

Attention is drawn to the fact that the copyright of this thesis rests with its author.

This copy of the thesis has been supplied on condition that anyone who consults it is understood to recognise that its copyright rests with its author and that no quotation from the thesis and no information derived from it may be published without the author's prior written consent.

D 12777/75
Kollath, K.J.A.
pp 163

THE LOW-FIELD STARK EFFECT OF HYDROGEN, $n=2$

by

Klaus-Johannes A. Kollath

Thesis submitted to the University of Stirling
for the degree of Doctor of Philosophy

Department of Physics
University of Stirling
Stirling

1974

ABSTRACT

The nonlinear low-field Stark effect in the level $n=2$ of hydrogen has been investigated.

The experiment employed the level crossing technique, measuring the position of the crossings between the Zeeman states:

$${}^2P_{3/2}, m_j = -3/2 \quad \text{and} \quad {}^2P_{1/2}, m_j = 1/2; \quad \text{and} \\ {}^2P_{3/2}, m_j = -3/2 \quad \text{and} \quad {}^2S_{1/2}, m_j = 1/2;$$

as the electric field was varied from 0 to 500 kV/m.

A beam of atomic hydrogen, produced by thermal dissociation, was subjected to parallel electric and magnetic fields. Lyman- α ($\text{Ly}\alpha$) resonance radiation was generated in an electrodeless microwave discharge lamp. The profile of the $\text{Ly}\alpha$ line emitted by the lamp has been investigated experimentally.

The level crossings were detected as changes of the $\text{Ly}\alpha$ resonance fluorescence intensity observed in a certain direction. The crossing positions were determined from the observed crossing signals of Lorentzian profile by a least squares computer programme.

The experimental results for the crossing positions as a function of the electric field have been compared with theoretical calculations. The theoretical values were obtained by numerical diagonalisation of the matrix of the eigenstates $|2l j m_F\rangle$ for perturbation by combined electric and magnetic fields. Radiative corrections were included.

Theoretical values and experimental results agree within the experimental uncertainties of 2%.

ACKNOWLEDGEMENT

I am indebted to Prof.H Kleinpoppen for suggesting this experiment and for his encouragement and continuous interest in its progress. I am very grateful to the other members of the Physics Department who participated in so many helpful discussions. In particular to Dr H-J Beyer with whom I enjoyed a fruitful cooperation in the spectroscopy laboratory, and to Dr A J Duncan for his careful reading of this thesis.

My thanks go also to Prof P S Farago and Prof R Kollath for many clarifying discussions and helpful suggestions.

. The technical problems in design and manufacture were always skillfully solved by Mr R R Harrison and the University's Shared Technical Service.

TABLE OF CONTENTS

List of figures

List of tables

CHAPTER I

I.1	Introduction	1
I.2	The Stark effect of hydrogen, review	2
I.2.1	The high-field Stark effect	2
I.2.2	The low-field Stark effect	8
I.3	Choice of experimental method	13
I.3.1	Magnetic field level crossings	13
I.3.2	Atomic beam method	17

CHAPTER II

II.1	Energy spectrum of the free H atom	19
II.1.1	Dirac and Breit equations	21
II.1.2	Bethe-Salpeter equation	26
II.1.3	Energy spectrum of the level $n=2$	31
II.2	The H atom in external fields	35
II.2.1	Stark effect	38
II.2.11	Electric field Hamiltonian	38
II.2.12	Electric field matrix elements	39
II.2.2	Zeeman effect	42
II.2.3	Matrix diagonalisation	50
II.3	Level crossing signals	56

CHAPTER III

III.1	Description of the apparatus	60
III.1.1	Vacuum system	60
III.1.2	The hydrogen beam	66
III.1.21	The hydrogen furnace	66

TABLE OF CONTENTS (cont.)

III.1.22	Beam geometry	70
III.1.23	Beam profile	70
III.1.24	Beam density	71
III.1.25	Dissociation of H ₂	74
III.1.3	The Ly α lamp	79
III.1.31	Lamp spectrum	80
III.1.32	Lamp intensity	81
III.1.33	Ly α line profile	85
III.1.4	Estimate of the resonance fluorescence rate	89
III.1.5	The magnetic field	91
III.1.51	Measurement of the field strength	91
III.1.52	Homogeneity	92
III.1.53	Stabilisation	92
III.1.6	The electric field	93
III.1.61	The condenser gap	94
III.1.62	Condenser voltage	95
III.1.63	Fringe field effects	95
III.1.7	Detection electronics	96
III.2	Experimental procedure	103
III.3	Data processing	105
III.3.1	Working line shape	105
III.3.2	Least squares fit	108
III.3.21	Computer programme	108
III.3.22	Goodness of fit	109
III.3.23	Average and rms error	111
III.3.3	Normalisation to Ly α intensity	112

TABLE OF CONTENTS (cont.)

CHAPTER IV

IV.1	Experimental results	115
IV.1.1	Crossing X1	115
IV.1.11	Crossing position	115
IV.1.12	Width and amplitude	121
IV.1.2	Crossing X2	124
IV.1.21	Crossing position	124
IV.1.22	Width and amplitude	127
IV.2	Error discussion	130
IV.2.1	Magnetic field	130
IV.2.2	Electric field	130
IV.2.21	Electric field parallel to the magnetic field	130
IV.2.22	Electric field perpendicular...	132
IV.2.3	Data analysis and signal distortions	136
IV.2.31	Variation of experimental factors	136
IV.2.311	Detection efficiency	136
IV.2.312	Hydrogen density	138
IV.2.313	Ly α emission	138
IV.2.32	Computer simulations	140
IV.3	Conclusion	144
IV.3.1	Comparison of experiment and theory	144
IV.3.2	Final remarks	150

List of references

LIST OF FIGURES

- I.1 Low-field Stark effect of hydrogen, $n=2$
- II.1 Graphs for the low order kernels
- II.2 Energy spectrum of the level $n=2$
- II.3 Zeeman effect in the FS of $n=2$
- II.4 Zeeman effect in the HFS of $2^2P_{3/2}$
- II.5 Zeeman effect in the HFS of $2^2P_{1/2}$ and $2^2S_{1/2}$
- II.6 FS levels in parallel electric and magnetic fields
- II.7 Level crossing X1 showing the HFS
- II.8 Anticrossing X1 for electric field $\vec{E} = (3.15, 0, 25) \text{ kV/m}$
- III.1 Photograph of the apparatus
- III.2 Diagram of the vacuum system
- III.3 The level crossing tank (LCT)
- III.4 Furnace assembly
- III.5 Circuit diagram for hydrogen furnace
- III.6 Mass 1 signal versus heating power
- III.7 Mass 1 signal versus hydrogen throughput
- III.8 Dependence of $\text{Ly}\alpha$ intensity on the magnetic field
- III.9 Schematic diagram of the $\text{Ly}\alpha$ line profile
- III.10 Experimental line profile
- III.11 Diagram of the detection system
- III.12 Experimental level crossing signal
- III.13 Distribution of $R = \text{SQ/NF}$
- IV.1 Position of crossing X1
- IV.2 FWHM of X1 versus electric field strength
- IV.3 Amplitude of X1 versus electric field strength

LIST OF FIGURES (cont.)

- IV.4 Position of crossing X2
- IV.5 FWHM of X2 versus electric field strength
- IV.6 Amplitude of X2 versus electric field strength
- IV.7 Comparison of experimental results and theory
 for X1
- IV.8 Comparison of experimental results and theory
 for X2

LIST OF TABLES

- II.1 Perturbation matrix for $n=2$
- III.1 Typical values of p_{FPT} , P , and R_{12}
- III.2 Condenser gap used in different experiments
- IV.1 List of measurements of crossing X1
- IV.2 Comparison of B_{appl} and B_{exp}
- IV.3 List of measurements of crossing X2
- IV.4 Uncertainty of the electric field strength
- IV.5 Effect of E_{\perp} on the position of crossing X1
- IV.6 Comparison of working line shapes
- IV.7 Comparison of experiment and theory for X1
- IV.8 Comparison of experiment and theory for X2

CHAPTER I

I.1 Introduction

The splitting of spectral lines under the influence of an external electric field was observed for the first time in 1913. In his experiments on the Balmer lines of hydrogen Stark found the well known linear Stark effect, implying a shift of the energy levels involved in the transitions proportional to the external electric field strength.

Such a linear Stark shift of the energy levels can only be obtained if the energy splitting between states with different orbital quantum numbers ℓ is negligible compared to the Stark shift. Therefore, the early theories which neglected the fine structure splitting gave a linear Stark effect and, for the high electric fields under consideration in Stark's experiments, theory and experiments agreed very well (Sec.I.2.1).

The Stark effect for low electric fields producing Stark shifts comparable to the fine structure was later treated theoretically (Sec.I.2.2). However, experimental measurements of the low-field Stark effect were not possible with the traditional spectroscopic methods which were limited by the Doppler broadening. Today much better resolution can be achieved with the level crossing method (Sec.I.3).

In this thesis an investigation of the nonlinear low-field Stark effect in the level $n=2$ of hydrogen employing the level crossing technique in an atomic beam experiment is reported.

I.2 The Stark effect in hydrogen, review.

Comparing the magnitude of the Stark shift with that of the fine structure splitting of the hydrogen ⁽¹⁾ levels under consideration, the range of electric fields can be subdivided in the following way: the high-field Stark effect, in which large electric fields produce Stark shifts large compared to the fine structure splitting; and the low-field Stark effect, in which small electric fields produce Stark shifts smaller or of the same order as the fine structure splitting.

I.2.1 The high-field Stark effect

The first investigation into the effect of an external electric field on atoms was conducted by Voigt as early as 1899 (V99). He estimated that a small effect, quadratic in the electric field strength, should be expected. In his experiments on the D lines of sodium, however, Voigt could not detect any splitting by the electric field. It, therefore, came as a surprise when in 1913 Stark (St13) and LoSurdo (L13) independently discovered a splitting of the Balmer lines of hydrogen in strong electric fields, which was subsequently found by Stark (St14) to be proportional to the applied electric field strength in the range from 10^6 to 10^7 V/m. Stark's measurements strongly supported the then new atomic theory by Bohr after Epstein (E16) and Schwarzschild (Schw16) had calculated the observed linear effect in terms of quantised orbits.

(1) For a more general review of the Stark effect see Bonch-Bruevich (BK67).

The same result was later obtained by Schrödinger (Sch26) applying the new wave mechanics. Schrödinger found that the equation for stationary states,

$$H^{(0)} \psi = W \psi, \quad (\text{I.1})$$

where

$$H^{(0)} = \frac{-\hbar^2}{2m} \nabla^2 - \frac{e^2 z}{(4\pi\epsilon_0) r}, \quad (\text{I.2})$$

was not only separable in spherical polar coordinates but also in parabolic coordinates ⁽¹⁾. The separability was maintained when the electric field term,

$$H_S = e \vec{E} \cdot \vec{r}, \quad (\text{I.3})$$

was added to the Hamiltonian and the field direction was chosen to coincide with the symmetry axis of the parabolic coordinate system.

(1) This property is a result of the O(4) symmetry of the hydrogen problem when spin and relativistic motion are neglected. The invariance of the Hamiltonian under rotation and parity operations for any potential V(r) (O(3) symmetry), which is equivalent to the conservation of angular momentum, leads to the degeneracy with respect to the directional quantum number m, and allows separation in the spherical coordinate system. The additional symmetry of the Coulomb potential, equivalent to the conservation of the Runge-Lenz vector, corresponds to the additional degeneracy with respect to the orbital quantum number ℓ. This higher symmetry allows the choice of the basis set for the Hilbert space of eigenfunctions belonging to the same energy, in two different physically significant ways. The two sets correspond to the set of ψ_{nlm} obtained by separating the Schrödinger equation in spherical coordinates, and to the set of Stark states $\psi_{nn_1n_2}$ obtained from separation in parabolic coordinates. See Hughes (H67) and references given in that paper.

The separated differential equations can be treated by means of a perturbation procedure (BS57) which to first order gives the result,

$$W = W^{(0)} + W^{(1)} = -Ry \frac{Z^2}{n^2} + \frac{3}{2} \frac{n}{Z} e a_0 E (n_1 - n_2), \quad (\text{I.4})$$

where the Rydberg energy ⁽¹⁾ is,

$$Ry = \frac{m e^4}{2 \hbar^2 (4\pi \epsilon_0)^2},$$

and n_1, n_2 are the parabolic quantum numbers with $0 \leq n_1, n_2 \leq (n-1)$.

The second term in Eq.I.4 describes a Stark shift of the energy levels linear in the electric field strength E .

For a given electric field strength the maximum separation between Stark terms belonging to the same level n is proportional to n^2 . Thus, when observing spectral lines the main contribution to the Stark splitting of the line is due to the upper level, and experiments would best be carried out in the Lyman series where only the respective upper level contributes. However, because of the inconvenient wavelengths of the Lyman lines, the experimental investigations of the Stark effect were confined to the Balmer series (Sj32, K33, SKS39, GS70), with the exception of the more qualitative work by Frerichs (F34). In these canal ray experiments the linear Stark effect has been observed for fields of order 10^7 V/m, and the slope found in the most recent work (GS70) agrees with theory within the experimental errors of less than 1%.

(1) The fundamental constants have the conventional definition as given by Taylor et al (TPL69). The equations in this section are quoted in SI units.

For higher electric fields the second order of the perturbation procedure must be included which takes into account the Stark mixing of states with different quantum numbers n and the result is,

$$W = W^{(0)} + W^{(1)} + W^{(2)}, \quad (I.5)$$

where

$$W^{(2)} = - \frac{(4\pi\epsilon_0)}{16} a_0^3 E^2 \left(\frac{n}{Z}\right)^4 (17n^2 - 3(n_1 - n_2)^2 - 9m^2 + 19).$$

The second order term $W^{(2)}$ describes a lowering, quadratic in the electric field strength, of all energy levels which is stronger for higher n and, therefore, results in a small red shift of all components of a Balmer line.

In third order the calculations by Ishida et al (I28) and, more recently by Tsai (T74) using operator techniques, give the result,

$$W^{(3)} = \frac{3}{32e} (4\pi\epsilon_0)^2 a_0^5 E^3 \left(\frac{n}{Z}\right)^7 (n_1 - n_2)(23n^2 - (n_1 - n_2)^2 + 11m^2 + 39). \quad (I.6)$$

The second and third order effects in the Balmer lines have been studied extensively by Rausch von Traubenberg (R31, and references given there). For fields up to 10^8 V/m the experiments are in good agreement with the Schrödinger theory and differ from the smaller shifts predicted by the Bohr theory.

For still higher electric fields Lanczos (L30) solved the separated equations numerically applying the WKB method. The results closely approximate those of the third order calculations except for very strong fields. For such fields the observation of the spectral lines is limited by field ionisation. The critical field values

for onset of ionisation found in the experiments agree well with Lanczos' calculations (L31).

Several attempts have been made to improve the resolution of the canal ray experiments and to extend the Stark effect measurements to smaller electric fields. Steubing and Junge (SJ49) measured the Stark splitting of H_{β} and H_{γ} for fields below 2000 kV/m and found satisfactory agreement with the Schrödinger theory for fields above 500 kV/m but reported surprising results for lower fields. Contrary to Schrödinger's theory which according to Lüders (L51) predicted a linear effect, the Stark splitting of the lines appeared to drop quadratically below 500 kV/m and to vanish completely at 200 kV/m. Below 400 kV/m Steubing and Junge could derive the "splitting" only by comparing the line widths observed with and without electric field. Obviously this method was not correct and their results are contradicted in the more recent experiments by Rother (R56) and by Gebauer and Selhofer (GS2 70).

Rother (R56) used a "Drehfeld" method. Canal rays were first subjected to a very high electric field which ionised the low energy Stark states of the $n=5$ level. The resulting asymmetric population of the Stark states was detected by measuring the ratio of the intensities of the weaker red shifted components to the violet shifted Stark components of H_{γ} . Then the canal ray traversed a region where an electric field perpendicular to the canal ray was suddenly reversed (Drehfeld), so that some of the atoms experienced a non-adiabatic transition which repopulated the ionised Stark states. From the known field distribution,

the velocity of the canal ray, and assuming the theoretical Stark splitting the integral probability for such transitions was calculated. From the measurement of the intensity ratio before and after the Drehfeld, the experimental transition probability was derived. To an accuracy of about 10% the experiment confirmed the linear Stark effect for fields as low as 150 kV/m and clearly disagreed with the results of Steubing and Junge.

The experiment by Gebauer and Selhofer (GS2 70) was a conventional canal ray experiment with improved resolution in which the splitting of H_γ was observed to be linear for fields down to 169 kV/m.

The theory of the Stark effect predicts not only the splitting of the energy levels and, therefore, the splitting of the spectral lines, but also the relative intensities and the polarisation of the line components.

The polarisation of the Stark components observed in the experiments (St13, GJ67) was found to agree well with the theoretical expectations.

The relative intensities for the Balmer lines calculated by Epstein (E16)* and Schrödinger (Sch26), were in general agreement with the earlier experiments but later more accurate measurements gave contradictory results depending strongly on the particular experimental conditions. Gebauer and Jäger (GJ67) solved this problem by inferring from the pressure dependence of the intensity distribution that radiationless collisions, selectively quenching the long lived Stark states, were responsible for the discrepancies.

* Corrected by Gordon and Minkowsky
Naturwiss. 17, 363 (1929)

I.2.2 The low-field Stark effect

The experiments reviewed in the preceding section were concerned with high electric fields and the results were described by theories neglecting the fine structure (FS). For the low-field Stark effect, where the Stark shifts are of the same order as the FS splittings, this approximation is not valid, and a theory is required which takes the FS into account.

Such a description of the Stark effect based on the Dirac equation was given independently by Schlapp (S28) and Rojanski (R29) who considered in particular the extreme cases of high electric fields and of very low fields. In the first case, for the high-field Stark effect, the familiar linear dependence was reproduced. In the second case, for Stark shifts small compared to the FS splittings, a linear effect was predicted for states with different orbital quantum numbers l , but identical j and n which are degenerate according to the Dirac theory. For the region between the two cases, where Stark shifts and FS splittings are comparable a nonlinear Stark effect was predicted. Later numerical calculations were carried out for this region by Lüders (L51) for the levels $n=2,3$ and 4.

In the calculation for the level $n=2$, which is of interest here, Lüders also included the Lamb shift (L50). The resulting Stark shifts in $n=2$ of hydrogen are reproduced in Fig.I.1 (Sec.II.2.1).

As may be seen from Fig.I.1, contrary to the prediction of the theory based on the Dirac equation, there is no linear Stark effect for fields below 300 kV/m if the

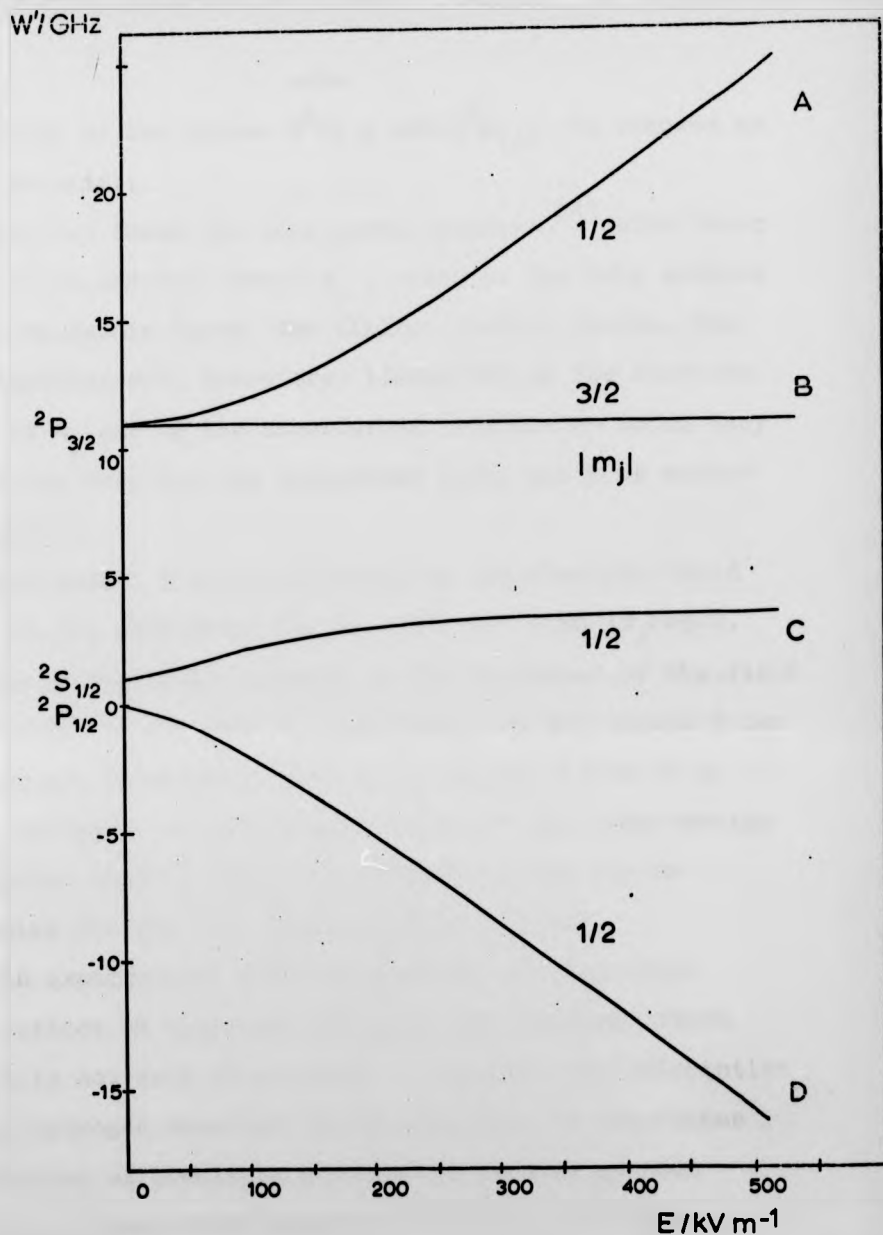


Fig.I.1 Low-field Stark effect in the level $n=2$ of hydrogen. The position of the unperturbed $2P_{1/2}$ level is chosen for zero energy. The three fine structure states are specified in spectroscopic notation. The branches are called A,B,C, and D and the absolute value of the corresponding directional quantum number m_j is indicated.

For electric fields below 300 kV/m there is no linear dependence of the Stark shifts on the electric field. In particular, branches C and D separated in zero electric field by the Lamb shift show a quadratic effect for fields below 50 kV/m .

degeneracy of the states $2^2P_{1/2}$ and $2^2S_{1/2}$ is removed by the Lamb shift.

Fig.I.1 shows the four Stark branches ⁽¹⁾ with their directional quantum number m_j , which is the only quantum number to remain "good" for finite electric fields. The four branches are, therefore, identified by the absolute value of m_j and by the unperturbed levels from which they originate. They will be designated A,B,C and D as marked in Fig.I.1.

The branch B is not affected by the electric field as it is the only state in the level $n=2$ with $|m_j|=3/2$. Because of the axial symmetry in the direction of the field only states of the same m_j are mixed, and the branch B can only couple to states belonging to higher values of n . Their influence is very small because of the large energy separation between states of different n and can be neglected for the low fields considered here.

An experimental investigation of this low-field Stark effect is desirable, because the low-field Stark effect is not only of interest to complete the description of the hydrogen atom but it has also been of importance in a number of precision experiments to test quantum electrodynamics and to measure fundamental constants. Such experiments are the determination of the Lamb shift (H III, R68), of the fine structure constant α (BBCM72), and of the Rydberg constant R_∞ (BS73, KRSS73).

In the original Lamb shift measurement (H III)

(1) The hyperfine structure (HFS) has been taken into account in the calculations which will be reported in Chapter II.

motional electric fields of the order of 1.05 kV/m were estimated for the hydrogen atoms in the beam. The Stark shifts of the Zeeman levels at the centre of the radio frequency resonances were calculated by second order perturbation theory, and the experimental results were corrected accordingly.

In the level crossing experiment by Baird et al (BBGM72) for the determination of the fine structure constant α , the Stark shifts introduced by thermal motion of the hydrogen atoms in the magnetic field of 3484 G led to a 0.75 ppm correction to the value of α .

To estimate the systematic errors in the determination of the Rydberg constant R_∞ the effect of small electric fields on the splitting and on the transition probabilities of H_α was investigated by Blackman and Series (BS73). The matrices for the electric field perturbation were diagonalised and the results were used to identify the H_α components least affected by electric fields and therefore best suited for the R_∞ determination.

Although the theory of the nonlinear Stark effect had been known since 1951 and the Stark effect corrections had been made in the experiments mentioned above, an experimental study of the low-field Stark effect was still outstanding prior to the present work.

Using traditional spectroscopic methods a measurement of the low-field Stark effect was not possible (G63) because of the very high resolution required. The only experiment to date with sufficient energy resolution has been a beam foil experiment by Andr s (A70) which

allowed the determination of the differential Stark effect between branches C and D for the limited range of electric fields between 10 kV/m and 40 kV/m. In this experiment the Lyman- α ($\text{Ly}\alpha$) intensity emitted by foil excited hydrogen atoms in an electric field was detected as a function of the distance from the foil, and the observed beat frequencies, corresponding to the separation of branches C and D were measured.

The beam foil method is not applicable to higher electric fields with correspondingly larger Stark shifts since the time resolution is limited to approximately 10^{-10} s by the speed of the atoms which is of the order of $5 \cdot 10^8$ cm/s. On the other hand the low-field Stark effect can be applied to investigate the mechanism of the foil excitation (A70, GAM74, E73).

In the work reported in this thesis the low-field Stark effect has been studied over a much wider range of electric field strengths. As outlined in the following section the level crossing technique has been chosen as the most promising experimental method. The results obtained from the level crossing experiment (Chapter IV) are in good agreement with the theoretical calculations reported in Chapter II.

I.3 Choice of experimental method

I.3.1 Magnetic field level crossings

A measurement of the low-field Stark effect requires a method capable of resolving energy differences of the order of the Lamb shift. For the Ly α line this requirement corresponds to a resolving power of $2.5 \cdot 10^6$ at 121.6 nm which cannot be obtained by conventional optical methods. More suitable are the modern level crossing, radio frequency, and quantum beat techniques which allow energy measurements in excited states with a precision comparable to the natural width of the levels involved. These methods utilise a "coupling" between close lying stationary energy levels of the atom. Under certain conditions the coupling produces resonance effects which are generally detected as a change in the spatial, spectral or temporal distribution of the fluorescence light.

Not all of the above methods can be applied to the Stark effect measurement in the level $n=2$ of hydrogen. The steady state experiments introducing the coupling between the $2^2S_{1/2}$ and one of the P states cannot be used here. Anticrossings, where the coupling is provided by a static electric field, cannot be detected because the metastable state has no measurable decay channel of its own (Se64, WE67). Similarly, no signals are expected when the coupling is introduced by electric radio frequency or microwave fields.

Experiments relying on the detection of the metastables (H III, R65) are not suitable either, since the lifetime of the $2^2S_{1/2}$ state reduces to about 50 ns for fields of

only 10 kV/m (H III, L50, H72).

Experiments using the modulation of fluorescence light in the presence of a static electric field to couple the S and P states, are possible with excitation by modulated light or electrons (Se64), or with beam foil excitation (A70). The first methods require excitation and detection at very high frequencies, difficult to obtain experimentally, and the time resolved level crossing effect is restricted to fields less than 5 kV/m. The beam foil method could only measure the differential Stark effect between the branches C and D over a narrow range of electric fields.

Among the methods based on a coupling between two levels of the short lived P states, the detection of the level crossings is the least complicated. Here the coupling of the states is part of the excitation process when the two levels are made degenerate by application of an external field. Such crossings cause a spatial redistribution of the resonance fluorescence radiation which can be detected as a change of the intensity observed in a particular direction. The external field may be a magnetic field (F61) or an electric field (KHL66).

In the level $n=2$ no crossings occur in the Stark pattern (Fig.I.1) but there are two crossings between P states when a magnetic field is applied (Fig.II.3, page 44).

The use of magnetic field level crossings for Stark effect measurements has been demonstrated by Budick et al (BMN65) for the case of ${}^7\text{Li}$, $n=3$ and has been applied to many other elements since. In such an experiment, first the position of the magnetic field level crossing is

determined, then an electric field is applied and the shift of the crossing position is measured as a function of the electric field strength.

The magnetic field crossings of the P states in the level $n=2$ of hydrogen are

$${}^2P_{3/2,-3/2} \times {}^2P_{1/2,1/2}, \text{ (de) at } 3484 \text{ G, and}$$

$${}^2P_{3/2,-3/2} \times {}^2P_{1/2,-1/2}, \text{ (df) at } 5223 \text{ G.}$$

The crossing states are specified in spectroscopic notation, the second subscript referring to the magnetic quantum number m_j , and the crossings are also identified using Lamb's notation by (de) and (df). The crossings have been detected experimentally by Wing and Fontana (WF67) and by Baird et al (B3GM72). Both crossings are very well suited for a Stark effect measurement because they involve the ${}^2P_{3/2,-3/2}$ state which is not affected by the electric field (branch B in Fig.I.1), and the states ${}^2P_{1/2,\pm 1/2}$ (branch D in Fig.I.1) which are of particular interest because their Stark effect depends on the presence of the Lamb shift.

For this work the (de) crossing has been preferred to the (df) crossings for two reasons. The (de) level crossing signal has the larger amplitude, and the geometry for optimum level crossing signals is more convenient experimentally. As there are no efficient polarisers available at the wavelength of 121.6 nm, unpolarised Ly α radiation has been used for excitation and detection. In the geometrical arrangement of the experiment the (de) level crossing resulted in a 13% decrease of the

unpolarised Ly α fluorescence light when no electric field was applied (BBGM72). The level crossing signal had a Lorentzian profile with a full width at half maximum (FWHM) of about 65 G.

When the electric field is present, states of different parity are coupled and the P content of branch D decreases with increasing electric field. Because of this S admixture to the originally pure P state at the crossing, the signal becomes weaker for higher electric field strength and could only be measured up to 250 kV/m.

On the other hand, the admixture of P character to the originally pure S states allows the detection of crossings which are not visible without electric field so that the crossing between the Zeeman levels

$${}^2P_{3/2,-3/2} \times {}^2S_{1/2,1/2}, (d\alpha)$$

(Fig.II.3, page 44) could be measured from 50 kV/m onwards.

To distinguish the two crossings used in this work the following nomenclature is introduced, avoiding the spectroscopic notation which is not valid in an electric field since ℓ ceases to be a good quantum number.

X1 refers to the crossing which for zero electric field occurs between the Zeeman levels ${}^2P_{3/2,-3/2}$ and ${}^2P_{1/2,1/2}$
and X2 refers to the crossing which for zero electric field occurs between the Zeeman levels ${}^2P_{3/2,-3/2}$ and ${}^2S_{1/2,1/2}$.

The two crossings are shown in Fig.II.3, page 44 for zero electric field and in Fig.II.5, page 51 for $E = 300$ kV/m.

The results obtained in the experiments reported here for the positions of the crossings X1 and X2 as a function of the electric field are equivalent to tracing branch D of Fig.I.1 from 0 to 250 kV/m and branch C from 50 to 500 kV/m.

I.3.2 Atomic beam method

The atomic beam method has been chosen to allow better control of the experimental conditions than would be possible in a "bottle" experiment, although a beam offers much smaller atomic density.

This decision was supported by the experience of Baird et al (MBB68, BBGM72) in their level crossing experiment for the determination of the fine structure constant α , where a discharge tube was used to produce the hydrogen atoms. The authors report that "we have applied an external electric field sufficiently large to shift the (crossing) signal by 1/2 of the line width. Since no shift was observed, we conclude that the average macroscopic electric field is zero due to the presence of free charges."

To avoid such screening effects an atomic beam of hydrogen with an expected density of $N = 10^9$ atoms/cm³ was used.

Because of the very small hydrogen density it was doubtful whether the Ly α resonance fluorescence light scattered from an atomic beam could be detected sufficiently well to make a level crossing experiment feasible. The experiment was, therefore, performed in two parts.

In the first part the Ly α resonance fluorescence was

observed and the spectral profile of the Ly α line investigated. In the second part, with a new apparatus, the level crossings X1 and X2 were detected and their positions measured as functions of the electric field.

CHAPTER II

In this chapter the theoretical background of the experiment is covered, beginning with a review of the energy spectrum of the free hydrogen atom in Sec.II.1. The perturbation of this spectrum by external electric and magnetic fields is treated in Sec.II.2, where the calculations of the crossing positions are described resulting in theoretical values which are later compared (Sec.IV.3.1) with the experimental results. In Sec.II.3 the theory of level crossing signals is reviewed.

II.1 Energy spectrum of the free hydrogen atom

The description of the energy levels of the simplest atomic system, the hydrogen atom has been a crucial test for all quantum theories ⁽¹⁾. It was a great success for Bohr's theory of quantised orbits when he derived Balmer's empirical formula,

$$\lambda_n = A \frac{n^2}{n^2-4}, \quad (\text{II.1})$$

where A is a constant, which related the wavelengths of the principal lines of the hydrogen spectrum.

The corresponding energy spectrum for the "radiationless orbits" was,

$$W(n) = - Ry Z^2/n^2, \quad (\text{II.2})$$

(1) A detailed account of the history has been given by Series (Se57) where the relevant references may be found.

where,

$$Ry = hc R_{\infty} = \frac{1}{2} mc^2 \alpha^2 = 13.6 \text{ eV} \text{ or } 2.2 \cdot 10^{-19} \text{ J},$$

is the Rydberg energy and,

$$\alpha = e^2 / (4\pi\epsilon_0 \hbar c),$$

is the fine structure constant.

Sommerfeld's generalisation to non-circular orbits and relativistic motion of the electron resulted in

$$W_{\text{rel}} = mc^2 \left(1 + \alpha^2 Z^2 / \left((n-k) + \sqrt{k^2 - \alpha^2 Z^2} \right)^2 \right)^{-1/2}, \quad (\text{II.3})$$

from which the famous formula for the binding energy spectrum was derived to be,

$$W(n,k) = - Ry \left(\frac{Z}{n} \right)^2 \left(1 + \frac{\alpha^2 Z^2}{n} \left(\frac{1}{k} - \frac{3}{4n} \right) + \dots \right), \quad (\text{II.4})$$

where $n = 1, 2, \dots$, $k = (\ell + 1) = 1, 2, \dots, n$, and ℓ is the quantum number of the orbital angular momentum.

The Bohr energy spectrum, Eq.II.2 was later derived again from Schrödinger's wave mechanics. Pauli added a fourth degree of freedom, the electron spin \vec{s} to the Schrödinger equation and the relativistic motion was included by Heisenberg and Jordan. The resulting energy spectrum was again given by Sommerfeld's fine structure formula, Eq.II.4. However, the levels were labeled differently. The quantum number k of Sommerfeld's theory was replaced by $(j+1/2)$, where

$$\vec{j} = \vec{s} + \vec{\ell}$$

is the total angular momentum of the electron. The new labeling led to new results for the line intensities removing the discrepancy between observations of the fine structure of H_{α} and the theoretical predictions

based on Sommerfeld's theory and the correspondence principle.

II.1.1 Dirac and Breit equations

When Dirac was searching for a relativistic covariant equation for the electron he proposed the Hamiltonian,

$$H^D = c \vec{\alpha} \cdot \vec{p} + \beta mc^2 \quad (\text{II.5})$$

aiming for an equation,

$$i\hbar \frac{\partial \psi}{\partial t} = H^D \psi, \quad (\text{II.6})$$

in which time and space derivatives were linear ⁽¹⁾.

To recover the relativistic energy relation,

$$W_{\text{mech}} = \sqrt{(\vec{p}c)^2 + m^2c^4}. \quad (\text{II.7})$$

the quantities $\vec{\alpha} = (\alpha_1, \alpha_2, \alpha_3)$ and β must obey the anticommutator relations,

$$\begin{aligned} \alpha_i \alpha_k + \alpha_k \alpha_i &= 2\delta_{ik}, \\ \alpha_i \beta + \beta \alpha_i &= 0, \end{aligned} \quad (\text{II.8})$$

and $\alpha_i^2 = 1, \beta^2 = 1.$

Quantities which fulfil such relations can be represented by 4 by 4 matrices. Using the Pauli spin matrices σ_i , the 4 by 4 matrices can be written in the compact form

$$\alpha_i = \begin{pmatrix} 0 & \sigma_i \\ \sigma_i & 0 \end{pmatrix}, \quad \beta = \begin{pmatrix} 1 & 0 \\ 0 & -1 \end{pmatrix} \quad (\text{II.9})$$

with,

$$\sigma_1 = \begin{pmatrix} 0 & 1 \\ 1 & 0 \end{pmatrix}, \quad \sigma_2 = \begin{pmatrix} 0 & -i \\ i & 0 \end{pmatrix}, \quad \sigma_3 = \begin{pmatrix} 1 & 0 \\ 0 & -1 \end{pmatrix}, \quad 1 = \begin{pmatrix} 1 & 0 \\ 0 & 1 \end{pmatrix}.$$

(1) This brief review of the Dirac theory follows Bjorken and Drell (BD64) and is given in the Gaussian unit system.

Since $\vec{\alpha}$ and β operate on the wave function ψ , the wave function also must have four components. It can be shown that two of the four components are smaller than the other two by a factor of order v/c and good approximate calculations are possible using only the large components.

The Dirac equation is now quoted in Lorentz covariant form to stress the similarity with the Bethe-Salpeter equation, Eq.II.24, defining,

$$\gamma^0 = \beta, \quad \gamma^i = \beta \alpha_i, \quad i=1,2,3; \quad \partial_\mu = \frac{\partial}{\partial x_\mu}, \quad \mu=1,2,3,4 \quad (\text{II.10})$$

and using "natural units", $c = 1, \hbar = 1$ to give,

$$(i \gamma^\mu \partial_\mu - m) \psi = 0, \quad \mu=1,2,3,4. \quad (\text{II.11})$$

For application to the hydrogen problem a Dirac equation is necessary which describes the electron motion in an electromagnetic field. Defining the electric field \vec{E} and the magnetic field \vec{B} by their potentials ϕ and \vec{A} according to

$$\vec{E} = -\nabla\phi - \frac{1}{c} \dot{\vec{A}}, \quad \vec{B} = \nabla \times \vec{A}, \quad (\text{II.12})$$

the Dirac equation can be expanded into the form

$$i\hbar \frac{\partial \psi}{\partial t} = (c\vec{\alpha} \cdot (\vec{p} - \frac{e}{c} \vec{A}) + \beta mc^2 + e\phi) \psi \quad (\text{II.13})$$

for a particle with charge e .

It turned out that this equation not only gave the relativistic corrections to the Schrödinger equation but also included the electron spin with the spin orbit interaction and the correct Zeeman effect. This result can be seen by reducing the Dirac equation in the non-relativistic limit to an equation for the two large components which leads to the Pauli equation.

Another approach to approximating the Dirac equation was developed by Foldy and Wouthuysen applying a transformation technique which systematically decoupled the large and small components of the Dirac wave function. In the presence of an electromagnetic field the components may be decoupled to any desired order at the expense of introducing further terms in the equation for the large components. After three transformations the Hamiltonian for the large components reads,

$$H = \left(mc^2 + \frac{(\vec{p} - e/c \cdot \vec{A})^2}{2m} - \frac{\vec{p}^4}{8m^3c^2} \right) + e\phi - \frac{e\hbar}{2mc} \vec{\sigma} \cdot \vec{B} \\ - \frac{e\hbar}{4m^2c^2} \vec{\sigma} \cdot (\vec{E} \times \vec{p}) - \frac{e\hbar^2}{8m^2c^2} \nabla \cdot \vec{E} . \quad (\text{II.14})$$

The terms in the first bracket are a series expansion of $\sqrt{(\vec{p} - e/c \cdot \vec{A})^2 c^2 + m^2 c^4}$. They include the orbital Zeeman effect and relativistic mass effect corrections. The next term in Eq.II.14 is the electrostatic energy, followed by the orientation energy of the spin magnetic dipole in the external magnetic field. The next term describes the interaction between electron spin and motional magnetic field. For a central potential $\phi = V(r)$, using $\vec{\ell} = \vec{r} \times \vec{p}$ the familiar form,

$$\frac{e}{2m^2c^2} \frac{1}{r} \frac{\partial V}{\partial r} (\vec{s} \cdot \vec{\ell}), \quad \text{where } \vec{s} = \frac{1}{2} \hbar \vec{\sigma}, \quad (\text{II.15})$$

for the spin-orbit energy emerges.

The last term of Eq.II.14 is called the Darwin term. It can be interpreted as a change of the effective potential experienced by the electron because of its fast jitter associated with the small components of the wave function.

In the extreme non-relativistic limit Eq.II.14 reduces to

$$H_{NR} = \frac{(\vec{p} - (e/c)\vec{A})^2}{2m} + e\phi - \mu_B \vec{S} \cdot \vec{B}, \quad (\text{II.16})$$

where

$$\mu_B = \frac{e\hbar}{2mc}$$

From Eq.II.16 the Pauli Hamiltonian H^P for a homogeneous magnetic field when terms quadratic in \vec{A} are neglected, may be derived to be,

$$H^P = \frac{p^2}{2m} - \frac{\mu_B}{\hbar} (\vec{L} + 2\vec{S}) \cdot \vec{B} + e\phi, \quad (\text{II.17})$$

explicitly showing the different g-factors for spin \vec{S} and orbital angular momentum \vec{L} of the electron.

When the Dirac equation is applied to the free hydrogen atom, in the form,

$$(c\vec{\alpha} \cdot \vec{p} + \beta mc^2 - \frac{Ze^2}{r})\psi = W\psi, \quad (\text{II.18})$$

the spectrum of energies given by Eq.II.3 and 4 with $k = j + 1/2$, is again obtained for the stationary states.

Refinements to the treatment of hydrogen were made
 a) to account for the nuclear motion by replacing the electron mass m by the reduced mass $\mu_H = m m_p / (m + m_p)$, and
 b) to account for the interaction of the electron with the nuclear dipole moment by inserting the vector potential \vec{A}_I of the magnetic dipole $\vec{\mu}_I$,

$$\vec{A}_I = \vec{\mu}_I \times \vec{r} / r^3. \quad (\text{II.19})$$

The resulting energy spectrum was accepted until Lamb and Retherford (LR47) confirmed earlier suggestions that the $2^2P_{1/2}$ and the $2^2S_{1/2}$ levels of hydrogen were not fully degenerate but the $2^2S_{1/2}$ was slightly shifted to higher energies. The discovery of this Lamb shift prompted

more detailed investigations into the problem of the interaction between charged particles and the electromagnetic field. The resulting new quantum electrodynamics (QED) has been very successful in explaining and calculating the Lamb shift.

Results of the QED may be approximated in the Dirac formalism by adding "radiative correction" terms to the Dirac Hamiltonian (BS57). However, the use of the Dirac equation which is a single particle equation, is not a very satisfactory way to approach the two body problem of the hydrogen atom.

The first step towards treating the two particles, electron and proton on an equal footing was carried out when the Hamiltonian which Breit had developed for the He problem (BS57) was used for the H atom. The particles e and p were described by their Dirac Hamiltonians and their interaction by the Coulomb potential and by the Breit operator \underline{B} so that,

$$H^B = H_e^D + H_p^D - \frac{Ze^2}{r} + \underline{B} . \quad (\text{II.20})$$

The Breit operator,

$$\underline{B} = - \frac{Ze^2}{2r} (\vec{\alpha}_e \vec{\alpha}_p + (\vec{\alpha}_e \cdot \vec{r})(\vec{\alpha}_p \cdot \vec{r})/r^2), \quad (\text{II.21})$$

can be derived from QED considering only the single transverse photon exchange between proton and electron.

\underline{B} can be regarded as the result of a QED perturbation calculation and must only be used in first order.

The total Hamiltonian H^B operating on a 16 component wave function can be reduced by a large component approach (H III). The reduced Breit equation accounts approximately for the hyperfine structure, for the nuclear motion, and

for radiative corrections in lowest order.

Although the Breit equation is sufficient to describe the Zeeman and Stark effect of the H atom (Sec.II.2) it is not very satisfactory because it does not furnish a covariant description of the H atom.

II.1.2 Bethe-Salpeter equation

A fully covariant description of the H atom can be derived from Lagrangian quantum field theory (QFT) which is briefly outlined in the following paragraphs.⁽¹⁾

Lagrangian QFT is a formalism to describe relativistic quantised systems of infinitely many degrees of freedom (fields) by treating the field amplitudes as operators $\varphi(x)$ subject to certain commutation relations. The field operators can be written as Fourier integrals in which positive and negative frequency parts can be separated. The coefficients of the positive (negative) frequency part are then identified as creation (destruction) operators for particles of specified energy-momentum k and other properties of the field in question. A Hilbert space is constructed from the vacuum state $|0\rangle$ by successive application of creation operators, leading to a complete base set. Each state of this base set $|n_\ell(k^\ell \alpha^\ell)\rangle$ is specified by the number n_ℓ of particles present which have particular energy-momentum k^ℓ and further properties denoted by α^ℓ . The set is referred to as particle number representation base.

(1) A detailed introduction into QFT is given by Roman (R69).

Similarly to the way in which the Fourier coefficients are interpreted, the positive (negative) frequency part of the field operators themselves can be interpreted as creating (destroying) a particle at a specified space-time location x .

The connection to the original field amplitudes $\phi_k(x)$ is made by the matrix element,

$$\langle 0 | \varphi(x) | 1(k, \alpha) \rangle \equiv \phi_k(x). \quad (\text{II.22})$$

It can be shown that $\phi_k(x)$ so defined is a solution of the non-quantised field equation, and is the probability amplitude for finding a particle with momentum k at location x .

Similarly the two particle amplitude,

$$\langle 0 | \varphi_1(x_1) \varphi_2(x_2) | 1_k 1_{k'} \rangle = \phi_{kk'}(x_1, x_2) \quad (\text{II.23})$$

is the probability amplitude for finding the free particles, particle 1 with momentum k at location x_1 and particle 2 with momentum k' at location x_2 , at the same time $x_1^0 = x_2^0$.

In the case of quantum electrodynamics (QED) the electromagnetic field and the Dirac fermion amplitude are treated by this formalism.

The Lagrangian formalism which provides a complete description for the free fields is then also applied to the case of interacting fields although no general mathematical justification can be given.

Such interacting fields are the solutions of field equations with interaction terms and cannot be directly related to observed particles (bare fields). For the interacting fields the particle numbers are no longer good quantum numbers. This fact may be interpreted in terms of fluctuations in the particle numbers due to

creation and destruction of virtual particles. The bare field may be visualised as a superposition of states with different particle numbers "dressing" the original particle with a "cloud" of virtual particles.

The bare fields are then used to construct the so called renormalised fields with the correct properties of observed particles. When the renormalisation constants relating the bare fields with the renormalised fields are calculated in perturbation theory, they are found to be infinite. For the H atom these divergencies can be ignored since the results for physical observables calculated from QED do not depend on the renormalisation constants and agree remarkably well with the observations.

From QFT the Bethe-Salpeter equation, which describes two fermions connected by an electromagnetic interaction, can be derived. For bound states between electron e and proton p the equation reads,

$$\begin{aligned} (i \gamma_e^\mu \partial_\mu^e - m_e)(i \gamma_p^\mu \partial_\mu^p - m_p) \chi_n(x_e, x_p) \\ = \int K(x_e, x_e', x_p, x_p') \chi_n(x_e', x_p') dx_e' dx_p' \end{aligned} \quad (\text{II.24})$$

where

$$\chi_n(x_e, x_p) = \langle 0 | T(\psi^e(x_e) \psi^p(x_p)) | k \rangle .$$

χ_n is, similarly to ϕ_{kk} , of Eq.II.23, the two particle amplitude for the fermion fields interacting with the electromagnetic field. χ_n may depend on different times for the two particles and in the matrix element the time ordered product is used, defined by,

$$\begin{aligned} T(\psi^e \psi^p) &= \psi^e \psi^p \text{ for } x_0^e > x_0^p \\ &= -\psi^p \psi^e \text{ for } x_0^e < x_0^p . \end{aligned}$$

The kernel K contains all the information on the interaction between the fermions. It cannot be given in closed form but for weak binding, as in the case of the hydrogen atom, the kernel can be approximated and low order perturbation calculations are expected to give reasonable results.

Using the Feynman graphs the first terms can be depicted by the graphs shown in Fig.II.1. They are (a) the one photon exchange graph, (b) the crossed, (c) the vacuum polarisation, (d) the self energy, and (e) the nuclear polarisation graphs. They are irreducible graphs standing for an infinite series of graphs with the same structure. For example the one photon kernel describes the exchange of one photon at a time, however the exchange can happen many times, as must be the case to describe a bound state.

Brodsky and Primack (BPr69) point out that the earlier theories for the H atom are recovered when successive approximations are made for the kernel K . The lowest order, the instantaneous ladder approximation, in the non-relativistic limit with $m/m_p \rightarrow 0$ yields the Schrödinger equation for an electron in a Coulomb potential. The exchange of one transverse photon accounts for the HFS and for the reduced mass corrections as described approximately by the Breit equation, Eq.II.20 and 21.

The ladder and crossed kernels together reproduce the Dirac equation with relativistic reduced mass correction. The vacuum polarisation and self energy kernels contribute to the Lamb shift and to radiative HFS corrections. Further contributions to the HFS may be expected from the fact that

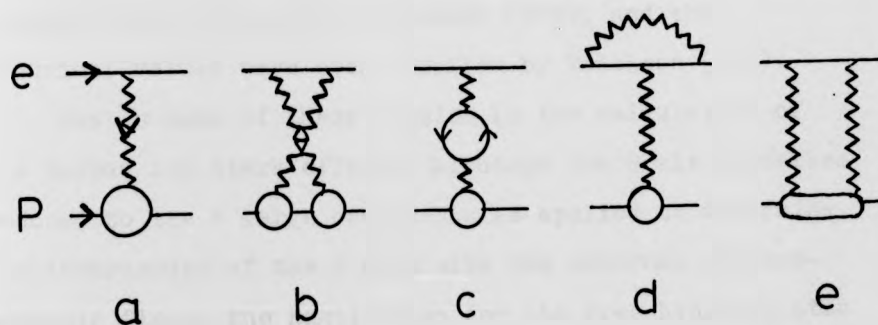


Fig.II.1 Graphs for the low order kernels of the Bethe-Salpeter equation (BPr69).
(a) one photon exchange, (b) the "crossed",
(c) vacuum polarisation, (d) self energy,
and (e) nuclear polarisation graphs.

the proton is not a point fermion but subject to strong interactions. This effect is indicated by the nuclear polarisation graph.

Calculations taking these and higher order kernels into account have been carried out by numerous authors. A review has been given by Brodsky (B70), and the numerical values have been compiled by Erickson (E71).

Use is made of these results in the calculation of the Zeeman and Stark effect. Although the Breit formalism reduced to the 4 large components is applied to determine the interaction of the H atom with the external electromagnetic field, the Hamiltonian for the free hydrogen atom is specified by the best known energy eigenvalues.

II.1.3 Energy spectrum of the level $n = 2$

The large component eigenfunctions of the reduced Breit equation contain the radial functions $R_{nl}(r)$, r being the relative coordinate, and the angular momentum eigenfunctions of the electron orbit $|\ell, m_\ell\rangle$, of the electron spin $|s, m_s\rangle$ and of the nuclear spin $|I, m_I\rangle$.

The three angular momenta $\vec{\ell}$, \vec{s} , and \vec{I} can be coupled with $\vec{j} = \vec{\ell} + \vec{s}$ as an intermediate state. The coupled functions are simultaneous eigenfunctions of the operators ℓ^2 , s^2 , j^2 , I^2 , F^2 and F_z with the quantisation axis in the z direction. They can be specified by the quantum numbers ℓ, j, F, m_F .

The functions $|n, \ell, j, F, m_F\rangle$ are very good approximations for the eigenfunctions of the total Breit Hamiltonian. Without external fields there are only very small off-diagonal elements of the Breit Hamiltonian for these functions.

The eigenfunctions in the coupled representation can be written in terms of the uncoupled functions

$$|nljFm_F\rangle = \sum_{m_l m_s m_j m_I} |nlm_l\rangle |sm_s\rangle |Im_I\rangle \times \\ \times (\ell m_l sm_s |jm_j) (jm_j Im_I |Fm_F) \quad (II.25)$$

The (|) are Clebsch-Gordon coefficients which include the restrictions $\Delta(\ell sj)$ ⁽¹⁾, $\Delta(jIF)$, and

$$m_l + m_s = m_j, \quad m_j + m_I = m_F.$$

In the case of hydrogen, $n = 2$, the orbital quantum number can be $\ell = 0, 1$ combining with $s = 1/2$ and $I = 1/2$ to form 16 states with $j = 3/2$ and $1/2$ and $F = 2, 1, 0$. The corresponding energy spectrum for the level $n = 2$ is shown in Fig.II.2. Without external fields the states differing only in m_F are degenerate.

The Lamb shift \mathcal{S} and the fine structure splitting ΔE are known. The experimental values, which are used in this work are,

$$\mathcal{S} = 1057.9 \quad (1) \text{ MHz (RS70),}$$

$$\Delta E = 10969.127(95) \text{ MHz (TPL69 and MBB68),}$$

in good agreement with the theoretical values,

$$\mathcal{S} = 1057.912 \quad (11) \text{ MHz,}$$

$$\Delta E = 10969.035 \quad (34) \text{ MHz (E71),}$$

derived using the natural constants as given by Taylor et al (TPL69).

(1) $\Delta(\ell sj)$ is the triangular condition for the values of j $j = \ell + s, \ell + s - 1, \dots, |\ell - s|$. It is symmetric in the three momenta.

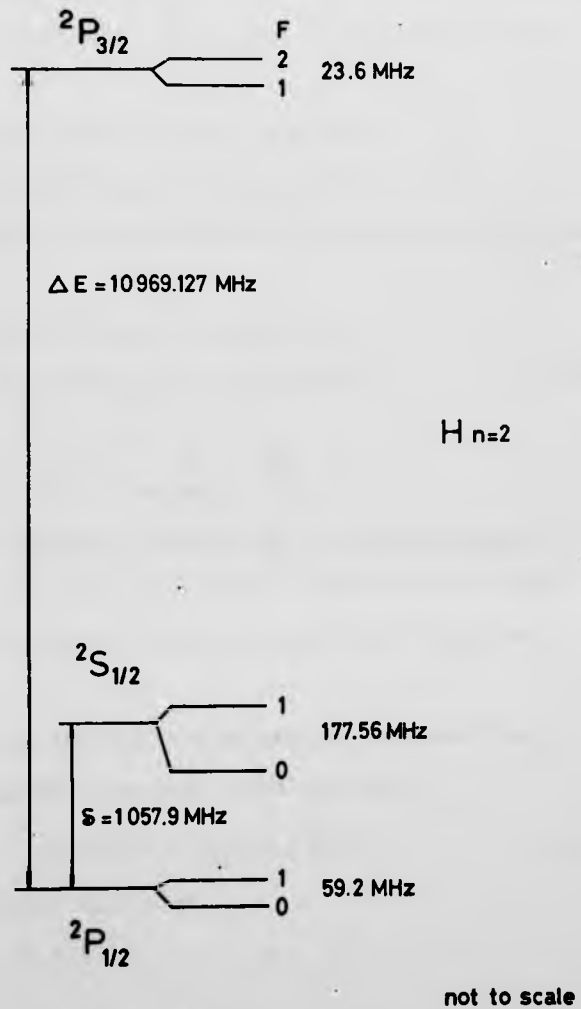


Fig.II.2 Energy spectrum of the level $n=2$, showing the three fine structure states and their hyperfine splittings. The diagram is not to scale but the numerical values of the level separations are given.

The positions of the HFS levels relative to the FS level are given by $\Delta \nu_{\text{HFS}}(lj) \langle \vec{I} \cdot \vec{j} \rangle$. The HFS splitting of the 2S state, which will be called K, is known from experiment to be,

$$K = 177.55686 (5) \text{ MHz (HRK56)}.$$

The splittings of the $^2P_{1/2}$ and $^2P_{3/2}$ states, which will be called H and L, have been calculated by Brodsky and Parsons (BP67) as,

$$\begin{aligned} H &= (E_F/3) (g_S/2 - (g_S-2)/4), \\ L &= (E_F/15)(g_S/2 - 5(g_S-2)/8), \end{aligned} \quad (\text{II.26})$$

where

$$E_F = \frac{2}{3} \alpha^2 c R_\infty \frac{\mu_p}{\mu_B} \left(\frac{\mu_H}{m} \right)^3,$$

μ_p is the proton magnetic moment, g_S is the g-factor of the electron spin, and μ_H is the reduced mass of the H system. Terms of order $(m/m_p) E_F$ and $(Z\alpha)^2 E_F$ are neglected.

In addition to the HFS contribution diagonal in j there are off diagonal elements from the term,

$$H_{\text{HFS}}' = (E_F/16)(2 - g_S/2) \langle \vec{I} \cdot \vec{\ell} \rangle \quad (\text{II.27})$$

for which the shorter notation,

$$H_{\text{HFS}}' = M \langle \vec{I} \cdot \vec{\ell} \rangle$$

will be used.

The corresponding matrix elements in the $|n(jFm_F)\rangle$ representation have been calculated by Brodsky and Parsons. They are reproduced in the matrix, Table II.1, page 49, together with the elements for external magnetic and electric fields.

II.2 The hydrogen atom in external fields

The interaction of a loosely bound two fermion system with an external electromagnetic field was investigated by Brodsky and Primack (BPr69). From Lagrangian QFT a Hamiltonian H_{BS}^{em} for the interaction with the external field was derived treating the binding of the two particles in the Bethe-Salpeter equation by the instantaneous ladder approximation (Coulomb potential). The resulting perturbation energy can be approximated very well by the Breit formalism when the Dirac Hamiltonians for the proton and electron include the external fields. The main contribution of higher order, self energy and vacuum polarisation kernels can be accounted for by the addition of anomalous moment terms. For a uniform magnetic field the contributions not included were estimated to be smaller than $\propto (\alpha Z)^2 \mu_B B$. To this order the Hamiltonian for the interaction of the hydrogen atom with the external field is,

$$H_R^{em} = |e| \vec{\alpha}_e \cdot \vec{A}_e - |e| A_e^0 - |e| \vec{\alpha}_p \cdot \vec{A}_p + |e| A_p^0 \\ + 2 \chi_e \frac{|e|}{2m} (\vec{s} \cdot \vec{B}) - 2 \chi_p \frac{|e|}{2m_p} (\vec{I} \cdot \vec{B}), \quad (II.28)$$

where $e_e = -|e|$ and $e_p = |e|$ have been used. The Hamiltonian consists of the Dirac parts of the electromagnetic interaction and the two terms for the anomalous magnetic moments described by χ_e and χ_p according to $g_{e,p} = 2(1 + \chi_{e,p})$, where g_e, g_p are the g-factors of the electron and proton, respectively.

A non-relativistic reduction H_{NR}^{em} , of Eq.II.28 was given by Brodsky and Primack (BPr68) in the form,

$$\begin{aligned}
 H_{NR}^{em} = \sum_{s=e,p} \left\{ -\frac{\vec{p}_s \cdot e_s \vec{A}_s}{m_s} + \frac{e_s^2 A_s^2}{2 m_s} + e_s A_s^0 - \mu_s \vec{G}_s \cdot \vec{B}_s - (2\mu_s - \frac{e_s}{2m_s}) * \right. \\
 \left. * \vec{G}_s \cdot \vec{E}_s x \frac{\vec{p}_s \cdot e_s \vec{A}_s}{2 m_s} \right\} + \frac{1}{4M} \left(\frac{\vec{G}_p}{m_p} - \frac{\vec{G}_e}{m} \right) \left[e_p \vec{E}_p x (\vec{p}_e - e_e \vec{A}_e) \right. \\
 \left. - e_e \vec{E}_e x (\vec{p}_p - e_p \vec{A}_p) \right] + O(1/m^3) \quad (II.29)
 \end{aligned}$$

Inside the sum H_{NR}^{em} contains terms familiar from the Foldy-Louthuysen (FW) reductions of the respective Dirac Hamiltonians, where $\hbar = 1$ and $c = 1$. The additional terms depending on the external electric field are corrections to the FW additivity. They are of kinematic origin, arising from the spin transformation of the wave function from the centre of mass (CM) system to the laboratory frame.

The Zeeman effect was calculated by Lamb (H III), Robiscoe (R 65), and Brodsky and Parsons (BP67) using a Hamiltonian of the type Eq.II.28. It was, therefore, in this work only necessary to estimate the size of the contributions in Eq.II.29 which depend on the electric field strength \vec{E} and to calculate the corresponding matrix elements.

To this end the centre of mass (CM) and the relative motion of the particles have been separated using,

$$\begin{aligned}
 \vec{p}_e &= \frac{m}{M} \vec{P} + \vec{p}, \quad \vec{p}_p = \frac{m_p}{M} \vec{P} - \vec{p}, \quad e_p = |e| = -e_e \\
 \vec{r}_e &= \frac{m_p}{M} \vec{r} + \vec{R}, \quad \vec{r}_p = -\frac{m_e}{M} \vec{r} + \vec{R}, \quad \vec{r} = \vec{r}_e - \vec{r}_p \\
 \mu_H &= \frac{m m_p}{m+m_p}, \quad M = m + m_p \quad (II.30)
 \end{aligned}$$

where \vec{R} and \vec{P} are the CM coordinate and momentum, and \vec{r} and \vec{p} are the relative coordinate and momentum.

For a uniform magnetic field \vec{B} with the vector potential $\vec{A} = (1/2) (\vec{B} \times \vec{r})$, and a uniform electric field \vec{E} with the potential $A^0 = -\vec{E} \cdot \vec{r}$, the result for the reduced Hamiltonian of Eq.II.29 is,

$$\begin{aligned}
 H_{NR}^{em} = & \frac{|e|\hbar}{2} \vec{B} \cdot (\vec{r} \times \frac{\vec{p}}{m}) + \frac{|e|\hbar}{2} \frac{1}{\mu_H} \vec{B} \cdot (\vec{r} \times \vec{p}) \\
 & - (\mu_e \vec{G}_e + \mu_p \vec{G}_p) \cdot \vec{B} - (\mu_e \vec{G}_e + \mu_p \vec{G}_p) \cdot \vec{E} \times \frac{\vec{p}}{m} \\
 & + |e|\hbar \vec{E} \cdot \vec{r} + \frac{|e|\hbar}{2m} \frac{m_p - m}{m_p} \vec{B} \cdot (\vec{r} \times \vec{p}) \\
 & - (2\mu_e + \frac{|e|\hbar}{2m}) \vec{G}_e \cdot \vec{E} \times \frac{\vec{p}}{2m}
 \end{aligned}
 \tag{II.31}$$

In the derivation, terms quadratic in the external fields have been neglected. Also a term similar to (7) for the proton spin has been neglected since it is small in comparison with term (7).

The terms (1) and (2) in Eq. II.31 were shown by Lamb (H III) to describe the motional electric field \vec{E}_{mot} ,

$$|e|\hbar \vec{r} \cdot \vec{E}_{mot} = |e|\hbar \vec{r} \cdot (\frac{\vec{p}}{m} \times \vec{B}) \tag{II.32}$$

Terms (3) and (4) are the orientation energy of the spin dipoles in the external magnetic field \vec{B} and in the motional magnetic field $\vec{E} \times \frac{\vec{p}}{m}$. Term (5) is the electrostatic energy in the external electric field, term (6) gives the orbital Zeeman effect with $g_l = (1 - m_e/m_p)$, and term (7), which has a similar form to a spin-orbit contribution, can be shown to be negligible (Sec. II.2.1).

The parts of Eq.II.31 depending on the electric field, including the motional field \vec{E}_{mot} , are considered in the subsequent section, the other terms, depending on the

magnetic field are quoted in Sec.II.2.2. in the form given by Brodsky and Parsons.

II.2.1 Stark effect

II.2.11 Electric field Hamiltonian

The terms of Eq.II.31 depending on the external electric field are,

$$H_S = |e| (\vec{E} \cdot \vec{r}) - (\mu_e \vec{G}_e + \mu_p \vec{G}_p) \cdot \vec{E} \times \frac{\vec{P}}{M} - (2\mu_e + \frac{|e|}{2m}) \vec{G}_e \cdot \vec{E} \times \frac{\vec{p}}{2m} \quad (\text{II.33})$$

The spin dependent contributions can be estimated by inserting for \vec{P}/M the velocity of the atoms in the beam of approximately $1 \cdot 10^6$ cm/s and for \vec{p}/m the velocity of $1.1 \cdot 10^8$ cm/s of the electron in the second Bohr orbit.

It follows that the magnetic field seen by the atom moving in the electric field is only $B' = 6 \cdot 10^{-5}$ G, corresponding for this experiment to a negligible energy contribution of 160 Hz. The third term in Eq.II.33 is only larger by about two orders of magnitude and can also be neglected.

The low-field Stark effect has, therefore been calculated from,

$$H = H_0 + H_S = H_0 + |e| (\vec{E} \cdot \vec{r}) \quad (\text{II.34})$$

where H_0 represents the full description of the free hydrogen atom, \vec{r} is the relative electron coordinate and \vec{E} is the external electric field.

This approach assumes that the dependence of H_0 on the electric field is small. This dependence was estimated by Brodsky ⁽¹⁾ to be of order

$\alpha(Z\alpha)^2 H_S = 6 \cdot 10^{-7} H_S$. It can be expected that the influence of the weak external field on the radiative corrections is very small, considering that these corrections for the strong internal Coulomb field of about $5 \cdot 10^{11}$ V/m are only of the order of the Lamb shift.⁽²⁾ It follows that in this experiment the dependence of the radiative corrections on the external electric field cannot be measured.

The external electric field E in this experiment is applied parallel to the magnetic field in the z -direction. The motional electric field, Eq.II.32 lies in the x - y plane. Further electric field components in the x - y plane can be generated by a misalignment of the magnetic and applied electric fields. For convenience the total field in the x - y plane E_{\perp} , was taken in the x -direction and the electric field vector in the form,

$$\vec{E} = (E_{\perp}, 0, E), \quad (\text{II.35})$$

was used in the calculations.

II.2.12 Electric field matrix elements

The matrix elements for the Stark Hamiltonian have been derived by application of the angular momentum formalism as presented by Edmonds (E60). Writing the vectors in spherical tensor notation,

(1) S. Brodsky, private communication.

(2) The influence of the real $Ly\alpha$ quanta in a level crossing experiment on the Lamb shift was shown to be negligible by Knight (K72).

$$\begin{aligned}
 E_{\pm 1} &= \mp \frac{1}{\sqrt{2}} (E_x \pm iE_y), \\
 E_0 &= E_z, \\
 \text{and } r_{\pm 1} &= \mp \frac{1}{\sqrt{2}} (x \pm iy), \\
 r_0 &= z
 \end{aligned}
 \tag{II.36}$$

the scalar product $D = \vec{E} \cdot \vec{r}$ is,

$$D = \sum_{\mu=-1}^1 (-1)^\mu E_{-\mu} r_\mu.
 \tag{II.37}$$

Using Racah's notation

$$C_q^{(k)} = \sqrt{\frac{4\pi}{2k+1}} Y_{kq}(\theta, \phi),
 \tag{II.38}$$

so that

$$r_m = r C_m^{(1)},$$

and the Stark Hamiltonian can be written

$$H_S = |e| D = |e| r \sum_{\mu=-1}^1 (-1)^\mu C_\mu^{(1)} E_{-\mu}.
 \tag{II.39}$$

Applying the Wigner-Eckart theorem to account for the m dependence and realising that the Stark Hamiltonian does not operate on the nuclear spin nor on the electron spin parts of the wavefunctions, the matrix elements for the level $n = 2$ are,

$$\begin{aligned}
 &\langle 2 \ell' j' F' m_F' | H_S | 2 \ell j F m_F \rangle \\
 &= |e| \sum_{\mu=-1}^1 (-1)^\mu E_{-\mu} (-1)^{j'+F'+j+F+1-m_F'} \\
 &\quad \sqrt{(2F'+1)(2F'+1)(2j'+1)(2j'+1)(2\ell'+1)(2\ell'+1)} \\
 &\quad \begin{pmatrix} \ell' & 1 & \ell \\ 0 & 0 & 0 \end{pmatrix} \begin{pmatrix} F' & 1 & F \\ -m_F' & \mu & m_F \end{pmatrix} \begin{Bmatrix} j' & F' & 1/2 \\ F & j & 1 \end{Bmatrix} \begin{Bmatrix} \ell' & j' & 1/2 \\ j & \ell & 1 \end{Bmatrix} \\
 &\quad \int R_{2\ell'}^* r R_{2\ell} dr
 \end{aligned}
 \tag{II.40}$$

The well known selection rules for electric dipole matrix elements are incorporated in the $3j$ and $6j$ symbols

$$\begin{aligned} \Delta F &= \pm 1, 0 & , & \quad \Delta j = \pm 1, 0 \\ \Delta \ell &= \pm 1 & , & \quad \Delta m_F = \mu = \pm 1, 0 \end{aligned} \quad (\text{II.41})$$

For parallel electric and magnetic fields m_F remains a good quantum number when the matrix is diagonalised, because the selection rules only allow Stark effect matrix elements between S and P states within the submatrix of given m_F . For an electric field perpendicular to the magnetic field matrix elements exist between S and P states with magnetic quantum numbers differing by $\Delta m_F = \pm 1$. In this case none of the original quantum numbers remain good.

The elements Eq.II.40 have been calculated using the tables by Rotenberg et al (RBMW59). The symmetry of the matrix provided a cross check for the elements $\langle i | H_S | j \rangle$ and $\langle j | H_S | i \rangle$ which were calculated independently. The matrix elements are shown in Table II.1. For Schrödinger eigenfunctions the radial integral is,

$$\int R_{2\ell}^* r R_{2\ell} dr = \sqrt{3} 3 a_0, \quad (\text{II.42})$$

and the Stark effect matrix elements of Table II.1 are to be multiplied by the factor $3\sqrt{3} a_0 e / h$, when using frequency units. The error made by evaluating the radial elements for Schrödinger functions instead of Dirac functions is expected to be of order 1 part in 10^4 (KSC73).

II.2.2 Zeeman effect

The most recent theoretical treatment of the Zeeman effect of hydrogen was given by Brodsky and Parsons (BP67). They considered the Hamiltonian,

$$H = H_0 + H_R^{em} \quad (II.43)$$

for a uniform magnetic field in the z-direction without electric field. The Hamiltonian H_0 again describes the free hydrogen atom including all known correction. The dependence of H_0 on the magnetic field is of order $\alpha^3 \mu_B B$ which is equivalent to a shift of 3 kHz for a magnetic field of 5 kG and may be neglected.

After radial integration for the n=2 states Brodsky and Parsons arrived at the effective Hamiltonian H_z , where

$$H_z = \mu_B B (A_S s_z + 1/2 A_\ell \ell_z + 1/2 \ell_z A_\ell + A_I I_z) \quad (II.44)$$

For the matrix elements the short notation

$$(F_z s_z I_z) + W = \mu_B B (F_z A_\ell + s_z (A_S - A_\ell) - I_z (A_\ell - A_I)) + W \quad (II.45)$$

with $W = 0$ for the unperturbed $^2P_{1/2}$ state, was introduced and the matrix elements are reproduced in this form in Table II.1, page 49.

The matrix for the Zeeman Hamiltonian, Eq.II.44 splits up into submatrices specified by the quantum numbers ℓ and m_F . The latter remains a good quantum number because of the rotational symmetry, the former because H_z does not operate on the radial part of the wave function.

The numerical values for the coefficients, estimated to be correct to 0.1 pp, for A_ℓ and A_S and 0.3 ppm for A_I , are

$$A_I = -g_I = -0.003\ 042\ 065,$$

$$A_S (\ell=0) = g_S (1 - \frac{\alpha^2}{12}) = 2.002\ 310\ 392,$$

$$A_S (\ell=1) = g_S (1 - \frac{\alpha^2}{10}) = 2.002\ 308\ 615, \text{ using}$$

$$g_S = 2.002\ 319\ 278, \text{ and}$$

$$A_\ell (\ell=1) = g_\ell (1 - \frac{\alpha^2}{8} + \frac{\alpha^2}{20} (\vec{s} \cdot \vec{\ell})), \text{ where } g_\ell = (1 - m/m_p).$$

The results for A_ℓ for different values of j are

$$A_{\ell 1} (j = 1/2 \leftrightarrow j = 1/2) = 0.999\ 446\ 056,$$

$$A_{\ell 2} (j = 1/2 \leftrightarrow j = 3/2) = 0.999\ 448\ 052$$

$$A_{\ell 3} (j = 3/2 \leftrightarrow j = 3/2) = 0.999\ 450\ 048 \quad (\text{II.46})$$

Numerical diagonalisation of the Zeeman matrix gives the results shown in Fig.II.3,4 and 5. In Fig.II.3 the Zeeman effect in the fine structure of $n=2$ is plotted. For zero magnetic field the three FS states are specified, and the values of the magnetic quantum number m_j are given on the right hand side. The crossings X1 and X2 used in this work are marked by the rectangles.

Fig.II.4 shows the Zeeman effect in the hyperfine structure of $2^2P_{3/2}$ and Fig.II.5 in the HFS of $2^2S_{1/2}$ and $2^2P_{1/2}$ covering 0...20 G and 0...200 G, respectively.

As long as the Zeeman splitting is smaller than the HFS, the eigenfunctions of the Zeeman states are approximated well by the low field representation $|n \ell j F m_F\rangle$. For higher magnetic fields where the HFS is smaller than the Zeeman splitting the eigenfunctions are better approximated by the high field representation $|n \ell j m_j m_I\rangle = |n \ell j m_j\rangle |I m_I\rangle$. This can be seen from the eigenfunctions calculated by the diagonalisation programme in the low field representation. In the example of the lowest level in Fig.II.4 the eigenfunction at 5 G is $\psi(5G) = |2\ 1\ 3/2\ 1 - 1\rangle$. At 3480 G the eigenfunction in terms of the low field

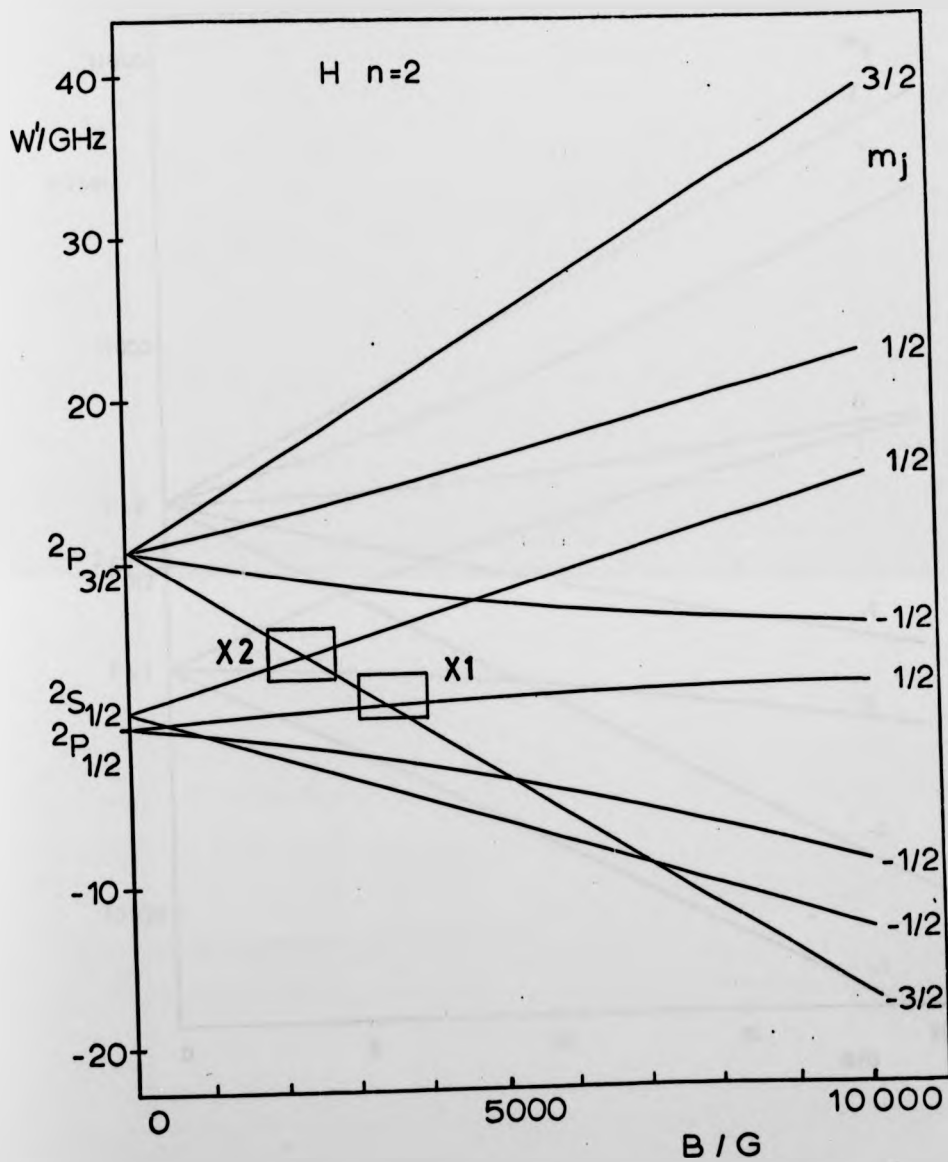


Fig.II.3 Zeeman effect in the fine structure of the level n=2 of hydrogen. The crossings X1 and X2 used in this work are indicated. On the left hand side the three fine structure states are specified in spectroscopic notation, on the right hand side the magnetic quantum numbers of the Zeeman levels, m_j are given.

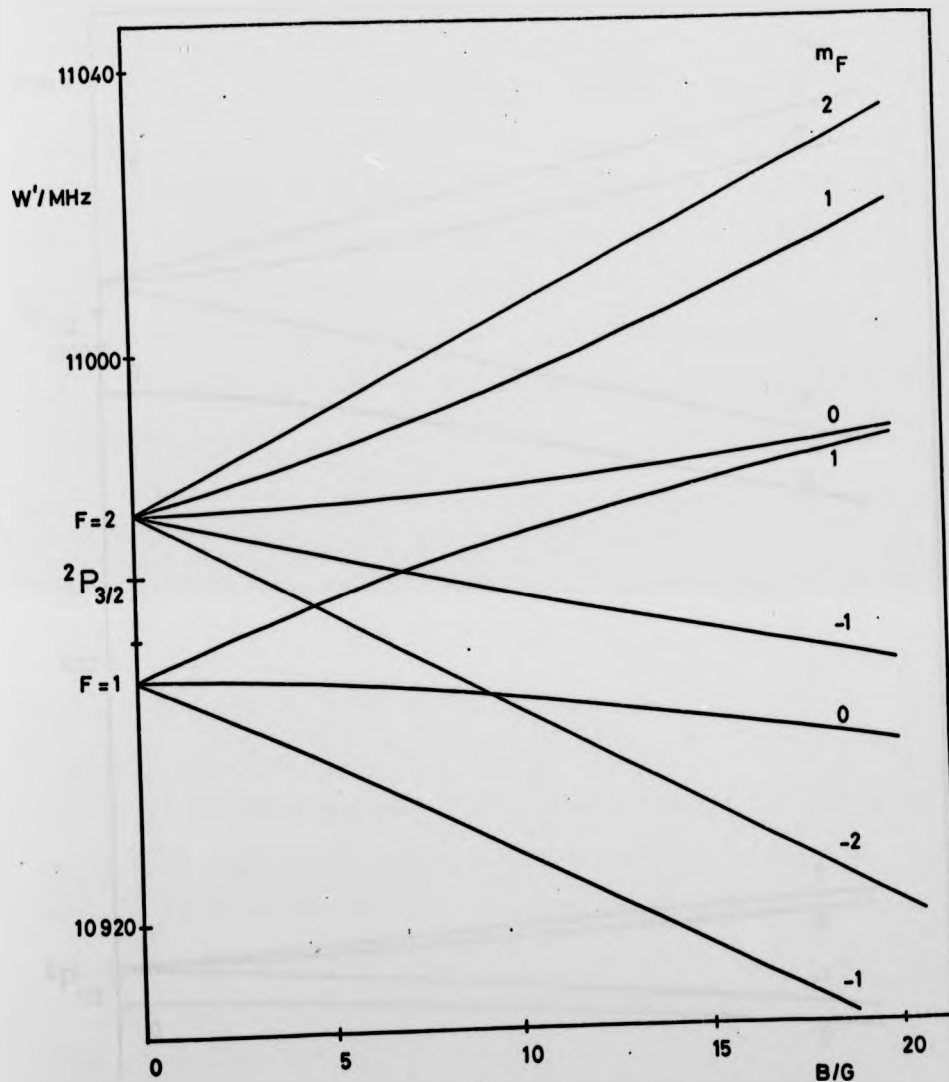


Fig.II.4 Zeeman effect in the hyperfine structure of $2^2P_{3/2}$. The quantum number F of the total angular momentum of the unperturbed states and the magnetic quantum number m_F of the Zeeman levels are shown.

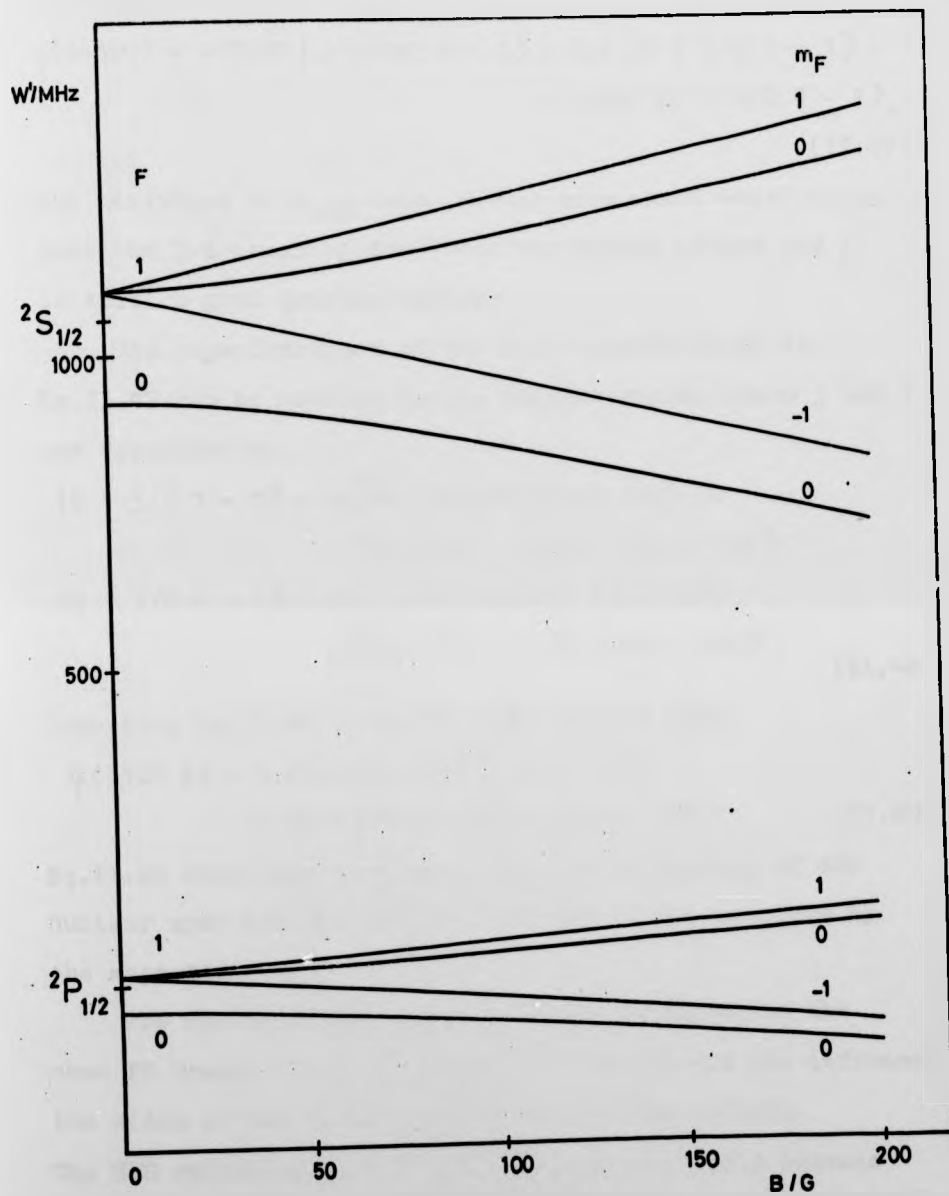


Fig.II.5 Zeeman effect in the hyperfine structure of $2^2P_{1/2}$ and $2^2S_{1/2}$. The quantum number F of the total angular momentum of the unperturbed states and the magnetic quantum number m_F of the Zeeman levels are shown.

representation is

$$\psi(3480G) = -0.87 |2\ 1\ 3/2\ 1\ -1\rangle + 0.5 |2\ 1\ 3/2\ 2\ -1\rangle + 0.002 |2\ 1\ 1/2\ 1\ -1\rangle. \quad (\text{II.47})$$

The admixture of $P_{1/2}$ character is very small which means that the L-S coupling dominates the Zeeman effect and j is still a good quantum number.

The eigenfunctions of the main contributions in Eq.II.47 can be written in the representation where j and I are decoupled as,

$$\begin{aligned} |2\ 1\ 3/2\ 1\ -1\rangle &= -\sqrt{3/4} |3/2-3/2\rangle |1/2\ 1/2\rangle + \\ &\quad + 1/2 |3/2\ -1/2\rangle |1/2\ -1/2\rangle \\ |2\ 1\ 3/2\ 2\ -1\rangle &= 1/2 |3/2\ -3/2\rangle |1/2\ 1/2\rangle + \\ &\quad + \sqrt{3/4} |3/2\ -1/2\rangle |1/2\ -1/2\rangle. \end{aligned} \quad (\text{II.48})$$

Inserting Eq.II.48 in Eq.II.47 it follows that,

$$\psi(3480\text{ G}) = 1.00 |3/2\ -3/2\rangle |1/2\ 1/2\rangle + 0.01 |3/2\ -1/2\rangle |1/2\ -1/2\rangle. \quad (\text{II.49})$$

Eq.II.49 describes an almost complete decoupling of the nuclear spin and the angular momentum of the electron by the magnetic field.

The HFS splitting between levels belonging to the same FS Zeeman level is of interest because it can influence the width of the level crossing signal (Sec.II.3). The HFS splitting varies with the magnetic field because of the orientation energy of the nuclear magnetic moment $\bar{\mu}_I$.

In the Zeeman levels with $m_j > 0$ the two HFS levels cross over when the perturbation energy,

$$W_{IB} = -g_I \mu_B B m_I, \quad (\text{II.50})$$

exceeds the HFS splitting,

$$W_{Ij} = \Delta \nu_{\text{HFS}}^{(lj)} m_I m_j. \quad (\text{II.51})$$

The magnetic field strength for such cross overs can be determined by estimating from the known HFS splittings the internal magnetic field generated by the electron.

These fields are approximately

4200 G from an electron in the $2^2P_{3/2}$ state,

7000 G from an electron in the $2^2P_{1/2}$ state, and

21000 G from an electron in the $2^2S_{1/2}$ state. The

numerical results for the cross overs obtained from the matrix diagonalisation agree with these estimates.

For the FS Zeeman levels with $m_j < 0$ the calculations show a small widening of the HFS splittings.

It will be shown that the effect of the variable HFS splittings on the level crossing signals is negligible (Sec.II.3).

Table II.1 Energy matrix of the level $n=2$ of hydrogen including the perturbations by magnetic and electric fields.

The fine structure splitting between ${}^2P_{3/2}$ and ${}^2P_{1/2}$ states is denoted ΔE . The Lamb shift between ${}^2P_{1/2}$ and ${}^2S_{1/2}$ states is denoted S . The energies are given relative to the ${}^2P_{1/2}$ state.

The HFS splittings of the ${}^2P_{1/2}$, ${}^2S_{1/2}$ and ${}^2P_{3/2}$ states are called H, K, and L. The off diagonal HFS term is called M.

For the magnetic field matrix elements the notation of Brodsky and Parsons (BP67) has been used,

$$(F_z s_z I_z) = \mu_B B (F_z A_L + s_z (A_S - A_L) - I_z (A_L - A_I)).$$

The Stark effect matrix elements are quoted with the spherical components of the electric field

$$E_0 = E_z,$$

$$E_{\pm 1} = \mp \frac{1}{\sqrt{2}} (E_x \pm i E_y).$$

The matrix elements of the Stark effect have to be multiplied by the factor $3\sqrt{3} a_0 |e|/\hbar$, if Schrödinger eigenfunctions are used to evaluate the radial matrix elements and the matrix elements are used in frequency units.

II.2.3 Matrix diagonalisation

The Stark and Zeeman spectra shown in Fig.I.1 and Fig.II.3,4, and 5 have been obtained by numerical diagonalisation of the respective perturbation matrices by a computer programme. All numerical work has been done using the fundamental constants quoted by Taylor et al (TPL69).

A FORTRAN subroutine, KTHE4 calculated the numerical values of the Stark and Zeeman effect matrix elements according to equations Eq.II.40 and Eq.II.45 and the resulting 16 by 16 matrix was diagonalised numerically by the subroutines MCO4A, EAO4B, EAO5A, and EAO1B⁽¹⁾.

The subroutine MCO4A reduced the real symmetric matrix by Householders method to a triple diagonal matrix with the same eigenvalues (W62). The eigenvalues of the triple diagonal matrix were found by a bisection method based on a Sturm sequence in subroutine EAO4B (BMW67) and printed out in ascending order. The corresponding eigenvectors were found by subroutine EAO5A (W2 62) by inverse iteration and were then transformed back to the eigenvectors of the original matrix. EAO1B is the organising routine.

An example of the energy levels for parallel electric and magnetic fields is shown in Fig.II.6. In accordance with the Stark spectrum in Fig.I.1 the branches A and C are almost equidistant from branch B, and branch D is found

(1) The original sequence by E. York has been improved and tested by J. Woolsey.

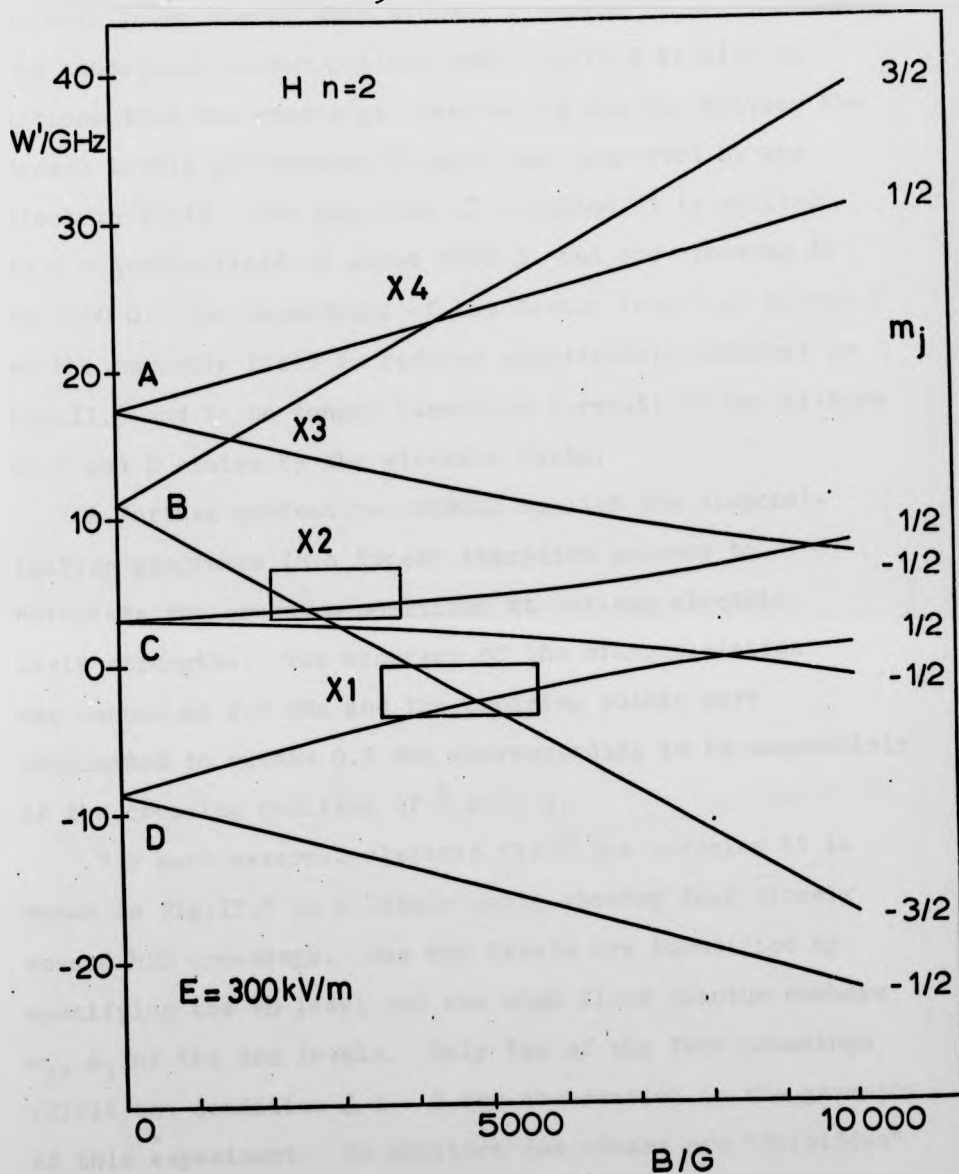


Fig.II.6 Fine structure levels for parallel electric and magnetic fields. The energy levels are shown for an electric field strength of 300 kV/m as a function of the magnetic field. The crossings X1 and X2 used in the experiment are indicated. For $B = 0 \text{ G}$ the branches are labelled as in Fig.I.1. The directional quantum number m_j is given on the right hand side. The new crossings are called X3 and X4.

at much lower energy than without electric field. Comparing the subsequent Zeeman pattern with Fig.II.3 it will be noticed that new crossings, denoted X3 and X4, between the Zeeman levels of branches B and A are generated by the electric field. The position of crossing X1 is shifted to a magnetic field of about 5000 G, and the crossing X2 to 2500 G. The dependence of the Zeeman levels of branch C on the magnetic field is reduced considerably compared to Fig.II.3 and is no longer linear as a result of the mixture of S and P states by the electric field.

A further subroutine, KCROSS applied the diagonalisation programme in a linear iteration process to calculate the crossing positions at various electric field strengths. The accuracy of the diagonalisation was chosen as 0.1 MHz and the crossing points were determined to within 0.2 MHz corresponding to an uncertainty of the crossing position of ± 0.05 G.

For zero external electric field the crossing X1 is shown in Fig.II.7 on a larger scale showing four closely spaced HFS crossings. The HFS levels are identified by specifying the FS level and the high field quantum numbers m_J , m_I of the HFS levels. Only two of the four crossings fulfil the condition $\Delta m = 2$ for observation in the geometry of this experiment. In addition the others are "forbidden" by the $\Delta m_I = 0$ selection rule for optical excitation from the ground state.

The calculated values for the positions of the $\Delta m = 2$ HFS crossings are 3476.24 G and 3491.99 G. They agree well with the results of Himmel and Fontana (HF67) of 3476.06 G and 3491.93 G, considering that different values for the fundamental constants and for the FS splitting ΔE have

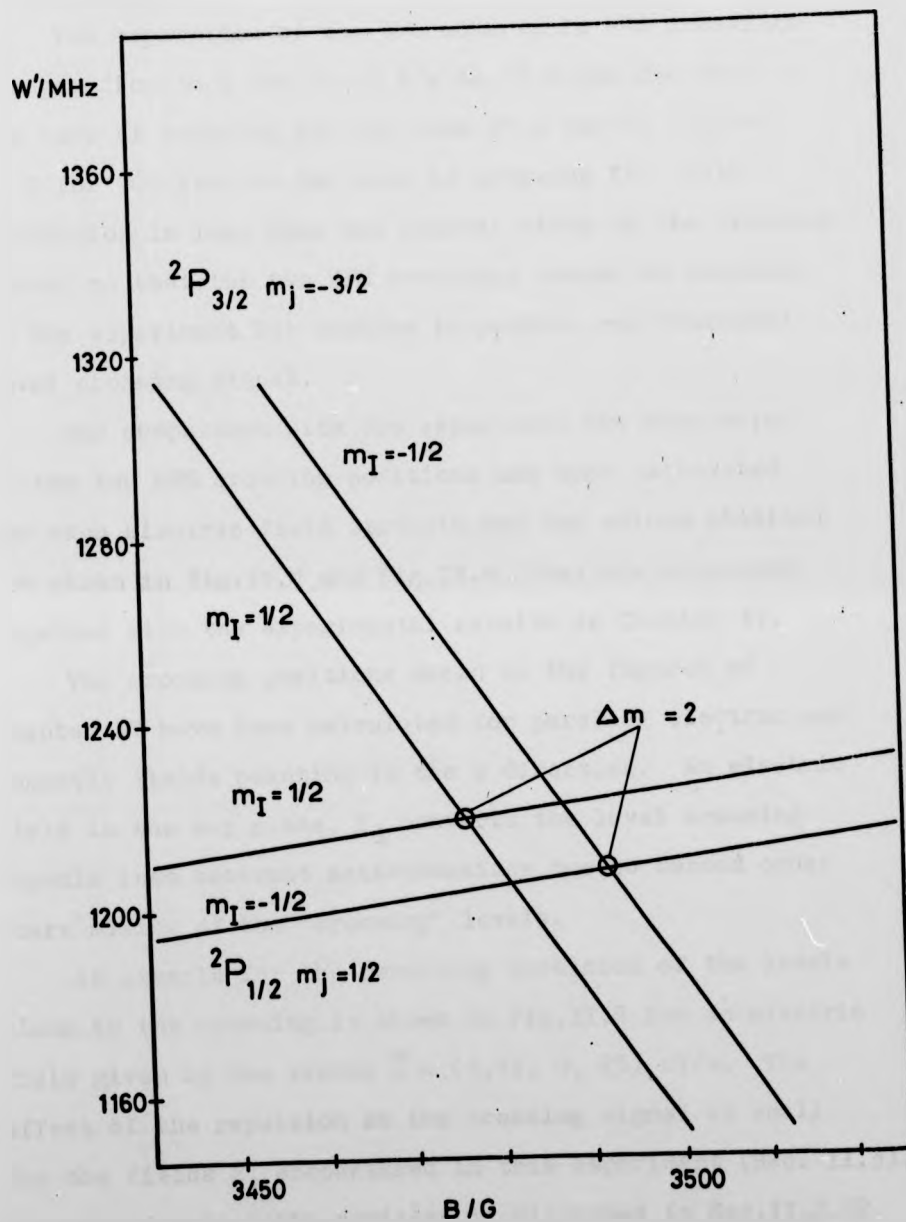


Fig.II.7 Level crossing X1 for zero electric field, showing the hyperfine splittings. The levels are specified by the quantum numbers m_j and m_I appropriate for the high field representation. The two observable $\Delta m = 2$ crossings are encircled.

been used in the two calculations.

The separation of the two observable HFS crossings changes from 18 G for $E = 0$ V/m to 15 G for 250 kV/m in the case of crossing X1, and from 25 G for 50 kV/m to 17 G for 500 kV/m in the case of crossing X2. This separation is less than the natural width of the crossing states so that the two HFS crossings cannot be resolved in the experiment but combine to produce one broadened level crossing signal.

For comparison with the experiment the mean value of the two HFS crossing positions has been calculated for each electric field strength and the values obtained are shown in Fig.IV.1 and Fig.IV.4. They are discussed together with the experimental results in Chapter IV.

The crossing positions shown in the figures of Chapter IV have been calculated for parallel electric and magnetic fields pointing in the z direction. An electric field in the x-y plane, E_{\perp} converts the level crossing signals into coherent anti-crossings due to second order Stark mixing of the "crossing" levels.

An example for the resulting repulsion of the levels close to the crossing is shown in Fig.II.8 for an electric field given by the vector $\vec{E} = (3, 15, 0, 25)$ kV/m. The effect of the repulsion on the crossing signal is small for the fields E_{\perp} encountered in this experiment (Sec. II.3), and the effect on the position is discussed in Sec.IV.2.22.

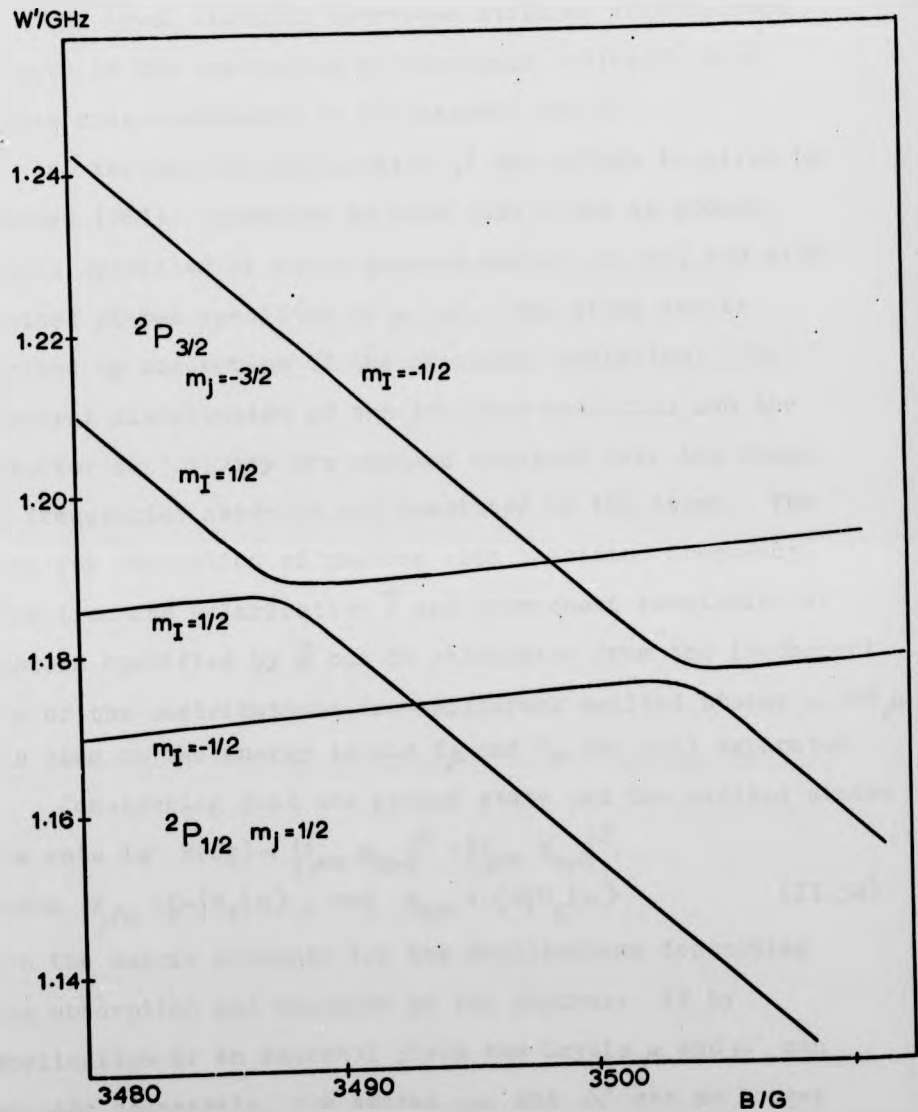


Fig.II.8 Anticrossing X1 for an electric field given by the vector $\vec{E} = (3.15, 0, 25.)$ kV/m. The two HFS crossings shown in Fig.II.7 are converted into anticrossings in the presence of an electric field perpendicular to the magnetic field by second order Stark coupling of the "crossing" states.

II.3 Level crossing signals

The level crossing technique utilises interference effects in the scattering of resonance radiation from states made degenerate by an external field.

An instructive explanation of the effect is given by Franken (F61). Consider an atom with a set of ground states specified by their quantum numbers m, m' , and with excited states specified by μ, μ' . The atoms can be excited by absorption of the resonance radiation. The spectral distribution of the incident radiation and the detector sensitivity are assumed constant over the range of frequencies absorbed and reemitted by the atoms. The rate for absorption of photons with specified frequency, direction and polarisation \vec{f} and subsequent reemission of photons specified by \vec{g} can be calculated from the incoherent sum of the contributions from different excited states μ and μ' as long as the energy levels E_μ and $E_{\mu'}$ are well separated.

Considering just one ground state and two excited states the rate is $R(fg) \sim |f_{\mu m} \mathcal{E}_{m\mu}|^2 + |f_{\mu' m} \mathcal{E}_{m\mu'}|^2$, where $f_{\mu m} = \langle \mu | H_f | m \rangle$, and $\mathcal{E}_{m\mu} = \langle m | H_g | \mu \rangle$ (II.52)

are the matrix elements for the Hamiltonians describing the absorption and emission of the photons. If by application of an external field the levels μ and μ' can be made degenerate, the states μ and μ' can no longer be distinguished in the resonance fluorescence process and the two probability amplitudes must be added, resulting in,

$$R(fg) \sim |f_{\mu m} \mathcal{E}_{m\mu} + f_{\mu' m} \mathcal{E}_{m\mu'}|^2. \quad (II.53)$$

If none of the matrix elements is zero the two expressions Eq.II.52 and Eq.II.53 differ by the "interference terms".

The resonance fluorescence of an atom with several close lying levels had been discussed earlier by Breit (B33) and the resulting Breit formula was derived again by Franken (F61):

$$R(fg) = \sum_{\mu\mu'mm'} \frac{f_{\mu m} f_{m\mu'} g_{\mu'm'} g_{m'\mu}}{1 + 2i \frac{W_{\mu} - W_{\mu'}}{\hbar (\Gamma_{\mu'} + \Gamma_{\mu})}}, \quad (\text{II.54})$$

where W_{μ} is the energy and Γ_{μ} is the decay constant of level μ , and m, m' denote different magnetic substates of the ground state assumed to be populated equally.⁽¹⁾

The Breit formula, Eq.II.54 contains the incoherent sum of the well separated levels, where the terms with $\mu + \mu'$ can be neglected because

$$\frac{2 (W_{\mu} - W_{\mu'})}{\hbar (\Gamma_{\mu} + \Gamma_{\mu'})} \gg 1,$$

and the coherent superposition of close levels, where

$$\frac{2 (W_{\mu} - W_{\mu'})}{\hbar (\Gamma_{\mu} + \Gamma_{\mu'})} \ll 1.$$

The angular correlation of incident and scattered electric dipole radiation was considered in detail by Rose and Carovillano (RC61). For the single electron system, neglecting HFS, and unpolarised light they found the rate R_S from the interference terms to be,

$$R_S = A P_2^{\mu-\mu'}(\cos \vartheta_1) P_2^{\mu-\mu'}(\cos \vartheta_2) \frac{\hbar \Gamma_{b'b} \cos \beta - W_{b'b} \sin \beta}{\hbar^2 \Gamma_{b'b}^2 + W_{b'b}^2}, \quad (\text{II.55})$$

where the crossing states are b and b' with magnetic quantum numbers μ and μ' , and A is a constant, $P_2^{\mu-\mu'}$ is the Legendre function, and $\beta = (\mu - \mu')(\varphi_1 - \varphi_2)$, $\Gamma_{b'b} = (\Gamma_b + \Gamma_{b'}) / 2$,

$$W_{b'b} = W_{b'} - W_b. \quad \text{The angles } \vartheta_1 \text{ and } \vartheta_2$$

are the polar angles of incident and scattered light relative to the symmetry and quantisation axis. $(\varphi_1 - \varphi_2)$ is the

(1) This condition is fulfilled very well for the ground state of H and the small external fields.

difference in azimuthal angle.

Eq.II.55 shows that $\Delta\mu = 2$ crossings can best be detected by choosing $(\varphi_1 - \varphi_2) = 90^\circ$ and $\vartheta_1 = \vartheta_2 = 90^\circ$, when the resulting level crossing signal has a Lorentzian profile with maximum amplitude.

For these geometrical conditions Himmel and Fontana (HF67) investigated the signal of level crossing X1 for zero electric field including the HFS. Treating the interaction of the two body system, electron and proton, with the incident photon in the non-relativistic approximation, they derived the same expressions for the Breit formula as Rose and Carovillano, adding only the selection rule $\Delta m_I = 0$. Himmel and Fontana showed that the FWHM of the total crossing signal from the two HFS crossings has a width of $b = 67.2$ G which is only 2 G wider than that calculated without HFS from,

$$b' = 2 \frac{\partial B}{\partial W_{b,b}} \hbar \Gamma_{b,b} = 65 \text{ G} . \quad (\text{II.56})$$

It follows that the small changes of the separation between the HFS crossings mentioned in Sec.II.2.3 have little influence on the width of the observed crossing signals.

The characteristics of the crossing signal were recalculated by Baird et al (BBGM72) who found that the two HFS crossing signals have the same amplitude within 0.05%, both containing a dispersion contribution of only 0.1%. The ratio of the coherent terms of the fluorescence rate at the crossing position to the incoherent terms was 0.138 with HFS, compared to 0.146 without HFS. Baird et al proceeded to derive an accurate formula for the line shape for the data analysis in their high precision experiment.

In this work the unresolved HFS crossings were approximated by only one Lorentzian line shape. This line shape is a good approximation of the observed crossing signals for zero electric field where the two HFS crossings have equal amplitude (Sec.IV.2.32). It is expected to be a good approximation for finite electric fields as well, since the separation of the two HFS crossings changes little and the S admixture to the originally pure P states affects the two HFS levels of the FS Zeeman level in much the same way.

As shown in Sec.II.2.3 an electric field perpendicular to the magnetic field causes the levels to repel one another due to Stark mixing via one or more intermediate states. Such anticrossings were described by Wieder and Eck (WE67). The coherent anticrossing signals are smaller than the pure level crossing signals by approximately

$$\Gamma_{b'b}^2 / (\Gamma_{b'b}^2 + W_{b'b}^2 \min). \quad (\text{II.57})$$

In Sec.IV.2.22 the magnitude of electric fields perpendicular to the magnetic field is estimated. The largest of them causes only a reduction of the signal amplitude by a factor 0.965 so that this effect is negligible.

The main effect causing the observed reduction of the signal amplitude of crossing X1 for higher electric fields is the admixture of S character into the $P_{1/2}$ states at the crossing. Since the S state does not contribute to the $Ly\alpha$ radiation, the interference terms at the crossing X1 in Eq.II.54 are reduced by the S admixture.

CHAPTER III

In this chapter the apparatus used in the level crossing experiment, the experimental procedure and the data processing are described.

The experiment was carried out in two parts. In the first part the $\text{Ly}\alpha$ resonance fluorescence radiation from the atomic beam was detected and the profile of the $\text{Ly}\alpha$ line as "seen" by the atoms in the beam was measured (Sec.III.1.3). The results were applied in the design of the second apparatus which was used for the detection of the level crossings X1 and X2.

III.1 Description of the apparatus

III.1.1 Vacuum system

In the design of the vacuum system for the second part of the experiment the following requirements had to be met:

- (i) The material must be non magnetic;
- (ii) Parts of the vacuum system must fit into the gap between the pole faces and between the coils of the 10" electromagnet;
- (iii) The pumping speed must be high enough to allow sufficient throughput of hydrogen at a reasonable background pressure;
- (iv) The distance between the hydrogen source and the interaction volume, where $\text{Ly}\alpha$ radiation and atomic beam intersect, must be as small as possible;
- (v) the distance between the $\text{Ly}\alpha$ lamp and the interaction volume must be as small as possible.

Fig.III.1 shows a photograph of the vacuum system made of aluminium ⁽¹⁾ which can be rolled out of the magnet gap on castors on the aluminium frames on both sides of the magnet without breaking the vacuum.

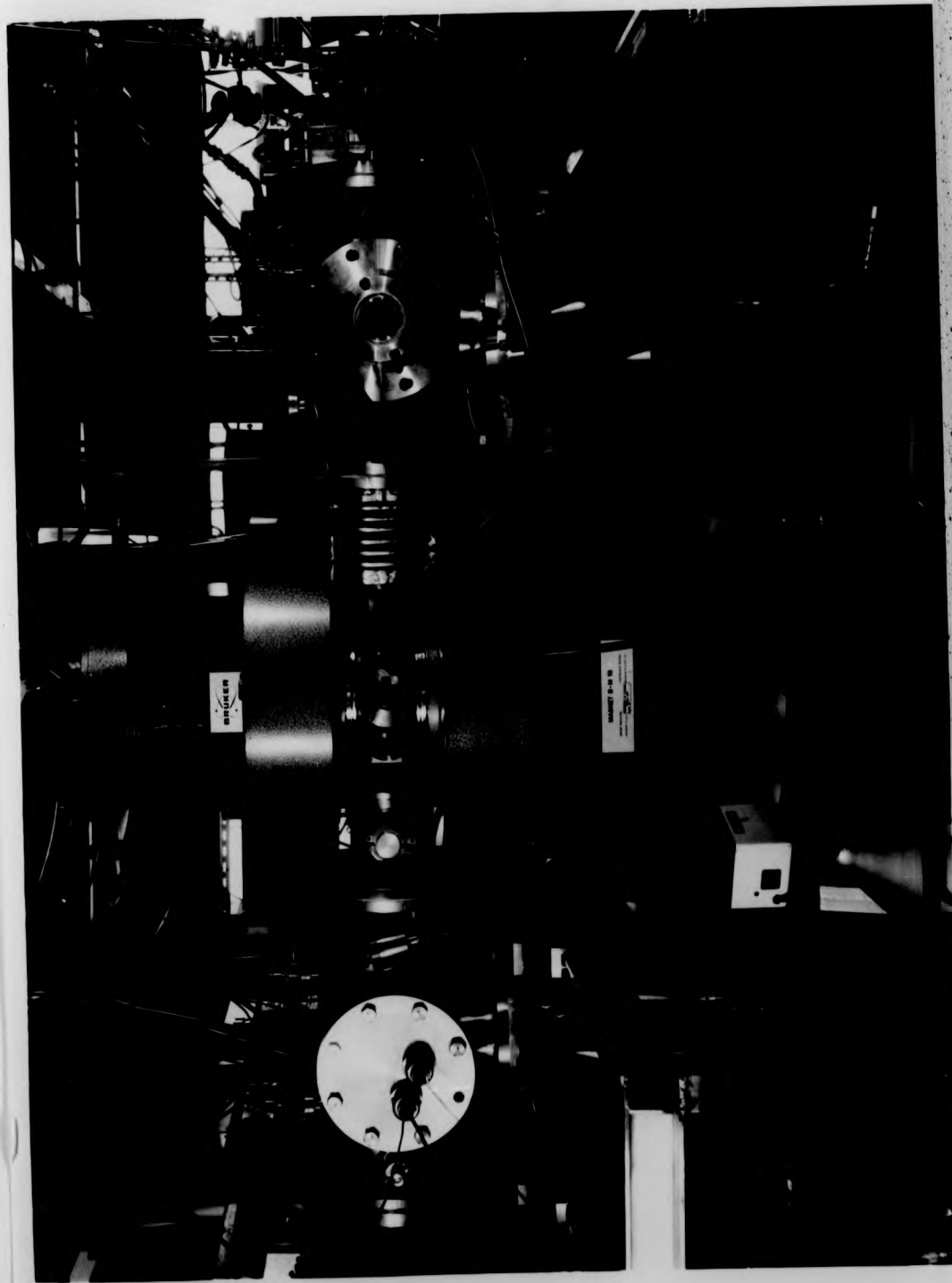
Fig.III.2 is a diagram of the 5 vacuum tanks which are called motor pump tank (MPT), motor tank (MT) in which the motor for the beam chopper is mounted, level crossing tank (LCT) which is only 56 mm high to fit into the gap between the magnet pole faces, the furnace tank (FT), and the furnace pump tank (FPT). Also shown is the furnace pipe supported by the end flange of the FPT and the window in the end flange of the MPT which allowed the observation of the furnace pipe for pyrometer measurements and alignment of the atomic beam with the help of a He-Ne laser.

The MPT and the FPT were fitted with 6" oil diffusion pumps (Edwards EO6) using Silicone 704 fluid, liquified gas-cooled traps (Edwards NTM6A), water cooled chevron baffles (Edwards CB6A), and pneumatic quarter swing butterfly valves (Edwards QSB6P). The backing pumps were rotary pumps type 1SC 450B (555 l/min) for the MPT and type ED660 (660 l/min) for the FPT.

The MT and FT were small enough to fit between the coils of the 10" electromagnet. The FT which contained the hydrogen beam source was water cooled to reduce thermal strain and avoid excessive heating of the rubber seals. FT and LCT were separated by a wall with a 3 mm diameter aperture for the atomic beam to allow differential

(1) N. Taylor (engineering) Ltd., Parkstone, Dorset.

Fig.III.1 Photograph of the atomic beam apparatus. The centre of the figure shows the 10" U-yoke electromagnet. The aluminium vacuum tanks (Fig.III.2) are supported by the framework on both sides of the magnet, and can be rolled out of the magnet gap on castors. The small level crossing tank (LCT) is shown inside the magnet gap with ports 3, 4 and 5 visible (Fig.III.3)



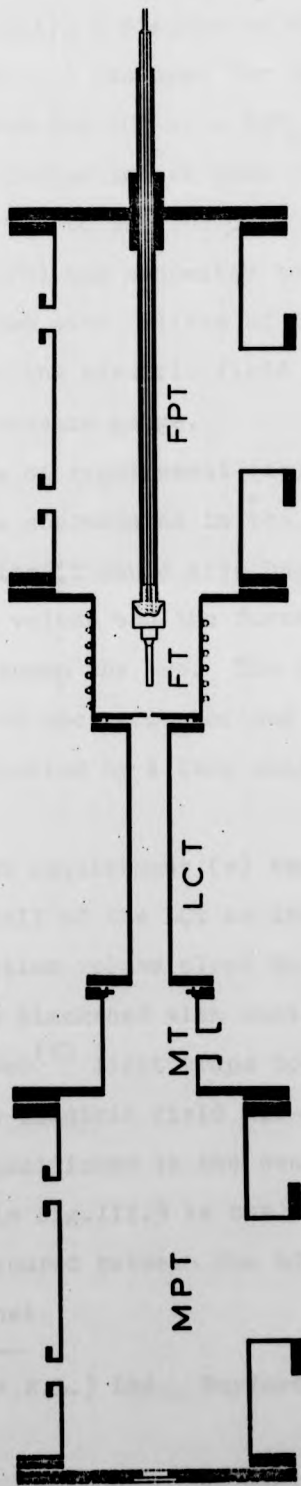


Fig.III.2 Diagram of the vacuum system viewed from the same direction as in Fig.III.1. The five aluminium vacuum tanks are

MPT Motor pump tank,

MT Motor tank,

LCT Level crossing tank,

FT Furnace tank,

FPT Furnace pump tank.

Also shown is the tungsten pipe of the hydrogen furnace and its support.

pumping.

In Fig.III.3 a diagram of the LCT and its 5 ports is shown. Port 1 was used for the $\text{Ly}\alpha$ lamp which was separated from the LCT by a MgF_2 window. Opposite the lamp the NO ionisation chamber (MONITOR) was sealed to port 5. At 90° to the incident $\text{Ly}\alpha$ light the photomultiplier (PM) was connected to port 2. Monitor and PM were fitted with filters of dry oxygen gas. Port 3 was used for the electric field condenser and port 4 carried a pressure gauge.

Because of requirement (iv) the chopper motor, which could not be accommodated in the LCT, was mounted in the MT. Otherwise it would have had to be placed between the interaction volume and the furnace, thus increasing the distance between the two. The chopper wheel was positioned in the recess of the LCT adjacent to the FT and was connected by a long shaft to the synchronous motor in the MT.

To meet requirement (v) the hydrogen beam travelled along the wall of the LCT as indicated in Fig.III.3 bringing the interaction volume close to the lamp. The inside of the LCT was blackened with soot and contained a number of black aeroweb⁽¹⁾ light traps to minimise the level of stray light. The electric field was provided by the condenser which was positioned in the centre of the magnet. Also indicated in Fig.III.3 is the outside NMR probe which in fact was secured between the LCT and the lower pole face of the magnet.

(1) CIBA (A.R.L.) Ltd., Duxford, Cambridge, England.

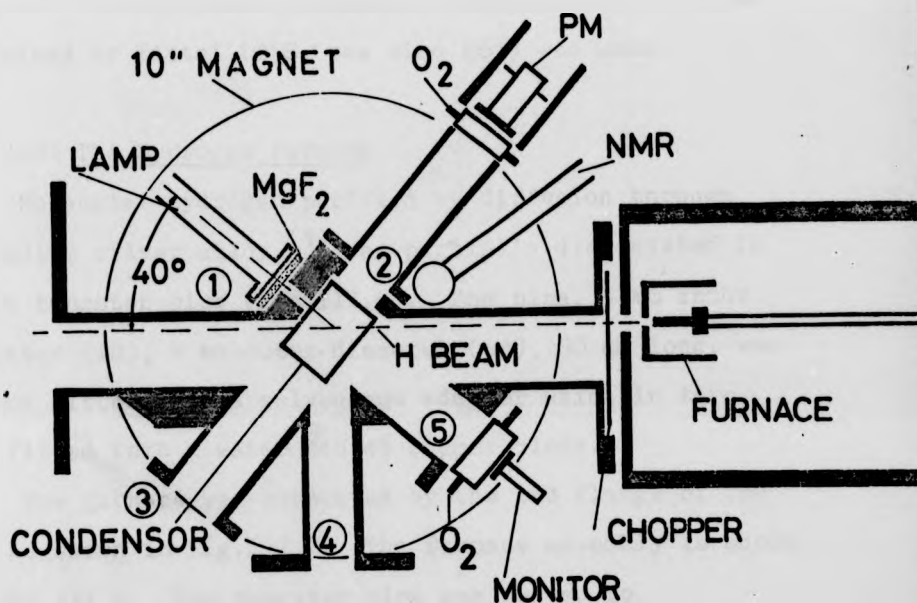


Fig.III.3 The level crossing tank (LCT) and its five ports. The Ly α lamp is connected to port 1, the photomultiplier (PM) to port 2. Port 3 is used for the support of the electric field condenser, port 4 for a pressure gauge and port 5 for the NO ionisation chamber. Also shown are the outside NMR probe, the position of the chopper wheel, the oxygen filters in front of the PM and NO chamber, and the FT with the tungsten pipe.

III.1.2 The hydrogen beam

A beam of atomic hydrogen was produced by thermal dissociation of molecular hydrogen on a hot tungsten surface. In this work a modified version of the furnace described by Tittel (T58, see also K61) was used.

III.1.21 The hydrogen furnace

Molecular hydrogen purified by diffusion through palladium silver alloy ⁽¹⁾ was partially dissociated in a hot tungsten pipe (Fig.III.4). The pipe, 3 mm inner diameter (id), 8 mm outer diameter (od), 60 mm long, was shrink fitted into a molybdenum adaptor which in turn was fitted into a water cooled copper block.

The furnace was supported by the end flange of the FPT as shown in Fig.III.2. The furnace assembly is shown in Fig.III.4. The tungsten pipe was heated to $T = (2400 \pm 150) \text{ K}^{(2)}$ by electron bombardment from two tungsten filaments of dimensions $55 \times 4 \times 0.05 \text{ mm}^3$. Pipe and filaments were surrounded by radiation shields. The filaments were suspended between the innermost molybdenum shield on one end and the molybdenum filament supports on the other. In Fig.III.4 the mounting of the molybdenum shield and the filament support are shown in the same plane, although they were in fact mounted at 45° , to accommodate a second filament and further shield mountings.

The filament supports were connected to the high voltage, high current feed throughs (Edwards Electrode 6D,

(1) Pd/Ag alloy with 23% Ag, 5 mm od x 0.1 mm wall was heated to approximately 400°C .

(2) The temperature was measured with an optical pyrometer (Pyrowerk GmbH) operating at 650 nm.

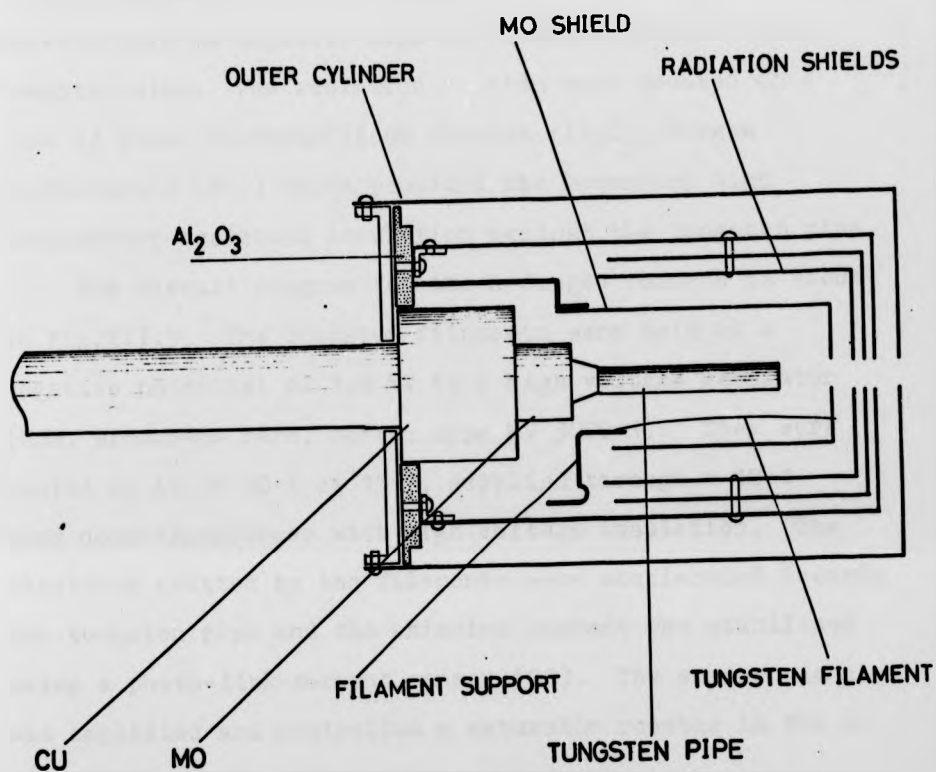


Fig.III.4 Furnace assembly

The tungsten pipe, supported by the molybdenum adaptor and the water cooled copper block, is heated by electron bombardment from the tungsten filaments. Radiation shields are employed to reduce the heat loss. The Al_2O_3 disc provides high temperature resistant insulation.

150 A, 10 kV DC rating) in the supporting flange by long stainless steel rods. The filaments and the four radiation shields were at negative high potential relative to the tungsten pipe. The radiation shields were mounted on a disc of Purox recrystallised alumina (Al_2O_3 , Morgan Refractories Ltd.) which provided the necessary high temperature resistant insulation against the tungsten pipe.

The circuit diagram for the hydrogen furnace is shown in Fig.III.5. The tungsten filaments were held at a negative potential of 1.8 kV by a high voltage generator (KSM, Brookmans Park, Herts; type HV 3000-1). They were heated by AC of 30 A at 15 V, supplied through a 10:1 step down transformer with high voltage insulation. The electrons emitted by the filaments were accelerated towards the tungsten pipe and the emission current was stabilised using a photo-link current sensor (CS). The sensor signal was amplified and controlled a saturable reactor in the AC supply line of the high voltage generator.

When operating the furnace close to the magnet the stray magnetic field may be as large as 1 kG at the front end of the FT for 4 kG at the magnet centre. Therefore, the filaments had to be arranged so that the path of the bombarding electrons was parallel to the magnetic field lines.

It was found that the alternating Lorentz force with an amplitude of the order of 0.2 N exerted on the filaments by the AC heating current destroyed the filaments within two hours. A soft iron cylinder was screwed to the FT to reduce the stray magnetic field thereby extending the life time of the filaments to 50 hours.

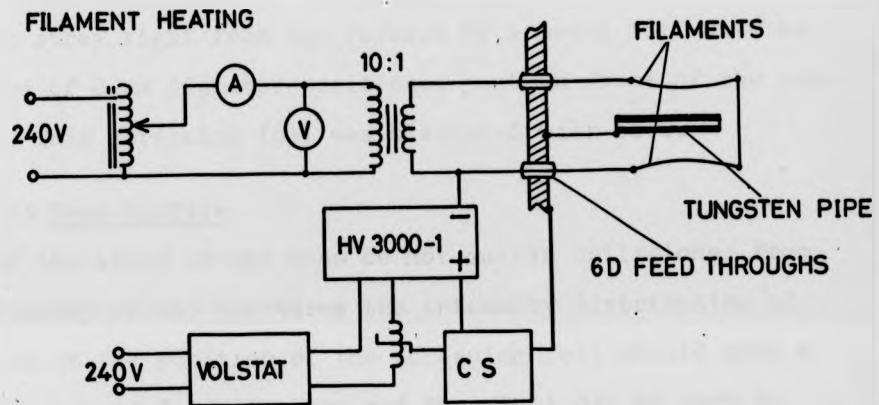


Fig.III.5 Circuit diagram for hydrogen furnace, showing the AC heating circuit of the tungsten filaments and the DC high voltage supply for the electron bombardment. The electron current is stabilised by a photo-link current sensor (CS) controlling a saturable reactor in the supply line of the DC high voltage generator.

III.1.22 Beam geometry

After leaving the hot tungsten pipe the atoms travelled 55 mm in the FT through openings in the radiation shields until they passed the 3 mm diameter differential pumping aperture. In the LCT they travelled a further 180 mm to the centre of the interaction volume. The interaction volume was screened against stray light from the furnace by a metal foil with an aperture of 8 mm diameter positioned just in front of the condenser. This screening foil was blackened with soot.

III.1.23 Beam profile

If the atoms in the beam do not suffer collisions, from the geometry of the apertures the intensity distribution of the beam at the position of the screening foil should have a flat maximum of 3 mm diameter and then fall off to zero at 18 mm diameter.

The only experimental indication of the beam profile was the appearance of concentric rings on the screening foil after exposure to the beam. The carbon layer on the foil showed discoloration forming an inner brownish ring of 10 mm od, another of 20 mm od and a faint greyish ring of 30 mm od. The diameter of the second ring agrees well with the expected outer diameter of the beam of 18 mm. The 10 mm ring could possibly be caused by atoms being scattered out of the 3 mm beam core by small angle scattering. Similarly the 30 mm ring may be caused by small angle scattering out of the whole beam.

Although the gas kinetic mean free paths for the pressures under operating conditions of $p_{\text{FPT}} = 2 \cdot 10^{-4}$ Torr and $p_{\text{LCT}} = 3 \cdot 10^{-5}$ Torr are about $\lambda_{\text{FPT}} = 50$ cm and $\lambda_{\text{LCT}} = 5$ m, for the small angles involved of 1° to 2° ,

the mean free path may be as short as 5 cm because of a steep increase of the collision cross section for small angles (Ra56)..

III.1.24 Beam density

The number density N of hydrogen atoms in the beam at the interaction volume determines the rate of scattered $\text{Ly}\alpha$ photons. This density may be estimated from the known geometry and the total throughput of gas calculated from the pumping speed, the conductance of the tanks, and the equilibrium pressure⁽¹⁾.

The number of molecules per second $d\dot{M}$, leaving an oven through an orifice into the solid angle $d\Omega$ is,

$$d\dot{M}(\theta) = \frac{N_0 \bar{v} A}{4\pi} \cos \theta d\Omega, \quad (\text{III.1})$$

where θ is the angle between the straight through direction and the solid angle,

N_0 is the number density of atoms in the oven,

\bar{v} is the magnitude of their mean velocity in the oven,

A is the area of the orifice (Ra56).

This formula was derived assuming that the mean free path is long compared with the orifice dimensions. It was also assumed that the oven conditions are not affected by the loss of particles, an assumption which is fulfilled when the furnace has reached a steady state.

In the forward direction the rate is

$$d\dot{M}(0) = N_0 \bar{v} A d\Omega / 4\pi = \dot{M} d\Omega / \pi, \quad (\text{III.2})$$

where \dot{M} is the total rate of molecules leaving the orifice.

(1) The pressure was determined using an ionisation gauge Balzers ING2 with gauge head IMR3, correcting the reading with the calibration factor 2.2 for hydrogen.

The total rate of atoms and molecules leaking into the FPT can be found by calculating the pump throughput from the estimated pumping speed of $\dot{V}_{H_2} = 400$ l/s and the equilibrium pressure in the FPT of $p_{FPT} = 2.2 \dots 4.4 \cdot 10^{-4}$ Torr, and expressing the throughput in terms of molecules per second using the ideal gas equation,

$$\dot{M} = p_{FPT} \dot{V}_{H_2} / kT = 2.8 \cdot 10^{18} \text{ atoms/s.} \quad (\text{III.3})$$

Assuming a degree of dissociation $D_H = 50\%$, \dot{M} also is the number of hydrogen atoms leaving the tungsten pipe per second. Only a small fraction of the H atoms arrives at the centre of the interaction volume at a distance of $R_B = 235$ mm from the tungsten pipe, where it forms a target for the Ly α radiation with a number density,

$$N_T = \dot{M} / \pi R_B^2 \bar{v} = 1.9 \cdot 10^9 \text{ atoms/cm}^3. \quad (\text{III.4})$$

In Eq. III.4 the mean velocity of the atoms in the beam,

$$\bar{v} = \sqrt{\frac{9\pi}{8} \frac{kT}{m_0}} = 8.4 \cdot 10^5 \text{ cm/s,} \quad (\text{III.5})$$

has been inserted.

Because of the collimating effect of the tungsten pipe the beam density should be higher than that calculated for an orifice. The effectiveness of the collimation by the pipe is expressed by the factor $1/k$ which gives the ratio between the total number of molecules passing through the pipe to the total number passing through an orifice with the same area for the same flow in the forward direction. Zugenmaier (Z66) obtained for $1/k$ the equation,

$$1/k = \frac{2\gamma(2/3 - \delta/4)}{1 + \delta(2/3 - \delta/4)}, \quad (\text{III.6})$$

which holds for $\gamma = 2a/L < 0.5$, where $2a$ is the diameter and L is the length of the pipe. Eq.III.6 is valid as long as collisions inside the pipe may be neglected, i.e. as long as $\lambda \gg L$, where λ is the mean free path.

If this condition is only fulfilled for part of the pipe, only that part acts as collimator. Then the intensity in the forward direction is proportional to the square root of the total throughput,

$$\dot{M}_p(0) \, d\Omega \sim \sqrt{\dot{M}} \, d\Omega. \quad (\text{III.7})$$

Assuming a linear variation of the density in the pipe it can be estimated that $\lambda \approx L$ is valid at 2.4 cm from the pipe output for hydrogen atoms.

Thus for the collimating part of the pipe $\gamma = 0.14$, which leads to $1/k = 0.163$, and the target density is then

$$N = N_p k = 1.2 \cdot 10^{10} \text{ atoms/cm}^3. \quad (\text{III.8})$$

This number should be regarded as an order of magnitude estimate only, because of the considerable uncertainty chiefly in the value for the throughput.

It should be pointed out that the estimate of the beam density merely helps to understand the operation of the apparatus. It is used in Sec.III.1.4 to estimate the $\text{Ly}\alpha$ resonance fluorescence count rate, but a knowledge of the beam density is not essential for the Stark effect measurement.

III.1.25 Dissociation of H₂

To find the best experimental conditions the beam emanating from the tungsten pipe was investigated with a quadrupole mass spectrometer.

The hydrogen beam was chopped at a frequency of 70 Hz and a lock-in amplifier was used to separate the response of the mass spectrometer to the beam from its response to the unmodulated residual gas which consisted mainly of molecular hydrogen. It was found that the ratio of the signals for mass 1 and mass 2, R_{12} , obtained for the beam increased with heating power P supplied to the tungsten pipe and decreased with larger hydrogen throughput.

Typical values are listed in Table III.1.

P_{FPT}/Torr	P/W	R_{12}
$2 \cdot 10^{-5}$	930	3.2 ± 1.1
$2 \cdot 10^{-4}$	930	1.0 ± 0.3
$7 \cdot 10^{-5}$	1000	2.2 ± 0.3
$7 \cdot 10^{-5}$	650	1.1 ± 0.4

Table III.1 Typical values for the pressure in the FPT, P_{FPT} , heating power P , and ratio R_{12} .

From the ratio R_{12} the dissociation fraction, $D_H = (N_1/2)/(N_1/2 + N_2)$, can be calculated from,

$$D_H = (1 + (Q_1/Q_2) \sqrt{2}/R_{12})^{-1}, \quad (\text{III.9})$$

where N_1 and N_2 are the atomic and molecular number densities, and Q_1 and Q_2 are the cross sections for ionisation of atoms and molecules by electrons in the mass spectrometer.

In the derivation of Eq.III.9 a constant supply of molecular hydrogen to the furnace was assumed (FB58).

However, for this experiment the density of atomic hydrogen at the interaction volume itself is more important than the degree of dissociation, because the scattering of $\text{Ly}\alpha$ photons by H_2 molecules can be estimated to be smaller by several orders of magnitude from the experiment by Heddle (H62).

An absolute determination of the atomic hydrogen density was not possible with the mass spectrometer, because the collection efficiency of the crossed beam arrangement was unknown. To find the best experimental conditions the mass 1 signal was observed as a function of the heating power and ^{as a function of} the pressure in the FPT used as a measure for the hydrogen throughput. Fig.III.6 shows the signal for mass 1 versus heating power P. The experimental points indicate a saturation effect at 800 W corresponding to a temperature of approximately 2200 K. For higher hydrogen throughput the saturation occurred at higher heating power so that most experiments were carried out choosing the heating power to lie between 800 and 1000 W.

Fig.III.7 shows the signal for mass 1 as a function of the hydrogen throughput at $P = 800$ W. The nonlinear behaviour was to be expected from Eq.III.7 and because of a decrease of the dissociation with increasing throughput.

The level crossing experiments were mostly run at $P_{\text{FPT}} = 2.2 \dots 4.4 \cdot 10^{-4}$ Torr with a ratio of about $R_{12}(900\text{W}) = 1$ and $D_{\text{H}} = 50\%$. The throughput was limited by the

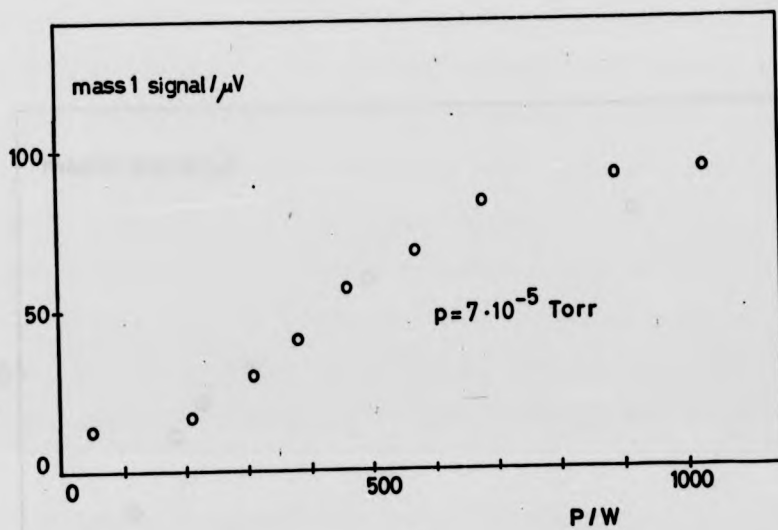


Fig.III.6 Mass 1 signal of mass spectrometer versus heating power P applied to the tungsten pipe.

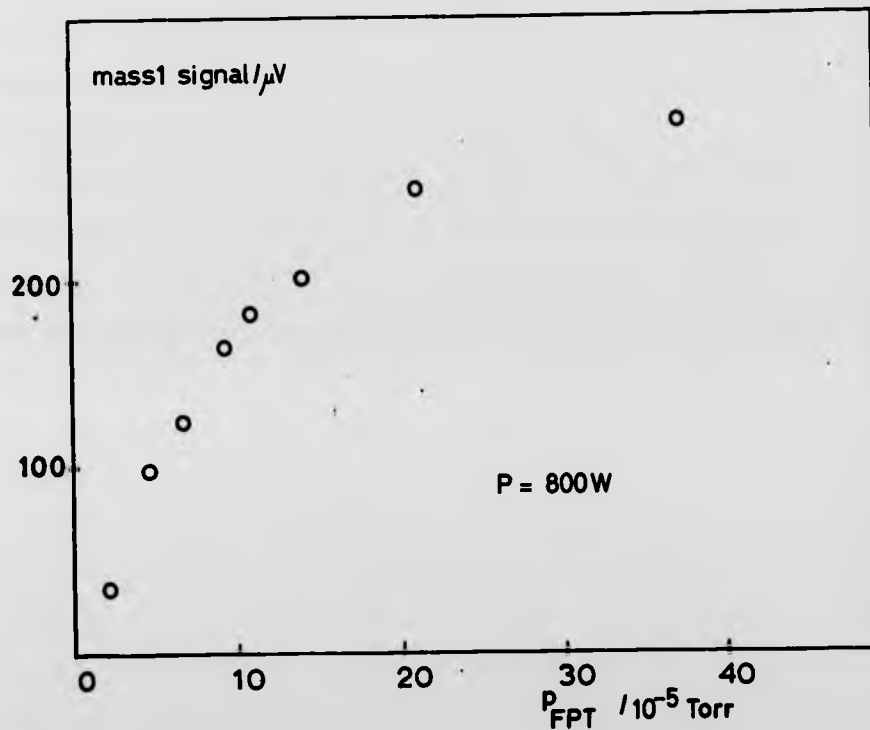


Fig.III.7 Mass 1 signal of the mass spectrometer versus hydrogen throughput measured by the equilibrium pressure in the furnace pump tank, P_{FPT} .

pressure in the backing line, which for $p_{\text{FPT}} = 4.4 \cdot 10^{-4}$ Torr was close to the recommended maximum of 0.5 Torr.

Other sources for a dense beam of atomic hydrogen were also investigated. With a view to using glass capillaries for beam collimation a number of discharge sources were compared with the high temperature dissociation furnace. The dissociation of the discharge sources was generally found to be lower and the mass 1 signal smaller by a factor of 10 for similar throughput.

The possibility of a high temperature multi-channel array has been considered but not been taken up because firstly, the manufacture is difficult and the results are not always convincing (K67), and secondly the channel walls block part of the area available for the beam.

III.1.3 The Ly α lamp

The Ly α light was produced in an electrodeless microwave powered discharge of helium with a small admixture of hydrogen.

A variety of different microwave cavities were investigated experimentally and the type 5 described by Fehsenfeld et al (FEB65) was found to be the most reliable, maintaining the discharge over the widest pressure range. However, for operation inside the magnet the cavity had to be modified and the modified version was always very difficult to tune for stable operation. About 20 W of microwave power supplied by a microtron 200 (Electro Medical Supplies (Greenham) Ltd.) at a frequency of 2.45 GHz were absorbed in the lamp cavity.

The discharge was confined to a quartz tube, 13 mm od and 1.5 mm wall with a 3 mm thick flange attached to one end. The flange was sealed to a polished MgF₂ window of 25 mm od and 2 mm thickness (Harshaw Chemicals Ltd., Daventry), which in turn was sealed to port 1 of the ICT. Both seals were made with 2 mm diameter indium wire.

The other end of the quartz tube was connected to a 2.5 l brass vacuum tank which could be evacuated to $1 \cdot 10^{-6}$ Torr by an Edwards 2" pump system. The evacuated brass tank and the quartz tube could be refilled through needle valves with helium, which was purified in a liquid nitrogen cooled charcoal trap, and hydrogen which was purified by diffusion through Pd/Ag alloy. For normal operating conditions the lamp was filled with 0.033 Torr H₂ and 1.6 Torr He as measured by Pirani gauge (Edwards

Vacuum gauge B9) correcting the readings according to the calibration chart supplied.

III.1.31 Lamp spectrum

The lamp spectrum was investigated using a grating spectrograph (1) which was evacuated to $1 \cdot 10^{-5}$ Torr. A MgF_2 coated grating blazed for 300 nm with 2400 grooves per mm was used and the spectrum was observed in second order.

With the NO ionisation chamber as detector in the range from 115 nm to 135 nm the $\text{Ly}\alpha$ line and about ten other lines were recorded. Most of them could be attributed to the OI and CI spectra. Their intensity was reduced by a factor 2 to 3 to about 1% of the $\text{Ly}\alpha$ intensity when the tank helium was purified in the cooled charcoal trap. When viewed through an oxygen filter (2) the intensity of the $\text{Ly}\alpha$ light was reduced by a factor of 3 and the intensities of the other lines were diminished to less than $3 \cdot 10^{-4}$ of the $\text{Ly}\alpha$ light.

A wider range of the spectrum was observed by using the EMR photomultiplier (ASCOP 542G-08-18B) which has a quantum efficiency of 10% at 121.6 nm and of 0.1% at 210 nm. A number of strong groups of lines and bands were detected, particularly in the range 135 nm to 165.5 nm. Their total intensity was much larger than that of the $\text{Ly}\alpha$ and rendered futile any attempt to detect the $\text{Ly}\alpha$ resonance

(1) The spectrograph was a McPherson model 218 which is a 0.3 m, f/5.3; plane grating scanning monochromator with crossed Czerny-Turner arrangement.

(2) The " $\text{Ly}\alpha$ window" in the O_2 absorption is

$\Delta\gamma = 4 \cdot 10^{12}$ Hz (L55) wide, which is broad compared to the $\text{Ly}\alpha$ line width (Sec.III.1.33).

fluorescence. However, when the oxygen filter was placed in front of the PM the intensity of each of the unwanted lines was reduced by a factor of 300 or more. The oxygen filter also helped to reduce the background radiation from the hydrogen furnace whose spectrum showed a broad maximum at 140 nm and some broad lines at 160 nm.

III.1.32 Lamp intensity

In the level crossing experiments the Ly α intensity was continuously monitored by the NO ionisation chamber connected to port 5 of the LCT. The ion current was amplified by an electrometer (Keithly 610C) and recorded on a chart recorder (Bryans Ltd., 27000 series).

The NO chamber was also used to find the best lamp conditions for stable and intense Ly α output. Lower pressure in the lamp generally allowed the discharge to spread out further from the cavity producing a higher Ly α intensity since the discharge was closer to the window. However, this discharge mode was not reliable and large sudden fluctuations could occur. Higher H₂ admixture reduced the Ly α output but had a stabilising effect. A compromise between the conflicting requirements of high Ly α output and stable operation was sought and under normal operating conditions the short term fluctuations were approximately 3% of the total intensity.

In addition, long term variations of the Ly α intensity were observed which in most cases took the form of decrease of the output.

As is well known (Wa62) the performance of optical components in the VUV deteriorates with time, the rate depending on the duration and intensity of irradiation and

on the composition and pressure of the residual gas.

When LiF or MgF₂ windows are used a brownish deposit is often observed (M68). Some authors blame the deposit on the sealing material and this was confirmed here for rubber O-rings and for materials such as araldite when they were exposed to the discharge (Wa62,B67). This deposit on the lamp side of the window was reduced when indium was used for sealing and the seal moved away from the discharge. The brownish deposit formed on the outside is probably due to decomposition of residual organic vapours (WB65,RMJ69). The windows can be cleaned with putty powder but the full Ly α transmission cannot be recovered. In addition LiF forms colour centres when irradiated with strong UV light (N67, Wa65). The colour centres can be removed by annealing the crystals at 400°C as recommended by Warneck (Wa65).

Because MgF₂ is less fragile than LiF and has a slower rate of deterioration, MgF₂ was preferred for the lamp window. In the O₂ filters the cheaper LiF windows were used since they are exposed here to much lower UV intensity.

The Ly α output of the lamp was also decreased by some aging effect of the gas filling. Therefore the gas was renewed during the experiments at regular intervals. The ratio of the two effects reducing the Ly α intensity changed with time as the window contamination seemed to reach a stable condition, a factor of 100 below the initial intensity.

Furthermore, the Ly α intensity depends on the magnetic field. The field had a desirable stabilising effect but tended to restrict the discharge to a small volume inside

the cavity thereby reducing the $Ly\alpha$ output. The current from the ionisation chamber measured for the range of magnetic fields of interest in this experiment is shown in Fig.III.8 (open circles). The total decrease is about a factor of 3 between zero magnetic field and 5000 G.

Also shown in Fig.III.8 are the experimental count rates for scaler A (S+F+L+U), and scaler B (L+U) (See Sec.III.1.7 for definition of S,L,F, and U.). All three curves decrease with increasing magnetic field but not with the same rate. This gives an indication that I_{NO} cannot be used for normalisation of the count rates measured at different $Ly\alpha$ intensities (Sec.III.3.3) as was originally planned.

The radiance of the lamp for $Ly\alpha$ may be estimated from the current measured in the NO chamber. At the exit of the monochromator, for input and output slit areas of $df = 1 \text{ mm}^2$, the current was $I_{NO} = 1.2 \cdot 10^{-11} \text{ A}$, measured for normal working conditions of the lamp in the absence of the oxygen filter. Taking into account a loss factor of 0.2 in the monochromator due to multiple reflection and the 40% sensitivity of the NO chamber (S67), the current corresponds to a photon flux $I_{\gamma} = 9.4 \cdot 10^7 \text{ Ly}\alpha/\text{s}$. The radiance J can be calculated from,

$$I_{\gamma} = J df d\Omega . \quad (\text{III.10})$$

Inserting the solid angle $d\Omega = 2.2 \cdot 10^{-2} \text{ sd}$, of the monochromator, the value

$$J = 4.3 \cdot 10^{11} \text{ Ly}\alpha/\text{s sd cm}^2 \quad (\text{III.11})$$

is obtained.

COUNTRATE
 10^3 counts/s

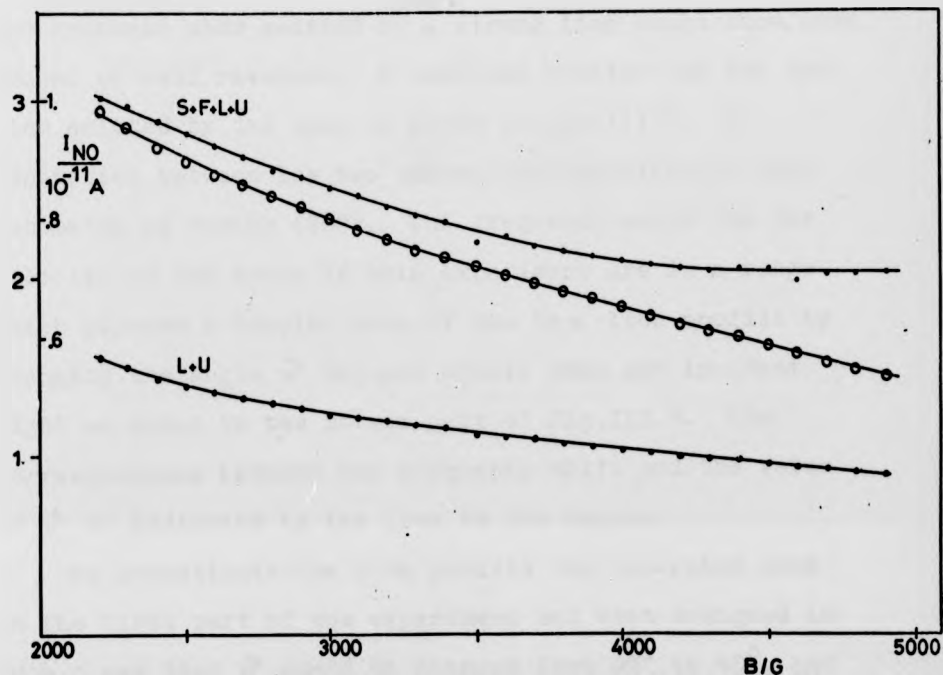


Fig. III.8 Ly α intensity measured by the NO chamber as a function of the magnetic field strength (open circles). The ordinate is given by the inside numbers 0.6 to 1.0 10^{-11} A. Also shown are the corresponding experimental count rates (dots). The upper curve is the resonance fluorescence count rate S plus all backgrounds, the lower curve is the sum of the constant dark rate U and the lamp background L. F is the furnace background. For these curves the outside ordinate 1 to 3 10^3 counts/s is valid.

III.1.33 Ly α line profile

It was to be expected that the main resonance line of the hydrogen atom emitted by a strong lamp would show some amount of self reversal. A possible profile for the Ly α line emitted by the lamp is shown in Fig.III.9. The separation between the two maxima is approximately that estimated by Vanier (V67). The frequency scale and the velocity of the atoms in this experiment are in a range which allowed a Doppler scan of the Ly α line profile by changing the angle \mathcal{V} between atomic beam and incident light as shown in the bottom part of Fig.III.9. The correspondence between the frequency shift and the value of \mathcal{V} is indicated by the line in the centre.

To investigate the line profile the apparatus used in the first part of the experiment had been designed in such a way that \mathcal{V} could be changed from 90° to 40° , and 8 positions from $\mathcal{V}_1 = 90^{\circ}$ to $\mathcal{V}_8 = 40^{\circ}$ were used in the measurement.

At an angle $\mathcal{V}_1 = 90^{\circ}$ the velocity component of the atoms in the beam towards the lamp is small and the atoms absorb photons from a narrow frequency band centred around the mid frequency ν_0 of the Ly α line. At the angle $\mathcal{V}_3 = 40^{\circ}$ there is a considerable velocity component towards the lamp and the atoms absorb from a wider frequency band around $\nu_0 + \Delta\nu_D$, where $\Delta\nu_D$ is the Doppler shift. The Doppler shift can be calculated from,

$$\Delta\nu_D(\mathcal{V}) = \nu_0 v_B \cos\mathcal{V}/c, \quad (\text{III.12})$$

where $\nu_0 = 2.466 \cdot 10^{15}$ Hz is the mid frequency of Ly α , v_B is the velocity of the atoms in the direction of the beam,

LAMP PROFILE

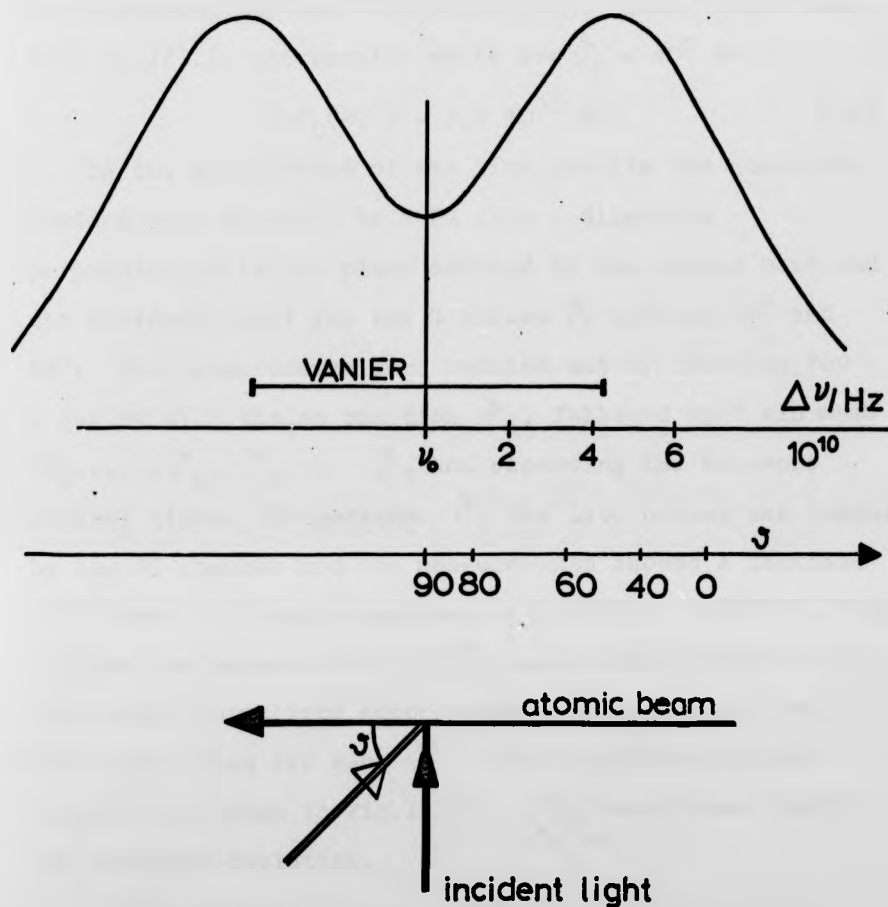


Fig.III.9 Schematic diagram of the Ly α line profile and the Doppler shift of the centre absorption frequency of the atoms in the beam for variable angle ν between atomic beam and incident Ly α radiation.

and c is the velocity of light. Neglecting the velocity of the atoms perpendicular to the beam which is only $0.02 v_B$ and inserting the mean velocity of the atoms in the beam from Eq.III.5, the Doppler shift for $\psi_8 = 40^\circ$ is,

$$\Delta \nu_D(40^\circ) = 5.3 \cdot 10^{10} \text{ Hz.} \quad (\text{III.13})$$

In the measurement of the line profile the scattered photons were observed by a PM from a direction perpendicular to the plane defined by the atomic beam and the incident light for the 8 values ψ_i between 90° and 40° . The measurements were carried out by counting for a period of 1 min at position ψ_1 , followed by 1 min each at $\psi_2 \dots \psi_8, \psi_8 \dots \psi_1$ and repeating the sequence several times. In position ψ_1 the $\text{Ly}\alpha$ output was measured by the NO chamber and the measurements showed a decrease with time. A linear dependence of the $\text{Ly}\alpha$ output on time between the measurements at ψ_1 was assumed and the count rates were normalised accordingly. Then the mean values of the count rates for each ψ_i were calculated and the results are shown in Fig.III.10. The error bars indicate one standard deviation.

The different curves in Fig.III.10 were measured maintaining different conditions for the lamp. The curve marked (1) was obtained for normal working conditions, the curve (2) for a discharge excited in helium without deliberate admixture of hydrogen, curve (3) for an increased distance between the discharge and MgF_2 window and curve (4) for a larger hydrogen admixture than normal. All profiles show self absorption and the minimum at the line centre is more pronounced in the cases (3) and (4) where more hydrogen atoms were present in the gap between the light emitting discharge and the MgF_2 window.

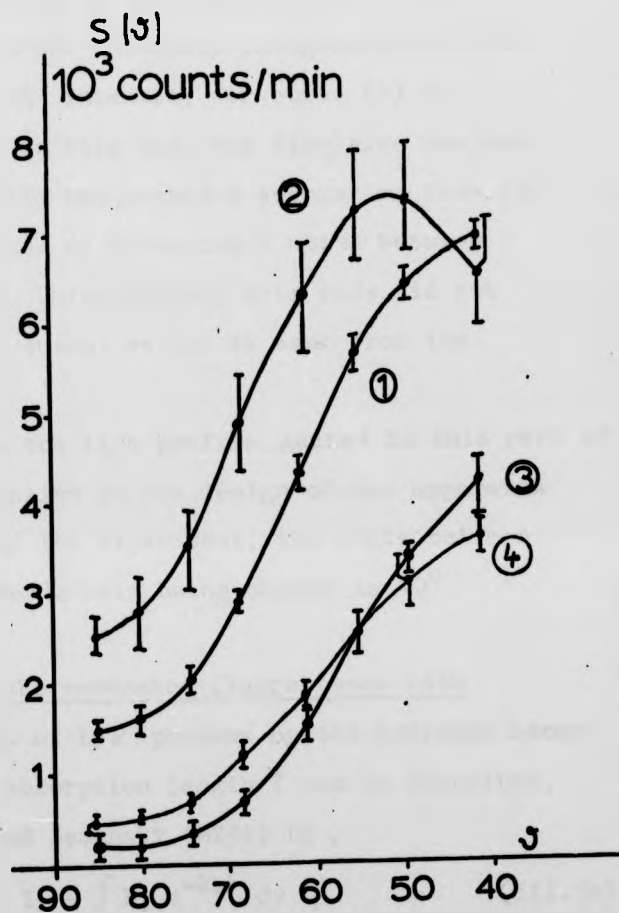


Fig.III.10 Experimental Ly α line profile.
 The fluorescence count rate S as a function of the angle j between atomic beam and incident Ly α light. The curves (1)....(4), obtained for different conditions of the lamp, show all strong self reversal.

Comparison of the total intensities shows that for (1) the Ly α intensity is larger than for (3) and (4). This observation was confirmed by measurements with the NO chamber which measures the intensity integrated over the whole line profile. The intensity for curve (2) is higher still, because in this case the discharge was not restricted to the cavity but expanded several mm from it, thus reducing the number of absorbing H atoms between discharge and window. Unfortunately this mode did not provide a stable Ly α output as can be seen from the larger error bars.

The knowledge on the line profile gained in this part of the experiment was applied in the design of the apparatus for the second part of the experiment, the angle between incident light and atomic beam being chosen as 40°.

III.1.4 Estimate of the resonance fluorescence rate

The absorption A of Ly α photons by the hydrogen atoms in the beam with an absorption length l can be described, following Mitchell and Zemansky (MZ34) by ,

$$A I_0 = I_0 - \int E_\nu e^{-k_\nu l} d\nu , \quad (\text{III.14})$$

where k_ν is the absorption coefficient of the atomic beam and $I_0 = \int E_\nu d\nu$ is the total number of Ly α photons arriving at the atomic beam integrated over all emission frequencies of the lamp.

I_0 can be estimated assuming that the lamp emits uniformly over its whole surface of $F = 0.5 \text{ cm}^2$, approximating the real geometry by a solid angle of $d\Omega = 0.13 \text{ sd}$, and using J of Eq.III.11 to give

$$I_0 = 2.8 \cdot 10^{10} \text{ Ly}\alpha/\text{s} . \quad (\text{III.15})$$

To simplify the analysis the Ly α profile (Sec.III.1.33) is approximated by a uniform spectral distribution E_0 of width $\Delta\nu_L$ writing,

$$I_0 = E_0 \Delta\nu_L .$$

The width $\Delta\nu_L$ is estimated from Fig.III.9 and 10 as,

$$\Delta\nu_L = 10 \cdot 10^{10} \text{ Hz.}$$

For small ($k_\nu l$) the exponential in Eq.III.14 can be expanded to give,

$$AI_0 = \int E_\nu k_\nu \ell \, d\nu \quad (\text{III.16})$$

It follows that,

$$AI_0 = \frac{I_0}{\Delta\nu_L} \ell \int k_\nu \, d\nu \quad (\text{III.17})$$

The integral of the absorption coefficient over all frequencies is known from,

$$\int k_\nu \, d\nu = \frac{\lambda_0^2}{8\pi} \frac{g_2}{g_1} \frac{N}{\tau} = 13.5 \cdot 10^{-3} \cdot N \cdot \text{cm}^2 \text{s}^{-1}, \quad (\text{III.18})$$

where λ_0 is the wavelength of the absorbed radiation, g_1, g_2 are the statistical weights of ground and excited states,

N is the number density of the atoms, and

τ is the lifetime of the excited state.

The numerical result is given for Ly α .

Using the estimate for N from Eq.III.8 and for the absorption length $\ell = 0.8 \text{ cm}$, the rate of absorption becomes,

$$A I_0 = 3.6 \cdot 10^7 \text{ Ly}\alpha/\text{s}, \text{ equivalent to } A = 1 \cdot 10^{-3}.$$

The small value of A justifies the expansion of Eq.III.14. The calculated rate of absorption implies that, on average, every 30 ns an excitation process occurs with subsequent decay within 1.6 ns. So, at any instant of time, at most

one H atom in the interaction volume is in the excited state.

Since the excited atoms travel less than $1.4 \cdot 10^{-3}$ cm during their lifetime almost all of them decay in the interaction volume. Only a small fraction γ of the re-emitted photons contributes to the fluorescence count rate. The fraction is $\gamma = 7 \cdot 10^{-6}$, taking into account the solid angle of the detector, the efficiency of the PM, and the absorption by the O_2 filter and its windows.

Including also the reduction of I_0 by the magnetic field a count rate of 500 counts/s is estimated. Considering the number of crude approximations made and the lack of knowledge about the window contaminations, the estimate is quite consistent with the experimental rates which lie between 500 and 3000 counts/s.

III.1.5 The magnetic field

The magnetic field was produced by a 10" electro-magnet with variable air gap (Bruker B-M 10). The magnet had a single yoke which allowed the movement of the LCT in and out of the air gap. The magnet coils were powered by a current stabilised 6 kW power supply (Bruker B-MNS 150/40 SI6s) with a short term stability of $\Delta I/I_0 \leq 1 \cdot 10^{-6}$.

III.1.51 Measurement of the magnetic field strength

The magnetic field strength was measured with a nuclear magnetic resonance (NMR) gaussmeter (AEG) with an accuracy of 10 ppm.

The gaussmeter produced two signals on an oscillograph which had to be adjusted to coincide. The width of the two signals depends on the homogeneity of the magnetic field

over the volume of the cylindrical probe with radius of 8.5 mm and a height of 3.5 mm. The minimum width of the signals is equivalent to an inhomogeneity of 0.3 G and increases for higher inhomogeneity up to 3 G when the two signals disappear.

III.1.52 Homogeneity of the magnetic field

Iron ring shims were attached to the pole faces to partly correct for the edge decay of the magnetic field. With the air gap set to its maximum value of 65 mm the profile of the field was measured. The field strength was found constant to better than 0.6 G within a cylindrical volume of radius $r = 30$ mm and a height of 30 mm for a field of $B_0 = 3700$ G at the magnet centre.

Unfortunately the use of iron shields to protect the PM and the tungsten filaments in the furnace from stray magnetic fields reduced the homogeneity. However the shields could be arranged in such a way that for $B_0 = 3500$ G the deviation of the magnetic field inside the electric field condenser was (0.2 ± 0.2) G. This result was supported by the fact that no broadening of the NMR signals could be detected when the probe was positioned inside the interaction volume.

III.1.53 Stabilisation of the magnetic field

The magnetic field strength was monitored and stabilised during the experiments by a NMR probe outside the LCT placed between the LCT and the lower pole face. The difference ΔB_p of the magnetic field strength measured by the outside probe and the value measured by

another probe at the interaction volume was investigated. It was found,

$$\Delta B_p = (0.11 \pm 0.25) G,$$

where the uncertainty includes all hysteresis effects appearing when the field was changed in steps of 500 G up to 5 kG. Changing the magnetic field in smaller steps, as used in the experimental runs, produced smaller hysteresis effects.

In most of the experimental runs the magnetic field was held constant during one counting period T_M and altered stepwise for the next. During each counting period the magnetic field was stabilised at the desired field strength. An error voltage was provided by the NMR gaussmeter depending on the difference between the desired field value and the measured field strength. The error voltage was fed through an interface to the modulation input of the magnet power supply. The stabilisation obtained was better than 10 ppm.

III.1.6 The electric field

The crossing positions were measured in a number of experiments employing different parallel plate condensers to generate the electric field. In the most precise experiment, called LC4, the electric field was generated in a condenser formed by two copper plates with an area of $36 \times 47 \text{ mm}^2$ and a gap of 8 mm. The plates were each connected to a coaxial high voltage vacuum feed-through.

The gap between the plates was determined by four boron nitride spacers to which the plates were tightly pressed by nylon screws. The plates were each supported by a pair of stainless steel 3 mm threaded rods which were

screwed to a perspex block. The perspex block was mounted on the 1/2" drive shaft of a rotary shaft vacuum seal (Edwards). This allowed adjustment of the angle between the electric and magnetic fields. The plates were adjusted visually so that the fields were parallel.

III.1.61 The condenser gap

In Table III.2 the name of the experiment, the value of the condenser gap d , and the relative uncertainty of d are listed.

Experiment	d/mm	$\Delta d/d$
MR5	10.8	7.4%
LC1	10.8	1.9%
LC2,3	8.2	2.4%
LC4	8.113	0.75%

Table III.2 The value of the condenser gap d used in different experiments and its relative uncertainty.

For experiment LC4 the gap between the condenser plates was measured with a travelling microscope. The average of several measurements along both 47 mm long edges of the plates carried out before and after experiment LC4 did not differ significantly. The mean value for the width of the gap and its standard deviation were,

$$d = (8.113 \pm 0.005) \text{ mm.}$$

Measurements of the gap inside the condenser with calipers and micrometer resulted in,

$$d = (8.131 \pm 0.014) \text{ mm.}$$

It was apparent from the measurements that the value for d should lie within the limits

$$8.07 < d/mm < 8.17 .$$

These limits include the different results obtained by different persons.

For data analysis, $d = 8.113$ mm has been adopted with an estimated uncertainty of $\pm 0.75\%$.

In the other experiments the condenser gap was less well defined, as shown in Table III.2.

III.1.62 Condenser voltage

The voltage was supplied to the plates by a regulated power supply (Fluke 408B, 0...6 kV) connecting one plate to ground potential and the other to high voltage.

The accuracy of the Fluke supply is specified to be 0.25% with a repeatability of 0.05% and stabilisation of 5-10 ppm/hr. In the range between 100 V and 1100 V the output voltage was measured by a digital voltmeter (DVM, Solartron) and the difference of the value set on the power supply and the DVM measurement was found to be of order of 0.2%. The voltages used in the experiments were corrected accordingly and the uncertainty of the corrected voltages is $\pm 0.12\%$, which accounts for the error of the DVM measurement of 0.07% and the repeatability of the power supply setting.

III.1.63 Fringe field effects

The electric field for infinite condenser plates may be calculated according to,

$$E_0 = U/d, \quad (\text{III.19})$$

where U is the applied voltage and d the condenser gap. For a practical condenser the fringe effect must be considered. The fringe fields outside the condenser do not disturb the experiment but help to quench any metastable atoms that might have been generated in the

FT. The reduction of the field strength at the interaction volume due to fringe effects can be estimated as follows.

Using the mathematical technique of conjugate functions it can be shown (J41) that for two semi-infinite condenser plates the electric field strength in the symmetry plane of the condenser is,

$$E = (1 + e^{-2\pi x/d})^{-1} E_0, \quad (\text{III.20})$$

where x is pointing into the condenser and the plates begin at $x = d/2\pi$.

In the present experiment, the interaction volume extended from the centre of the plates to about $1.5 d$ from the edge at the narrowest part of the plates. From Eq.III.20 it follows that the electric field in the interaction volume differs by less than 1 part in 10^4 from the field E_0 . Even the combined effect of all edges is probably of the same order and has been neglected.

III.1.7 Detection electronics

The scattered Ly α photons were detected by a PM whose single photon pulses were amplified and counted. The input gates of two scalers were opened and closed in phase with the chopping of the atomic beam. A schematic diagram of the detection system is shown in Fig.III.11.

In the first part of the experiment the EMR photomultiplier was used together with a high speed counting system. The reduction of the background counts by a factor of 10^4 by the O_2 filter and suitable light traps allowed the application of a slower system, less sensitive to pick up. In the second part of the experiment the EMR PM with venetian blind dynodes was

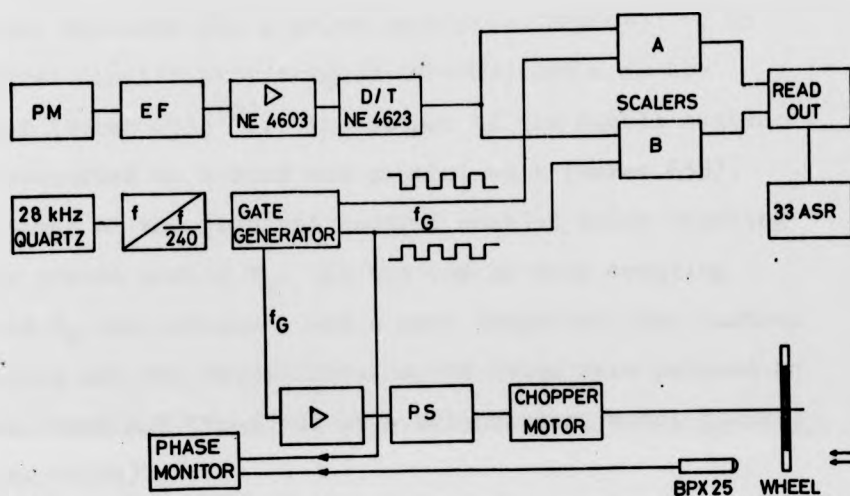


Fig.III.11 Diagram of the detection system, showing the pulse electronics for counting of the photomultiplier pulses, the gating system, and the beam chopper.

replaced by a PM with channeltron electron multiplier (Bendix BX 762) because the channeltron is less affected by stray magnetic fields (BR70, HHKN72, HH73).

As shown in Fig.III.11 the pulse electronics for the level crossing experiments consisted of the PM, an emitter follower EF, a pulse amplifier (NE4603)⁽¹⁾, an integral discriminator/trigger (NE4623) and a double scaler (borer 613)⁽²⁾. The output of the double scaler was connected to a read out control unit (borer 635). The timer of the read out control enabled pulse counting for a preset period T_M . At the end of each counting period T_M the scalers A and B were inhibited from further counting and the experimental count rates were punched on paper tape and typed out by a teleprinter, model 33ASR (borer 497/a).

The scaler input gates were controlled from the gate generator by complementary square wave gating signals at a frequency $f_G = 58.33$ Hz. The gating signals were taken from the Q and \bar{Q} outputs of a flip-flop which was triggered by a signal at frequency $2 f_G$ from a quartz oscillator with subsequent frequency divider. This arrangement ensures correct 1:1 spacing of the square waves within the frequency stability of the oscillator of 10 ppm which is essential for this counting technique. The rise time of the gating signals, τ_r was smaller than 50 ns which is very short compared to the time $T_G = 8.57$ ms each

(1) Nuclear Enterprises, Sighthill, Edinburgh.

(2) borer electronics, Shoreham-by-sea, Sussex.

scaler gate was held open.

The gating electronics were tested by feeding approximately $.1 \cdot 10^5$ pulses per second from a pulse generator into the discriminator and from there to the gated scalers. The difference in the count rates of scaler A, R_A and of scaler B, R_B averaged over several counting periods was, $|R_A - R_B| = (140 \pm 301)/120s$, corresponding to, $|R_A - R_B|/R_A = (2.4 \pm 4.9) \cdot 10^{-5}$. The maximum difference obtained for any one counting period was equivalent to $|R_A - R_B|/R_A = 1.3 \cdot 10^{-4}$, which is small enough to be neglected.

The gate generator provided another output at the same frequency f_G which was fed into a variable phase shifter (PS) and then amplified to drive the chopper synchronous motor. (Globe hysteresis synchronous motor, type 18A107).

The light emitted by the hydrogen furnace was observed by a phototransistor (Mullard BPX25, Si npn) through the chopper wheel producing a photo signal in phase with the chopping of the beam. The phase between the photo signal and one of the gating signals was registered by the phase monitor. This phase showed a small shift with time of about $100 \mu s/4hrs$. The phase also shifted slightly with the magnetic field strength, presumably because of a changing influence of the stray magnetic fields on the chopper motor.

To limit both effects the phase monitor produced a warning signal if the previously adjusted phase between scaler gating and photo signal changed by more than $\pm 50 \mu s$, which is equivalent to $6 \cdot 10^{-3} \pi$.

With this arrangement the following count rates (photons/s) can be observed,

- U the constant dark count rate,
- F the count rate produced by the hydrogen furnace alone,
- L the count rate produced by the lamp alone, and
- S the fluorescence signal count rate.

Assuming that scaler A is open while the atomic beam is on, and scaler B is open while the atomic beam is off, the count rates in scaler A are $(S+F+L+U)$ and $(F+U)$ and the rates in scaler B are $(L+U)$ and (U) depending on whether the lamp is on or not.

To measure a level crossing signal, the counts were collected at different values of the magnetic field for the preset counting period T_M and the count rates were calculated by dividing the number of counts by the time $T_M/2$ the scaler gates were open. The fluorescence rate was then obtained from,

$$S(B) = [(S + L + F + U) - (L + U)] - [(F + U) - U]. \quad (\text{III.21})$$

For maximum fluorescence rate it is desirable that the scaler gating and the chopping of the beam be exactly in phase. In this case the number of counts collected during each gating cycle by scaler A is, $C_A = T_G (S+L+F+U)$, and the number of counts collected by scaler B is, $C_B = T_G(L+U)$, and their difference is,

$$C_A - C_B = T_G (S+F). \quad (\text{III.22})$$

If the beam chopping and scaler gating are out of phase by ΔT , then in each gating cycle the counts collected by scaler A are,

$$C_A' = (T_G - \Delta T) (S + F + L + U) + \Delta T (L + U),$$

and by B are,

$$C'_B = (T_G - \Delta T) (L + U) + \Delta T (S + F + L + U),$$

and their difference is,

$$C'_A - C'_B = T_G (S + F) - 2\Delta T (S + F) = T_G (S + F)' \quad (\text{III.23})$$

If the lamp is off, the equivalent result is,

$$C'_A - C'_B = T_G F - 2\Delta T F,$$

and, therefore

$$T_G S' = T_G S - 2\Delta T S, \quad (\text{III.24})$$

So, if the beam chopping and the scaler gating are not in phase, the calculated signal rate S' is smaller than the true rate S .

A similar reduction is produced if the time τ_R it takes to fully open or close the beam is an appreciable fraction of T_G . This effect was kept small by use of a large chopper wheel with only two teeth producing a ratio of $\tau_R/T_G = 7 \cdot 10^{-2}$.

The calculated rate is also reduced if the time the atomic beam is open, differs from the time it is closed. Both times should be T_G .

To investigate the phase for each gating cycle between one of the gating signals and the photo signal a laser was used as light source instead of the hydrogen furnace and the signals were displayed on an oscilloscope. In addition to the slow shifts mentioned before, this test revealed short term fluctuations of the phase. The main source for this jitter was the imperfect chopper wheel which can cause such fluctuations if the teeth are not identical or not spaced evenly.

Another source of the jitter was the vibration of the long shaft connecting the chopper motor mounted in the MT with the chopper wheel in the recess of the LCT.

The synchronous motor itself contributed to the jitter and also gave rise to phase slipping and sudden large jumps when operated at the specified voltage of 115 v. These irregularities could be reduced considerably by operating at 75 V when the total jitter was reduced to $\pm 25 \mu\text{s}$ which is small compared with $T_G = 8.57 \text{ ms}$. Any remaining irregularities larger than $\pm 50 \mu\text{s}$ were detected by the phase monitor and faulty data were excluded.

III.2 Experimental procedure

The vacuum systems of lamp and hydrogen beam were evacuated to approximately $1 \cdot 10^{-6}$ Torr. The corresponding pressure in the LCT was $2 \cdot 10^{-5}$ Torr because the LCT could only be evacuated through the MT and MPT and the soot covered light traps in the LCT presented a large outgassing surface area.

The araldite seals of the LiF windows in the oxygen filters are prone to develop leaks and were vacuum tested before each experiment. Commercial oxygen, dried in two traps by P_2O_5 and silica gel was admitted through a needle valve to the filters and a continuous flow was maintained.

The electronic system was checked replacing the PM by a fast pulse generator. If no fault was detected the PM was re-connected and its dark count rate of 1 count/10 s was measured.

The furnace was heated while the pressure in the FPT was recorded to ensure smooth heating. If the filaments were new the heating period was 4 hours, if they had been outgassed before the period was 1 hour. Hydrogen gas from the Pd/Ag leak was admitted through a needle valve increasing the pressure in the FPT to $2 \dots 4 \cdot 10^{-4}$ Torr while the pressure in the other tanks was hardly changed. The furnace was then heated up fully and the emission current stabiliser switched in.

Now the count rates (U+F) and (U) were observed and the phase between scaler gating and the photo signal was adjusted to maximum difference between the rates collected in the two scalers. Changes of the adjusted phase were indicated by the phase monitor.

The lamp was filled with He and H_2 mixture and the discharge was run for a cleaning period of 10 min. If the NO chamber showed the presence of instabilities in the $Ly\alpha$ intensity, the gas filling of the lamp was renewed with

slightly different pressure, a different level of microwave power was chosen and the procedure repeated until a reasonably steady $\text{Ly}\alpha$ output was obtained.

A value for the electric field was chosen, the magnetic field was set to a value close to the expected crossing position, and the system was allowed to settle for about 1/2 hr while the rates (U+F) and (U) were counted.

Different procedures were followed from here. Either the electric field was held constant and the magnetic field was changed after each counting period T_M or the magnetic field was held constant and the electric field was varied. The second method had the advantage that the electric field could be changed quickly during the 12 s read out time of the data, while the magnet needed about 40s to stabilise at a new field value. At any combination of the two fields the count rates (S+F+L+U) and (L+U) were measured for periods of 1 or 2 min. For each run the counting was done at 6 to 30 (average 18) values of the variable field covering a range of about 4 FWHM. In most runs the variable field was changed in equidistant steps to transform any time dependence of experimental factors linearly into a field dependence (Sec.IV.2). In some of the runs the steps were increased at the wings to cover a wider field range in the same time.

During each run the $\text{Ly}\alpha$ intensity was monitored by the NO chamber. If the intensity showed strong fluctuations the run was interrupted and the lamp readjusted. At the end of one or two runs the lamp was switched off and its gas mixture renewed while (U+F) and (U) were collected to make sure that they had remained constant.

III.3 Data processing

The crossing positions were determined from the experimental crossing signals by a least squares computer programme using a theoretical "working line shape" to describe the experimental data.

III.3.1 Working line shape

The working line shape can be derived following Sec.III.1.4 by writing the resonance fluorescence count rate in the form,

$$S(E,B) = C f(E,B) N \gamma \int E_\nu \sigma_\nu d\nu, \quad (\text{III.25})$$

where

$f(E,B)$ describes the theoretical level crossing signal whose centre has to be determined,

C contains the geometrical factors which remain constant,

γ accounts for the detection efficiency including PM sensitivity, absorption by the oxygen filter and LiF windows,

N is the number density of the atoms in the interaction volume,

E_ν describes the spectral distribution of the Ly α radiation emitted by the lamp, and

σ_ν is the absorption cross section, $\sigma_\nu = k_\nu / N$, which depends on the frequency because of the distribution of velocities in the atomic beam.

The numerical values of these experimental factors are not essential for the level crossing experiment since no absolute determination of the fluorescence light intensity is required. A change of the experimental factors, however, distorts the level crossing signal and can influence the result of the crossing position (Sec.IV.2.31).

For constant electric field and neglecting the HFS $f(E,B)$ as a function of the magnetic field has Lorentzian form (Sec.II.3). Similarly for constant magnetic field B , it was assumed that the level crossing signal as a function of the electric field can also be approximated by a Lorentzian profile.

In the following the variable field is denoted x while the other field is understood to be constant. Inserting for $f(E,B)$ a Lorentzian profile with centre Z (crossing position), FWHM of $2b$, and amplitude a , the function for the fluorescence count rate can be written,

$$S(x) = C N \int E_{\nu} G_{\nu} d\nu \cdot (1 - a / (1 + (\frac{x-Z}{b})^2)). \quad (\text{III.26})$$

Ideally all experimental factors in Eq.III.26 should be independent of x so that they can be replaced by one constant, say K_0 .

In the experiments the factors were not always exactly constant. As shown in Sec.IV.2.31 it is a good approximation to describe the variation of one or more of the experimental factors by a linear dependence on x which may be written,

$$K = K_0 (1 + d (x-Z)). \quad (\text{III.27})$$

The function $S(x)$ then becomes,

$$S(x) = K_0 + d K_0 (x-Z) - K_0 a (1 + d(x-Z)) / (1 + (\frac{x-Z}{b})^2). \quad (\text{III.28})$$

The main new contribution compared to Eq.II.26 is the sloped background given by the second term of Eq.III.28. This term has been taken into account in the working line shape,

$$S_i(x) = P_3 / (1 + (\frac{x_1 - P_1}{P_2})^2) + P_4 + P_5 (x_1 - P_1), \quad (\text{III.29})$$

which contains 5 constant line shape parameters $P_1 \dots P_5$. The index i is included to stress the fact that the fluorescence count rate S_i was measured at certain values x_i of the variable field.

The dispersion like contribution in Eq.III.28 which has the same position and FWHM as the Lorentzian part leads to a working line shape with 6 parameters, replacing P_3 by $P_3 (1 + P_6 (x_i - P_1))$.

In Sec.IV.2.32 a comparison is reported of the two working line shapes using 5 and 6 parameters. Both were applied to the experimental crossing signals obtained for X1 without electric field. The additional parameter P_6 did not improve the results for the crossing position $P_1 = Z$ which is well known from theory and experiment (BBGM72). Since it is advisable to use as few parameters as possible to fit a small number of experimental points the 5 parameter line shape as given by Eq.III.29 has been applied throughout.

III.3.2 Least squares fit

III.3.21 Computer programme

The subroutine VBO1A⁽¹⁾ was applied to find the best values for the line shape parameters P1...P5 by minimising the sum of squares SQ,

$$SQ = \sum_{i=1}^N \{S_i - f(x_i, P_1 \dots P_5)\}^2 w_i, \quad (\text{III.30})$$

where $f(x_i, P_j)$ is the working line shape, S_i are the fluorescence count rates at the field values x_i , and w_i are their statistical weights (Eq.III.32). Use was made of MAC4A⁽¹⁾ which solves a set of simultaneous linear equations, and of SAO1A⁽¹⁾ which calculates the cumulative χ^2 probability

$$\chi_c^2 = \frac{1}{\Gamma(NF/2)} \int_{\chi_c^2}^{\infty} e^{-\theta} \theta^{(NF/2 - 1)} d\theta, \quad (\text{III.31})$$

where NF is the number of degrees of freedom, $\Gamma(N)$ is the Gamma function, and θ an integration variable.

Further subroutines were DERIV, which contains the working line shape $f(x_i, P_j)$, Eq.III.29 and the derivatives $\partial f / \partial P_j$, where P_j are the line shape parameters P1...P5.

The fitting programme calculated the best values for the line shape parameters P_j , their covariance matrix, the residual sum of squares SQ, the number of

(1) Programme library, Dept. of Physics, Stirling

degrees of freedom NF , the ratio $R = SQ/NF$, and the cumulative χ^2 probability which is the probability of chance occurrence of a ratio R at least as large as that obtained in the fit.

The least squares programme was used in connection with the plotter routine DRAWIK which plots the experimental points, the fitted values, and their difference multiplied by 10. An example is shown in Fig.III.12 where the electric field strength was

29.6 kV/m. The results of the fit were,

$$P1 = Z = (3492.8 \pm 2.3) \text{ G}, \quad P2 = \nu/2 = (34.1 \pm 4.7) \text{ G},$$

$$P3 = -2470. \pm 170. \quad P4 = 18240 \pm 100$$

$$P5 = (-2.47 \pm 0.56) \text{ G}^{-1}, \text{ and}$$

$$SQ = 18, \quad NF = 26, \quad R = 0.69, \quad \chi^2_c = 0.87.$$

From these results the FWHM and the amplitude $D = P3/P4$ of the crossing signal were calculated to be,

$$b = (68.3 \pm 9.3) \text{ G} \text{ and } D = (-13.55 \pm 0.89)\%.$$

III.3.22 Goodness of fit

The statistical weights of the count rates were set as,

$$w_1 = 1/((S+L+F+U) + (L+U) + (F+U)), \quad (\text{III.32})$$

taking into account the statistical variances of all count rates which were used in Eq.III.21 to calculate the fluorescence count rate S_1 .

If the statistical weights are chosen correctly the residual sum of squares SQ is expected to have a χ^2 distribution appropriate for the number of degrees of freedom, NF . In this work the number of points in each

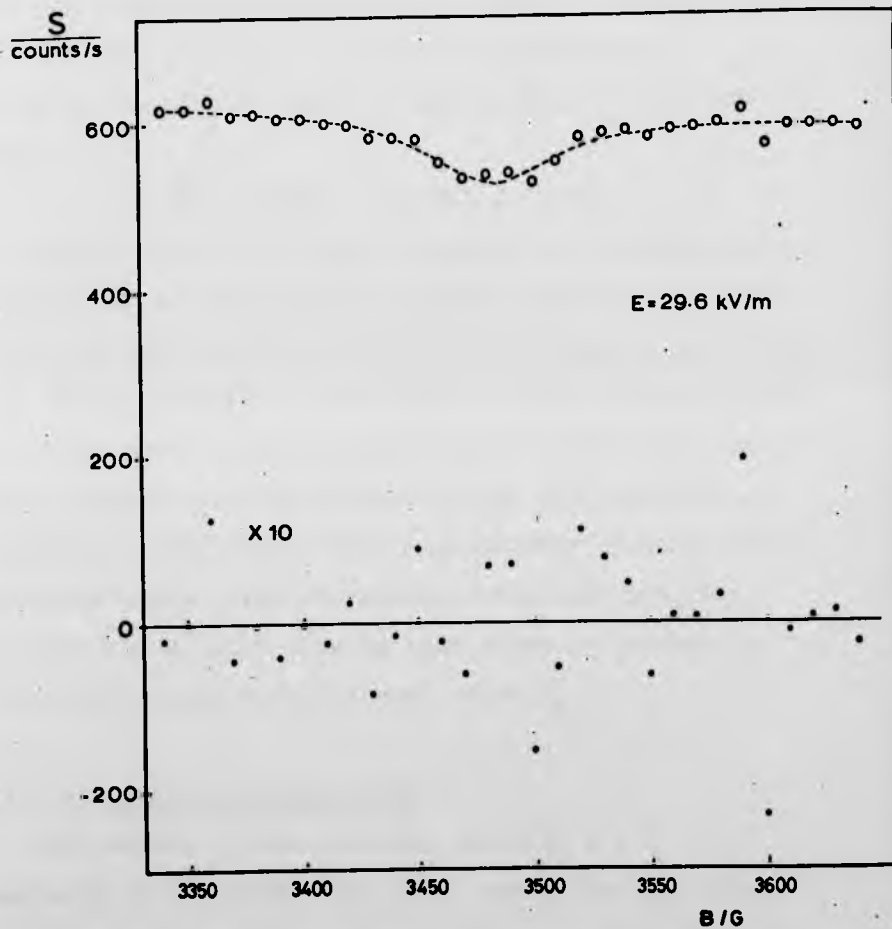


Fig.III.12 Experimental level crossing signal for $E = 29.6$ kV/m (open circles), least squares fit (dashed line), and their difference multiplied by 10 (dots). Crossing X1, experiment LC4, run E19.

crossing signal varies between 6 and 30 and no value of NF has enough crossing signals to allow a test of the distribution. The ratio $R = SQ/NF$, on the other hand should have a distribution, admittedly different for different values of NF, about the value 1 for all NF. The distribution $f(R)$ of R for all experimental crossing signals is shown in Fig.III.13. The expectation value,

$$\sum R \cdot f(R) / \sum f(R) = 1.18 ,$$

is close to 1 and $f(R)$ shows an asymmetry characteristic of the χ^2 distributions for low NF. The mean value for χ^2_c is 0.4 which differs little from the ideal case of 0.5.

It is, therefore, concluded that the measured rates S_i of the level crossing signals used in the data analysis have a scatter correctly described by the statistical weights w_i . This means that no important distortions of the experimental crossing signals remained unobserved, and that the assumed working line shape is reasonable within the scatter of the count rates S_i .

III.3.23 Average and rms error

The values of the crossing position $Z = P1$, and similarly of the FWHM, $b = 2 \cdot P2$, and of the amplitude $D = P3/P4$ obtained from different crossing signals for the same value of the constant field were averaged according to their statistical weights,

$$\bar{Z} = \frac{\sum_{j=1}^N \epsilon_j Z_j}{\sum_{j=1}^N \epsilon_j} ; \quad \epsilon_j = \frac{1}{6_j^2} \quad (III.33)$$

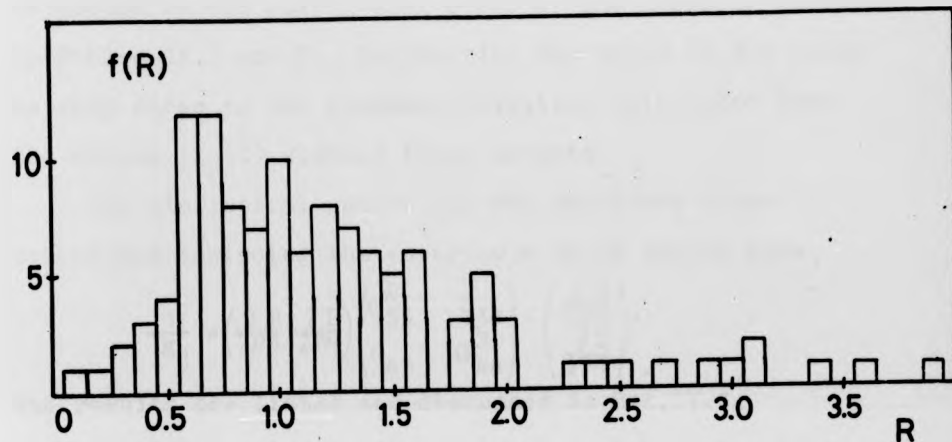


Fig.III.13 Distribution of values for the ratio R of the sum of squares SQ and the number of degrees of freedom NF , for all experimental runs, showing the characteristic asymmetry of a χ^2 distribution for low NF .

where σ_j^2 is the variance of Z_j calculated by the fitting programme. The rms error defined by,

$$(\Delta Z)^2 = \sum_{j=1}^N \sigma_j (Z_j - \bar{Z})^2 / \sum_{j=1}^N \sigma_j \quad , \quad (\text{III.34})$$

is quoted as the statistical error of the crossing position in Tables IV.1 and 3. In practice the value of ΔZ would be very close to the standard deviation calculated from the values $(Z_j - \bar{Z})$ without their weights.

The statistical weight for the amplitude D was calculated including the covariance of P3 and P4 from,

$$\frac{1}{\sigma_j} = \begin{pmatrix} \frac{\partial D}{\partial P3} & \frac{\partial D}{\partial P4} \end{pmatrix} \begin{pmatrix} \sigma_{33}^2 & c_{34} \\ c_{43} & \sigma_{44}^2 \end{pmatrix} \begin{pmatrix} \frac{\partial D}{\partial P3} \\ \frac{\partial D}{\partial P4} \end{pmatrix} .$$

The results are listed and discussed in Sec.IV.1.

III.3.3 Normalisation to Ly α intensity

It was originally planned to normalise the experimental count rates to equal Ly α intensity as monitored by the NO ionisation chamber.

The normalisation was tested for the signals of crossing X1 without electric field, the position of which should be 3484.1 G. The results obtained from the computer fit for the crossing position when using the normalised count rates did not agree better with the theoretical value than the results from the original data. Moreover, it became obvious that the normalisation did not improve the line shape of the crossing signals but in some cases introduced distortions worse than those present in the original crossing signal.

The failure of the Ly α monitor can be explained when it is realised that fluctuations of the Ly α intensity were usually accompanied by changes of the discharge mode of the lamp, which in turn changed the profile of the emitted Ly α line. It is possible that the Ly α intensity integrated over the range of frequencies absorbed by the atoms is affected differently by a change of the discharge mode from the Ly α intensity integrated over all emitted frequencies as measured by the NO chamber.

The NO chamber has nevertheless been useful in ensuring that only runs with reasonably stable Ly α intensity were included for the data analysis.

CHAPTER IV

The experimental results for the crossings X1 and X2 are described in the first section of this chapter. In Sec.IV.2 the experimental errors are considered. Finally, the experimental results are discussed in comparison with theoretical calculations carried out assuming different values for the Lamb shift and for the Stark effect matrix elements.

IV.1 Experimental results

IV.1.1 Crossing X1

The results obtained for the crossing position, for the FWHM, and for the amplitude of crossing X1 as a function of the electric field are reported in the next two sections.

IV.1.11 Crossing position

A list of measurements taken for crossing X1 is given in Table IV.1. The first column gives an identification of the experiment, the second column the number of crossing signals recorded for the particular value of the constant external field.

In most cases the electric field was held constant and the resonance fluorescence count rate was observed as a function of the magnetic field. The experimental magnetic field crossing position determined as described in Sec.III.3.2 is given in column 4 together with the statistical error defined in Eq.III.34.

Exp	No of runs	E/kVm ⁻¹	B/G	ΔE/kVm ⁻¹	ΔB/G
LC4	6	0	3483.9±3.1	-	
MR5	4	0	3480.3±5.7	-	12
LC1	3	0	3485.1±2.1	-	
LC2	3	12.18	3480.13±0.53	0.30	16
LC4	2	19.68	3490.6±2.1	0.17	12
LC2	1	24.35	3489.2±3.3	0.61	16
LC4	4	29.52	3498.2±2.0	0.26	12
LC2	1	36.53	3502.3±1.1	0.92	16
MR5	1	46.2	3523.9±1.7	3.5	16
LC4	6	49.20	3523.79±0.62	0.43	12
LC2	5	49.9±1.3	3530.0	1.3	16
MR5	1	73.9	3593.2±2.6	5.6	16
LC4	5	78.73	3589.5±2.0	0.69	12
MR5	4	74.0±2.1	3600.0	5.6	16
MR5	2	92.4	3649.1±3.4	7.0	16
LC1	5	117.9±2.6	3750.0	2.5	16
LC4	6	123.3	3746.2±2.3	1.2	+16-12
MR5	1	139.0	3857.6±7.0	11.0	16
LC1	3	164.82±0.96	4000.0	3.5	16
LC4	10	182.60±0.66	4050.0	1.8	+12-16
LC2	8	190.43±0.91	4120.0	5.1	16
LC4	5	222.69±0.62	4300.0	2.2	+12-15
LC1	1	210.9± 3.7	4300.0	4.5	16
LC4	7	252.2± 1.1	4500.0	2.5	+12-16

Table IV.1 List of measurement of crossing X1.

The first two columns give the identification of the experiment and the number of level crossing signals used to derive the result for the crossing position. E is the electric field strength and B the magnetic field strength at the crossing. Either E or B was held constant during each run and the result for the other is quoted with its rms error. ΔE and ΔB are the experimental errors discussed in Sec. IV.2.

In some cases the magnetic field was held constant and the resonance fluorescence light observed as a function of the electric field strength. In these cases column 4 gives the constant magnetic field and column 3 gives the electric field at the crossing position with its statistical error.

The next column ΔE states the uncertainty of the electric field strength calculated according to Sec.IV.2.21. The last column $\Delta B = \Delta B_1 + \Delta B_2 + \Delta B_3$ shows the sum of the systematic error of the magnetic field measurement, ΔB_1 (Sec.IV.2.1) and the errors in the determination of the crossing position, $\Delta B_2 + \Delta B_3$ (Sec.IV.2.22 and IV.2.3).

The crossing position for zero electric field was determined in the three experiments MR5, IC1 and IC4. The weighted mean of the values for the crossing position listed in the first three rows of Table IV.1 with its statistical error is,

$$B(E = 0) = (3484.3 \pm 1.3)G.$$

This experimental result obtained from 13 runs agrees very well with the theoretical value of,

$$B(\text{theor.}) = 3484.1 G.$$

The agreement is much better than to be expected from the systematic error of $\Delta B = \pm 12 G$ given in Table IV.1. This value of ΔB was estimated (Sec.IV.2) for a single level crossing signal. Some of the effects contributing to ΔB cancel when the results for the crossing position obtained from a number of crossing signals of the same constant field are averaged.

Therefore, the systematic error should fully be taken into account when only one crossing signal is available but can be regarded as a conservative estimate if several runs were used to derive the experimental result.

The information contained in Table IV.1 is displayed in Fig.IV.1. The dashed line indicates the theoretical relation between the electric field E and the magnetic field B at the crossing, taking the average of the two HFS crossings.

As can be seen from Fig.IV.1 the agreement between the theoretical curve and the experimental points is good. The accuracy of the measurements and, therefore the error bars in Fig.IV.1 differ mainly because of different uncertainties in the values of the electric field strength (Table IV.4) resulting from the measurement of the condenser gap. The uncertainty is smallest in experiment LC4 where it is of order 1%. However, assessing the results of LC4 it must be taken into account that some of the experimental tests, e.g. reversing the polarity of the condenser plates, which were found not to have a significant effect on the results within an accuracy of 2% in the experiments LC1 and LC2 have not been repeated for LC4 because of lack of time. Therefore, systematic errors within the accuracy of 2% cannot be excluded in any of the measurements.

For some of the experimental runs where the electric field was varied one least squares fit was obtained using the electric field values as variable field x and the results are listed in Table IV.1. Another fit was

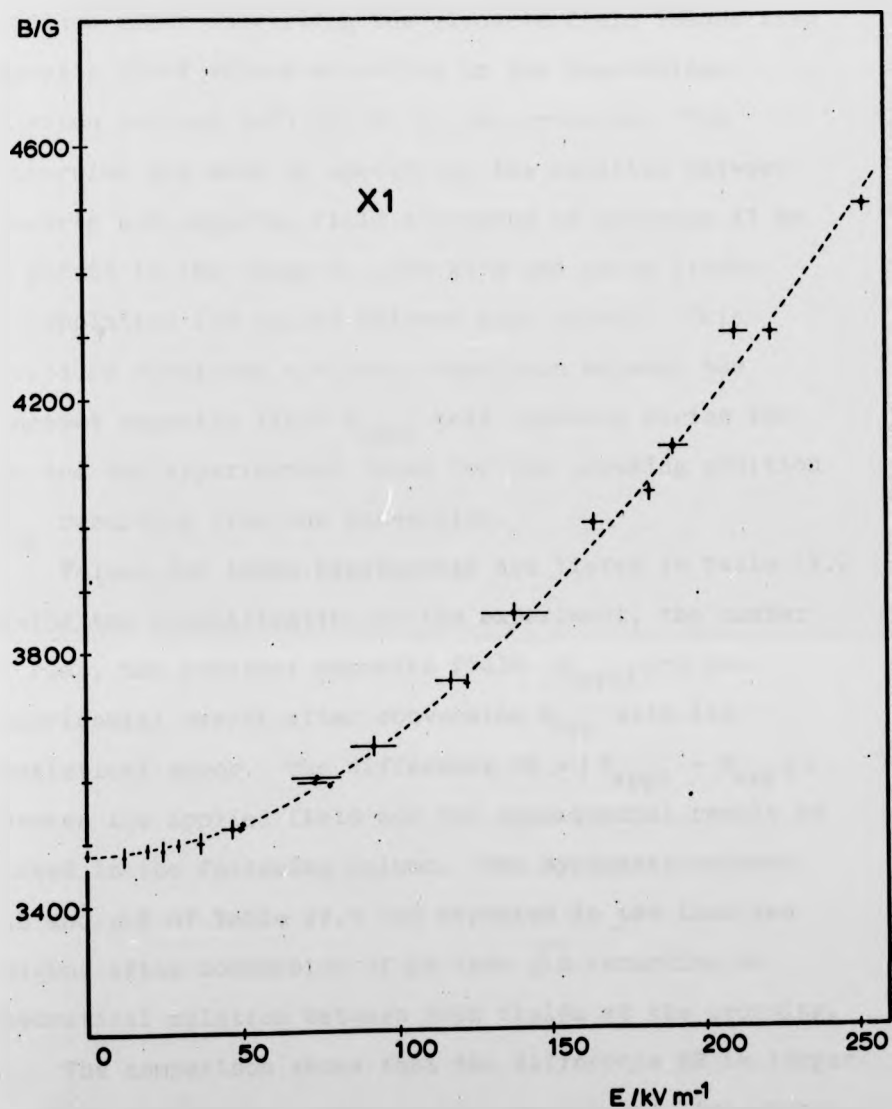


Fig.IV.1 Experimental results and theoretical values for crossing X1 showing the magnetic field strength B and the electric field strength E at the crossing for the low-field range of the Stark effect. The line indicates the mean value of the two HFS crossings obtained from the diagonalisation of the combined Stark and Zeeman perturbation matrices. The experimental results of Table IV.1 are shown with error bars including the statistical errors and the systematic errors ΔB and ΔE . The error bars for ΔB have had to be omitted for the close lying points at 50 kV/m and 80 kV/m.

obtained after converting the electric field values into magnetic field values according to the theoretical relation between both fields at the crossing. The conversion was made by specifying the relation between electric and magnetic field strengths at crossing X1 by 50 points in the range 0...250 kV/m and using linear interpolation for values between such points. This procedure furnishes a direct comparison between the constant magnetic field B_{appl} held constant during the run and the experimental value for the crossing position B_{exp} resulting from the conversion.

Values for three experiments are listed in Table IV.2 giving the identification of the experiment, the number of runs, the constant magnetic field B_{appl} , and the experimental result after conversion B_{exp} with its statistical error. The difference, $DB = |B_{\text{appl}} - B_{\text{exp}}|$, between the applied field and the experimental result is listed in the following column. The systematic errors ΔE and ΔB of Table IV.1 are repeated in the last two columns after conversion of ΔE into $\overline{\Delta B}$ according to theoretical relation between both fields at the crossing.

The comparison shows that the difference DB is larger than the statistical error of the results but lies within the systematic errors ΔB and $\overline{\Delta B}$.

Experiment	number of runs	B_{appl}	B_{exp}	DB	ΔB	$\overline{\Delta B}$
MR5	4	3600	3587.6 ± 5.8	12.4	16	20
IC4	10	4050	4066.9 ± 3.9	16.9	$\begin{matrix} +12 \\ -16 \end{matrix}$	10
IC4	7	4500	4520.8 ± 7.4	20.8	$\begin{matrix} +12 \\ -16 \end{matrix}$	15

Table IV.2 Comparison of the magnetic field B_{appl} held constant during the runs with the magnetic field value obtained as crossing position B_{exp} from the least squares fit when the values of the electric field were converted according to the theoretical relation into magnetic field values.

IV.1.12 Width and amplitude of crossing signal X1

In Fig.IV.2 and Fig.IV.3 the values for the FWHM and the amplitude D of the crossing signal X1 are shown as a function of the electric field strength.

The solid line in Fig.IV.2 represents the FWHM one would expect from Eq.II.56, page 58, due to the changing relative slope $\partial B/\partial W_{b,b}$ of the crossing states for a natural width of 100 MHz. The additional decrease of the FWHM for higher electric fields may be due to the admixture of S character to the originally pure P state which extends the lifetime and reduces the natural width of the state at the crossing. (1)

(1) The reduction of the lifetime due to field ionisation has been shown to be negligible by Lüders (L51).

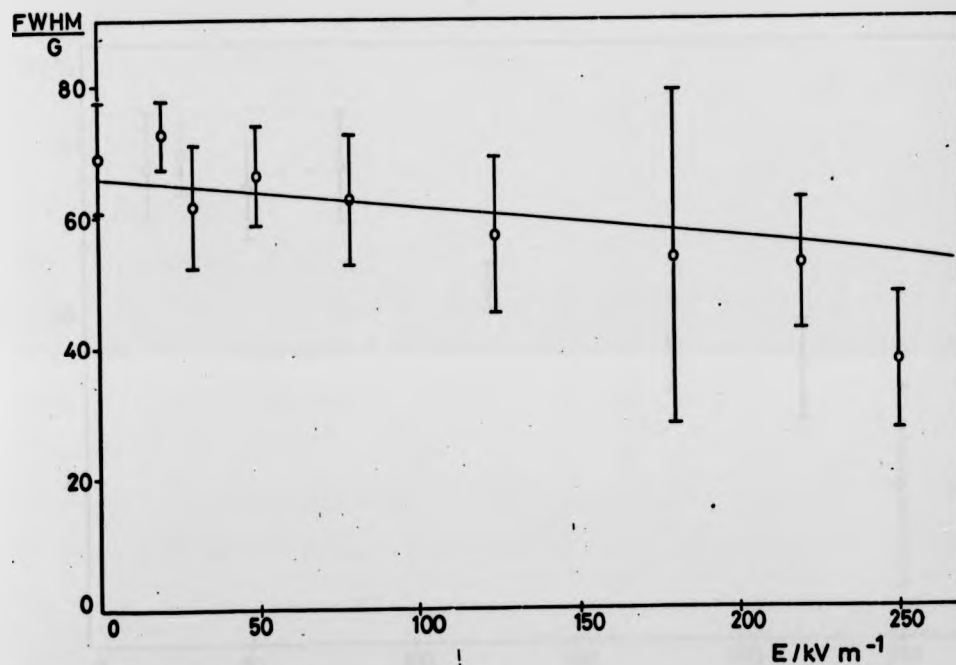


Fig.IV.2 FWHM of crossing X1 as a function of the electric field strength. The line indicates the FWHM calculated according to Eq.II.56 for a natural width of 100 MHz of the crossing states.

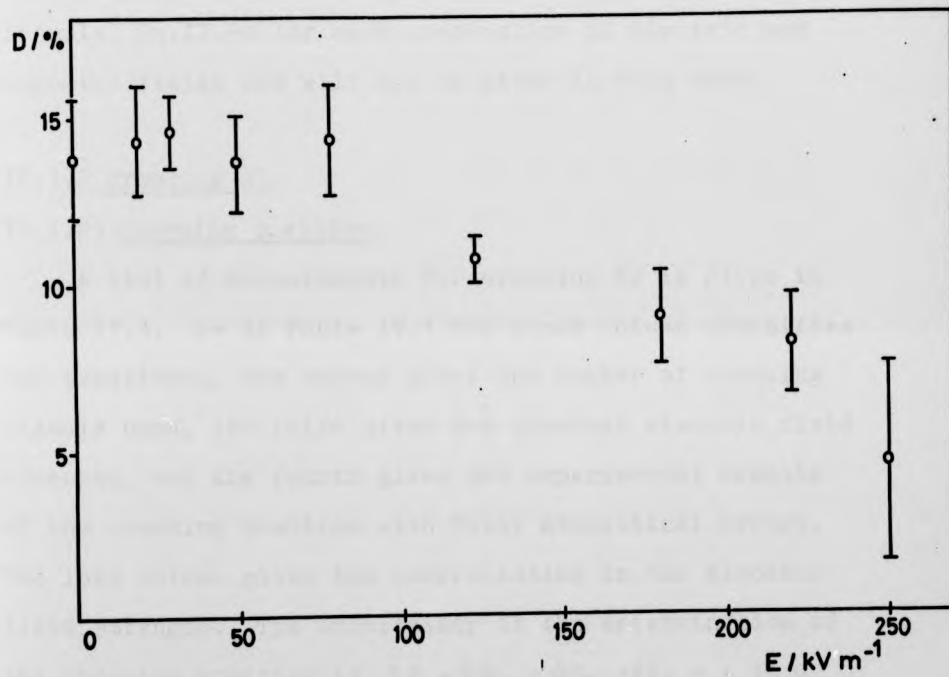


Fig.IV.3 Amplitude D of crossing X1 as a function of the electric field strength.

Similarly the decrease of the amplitude D of the crossing signal which depends on the P content of the crossing states can be explained by the admixture of S character to the $P_{1/2}$ states at the crossing ⁽¹⁾.

A quantitative analysis of the FWHM and the amplitude would involve the application of the Breit formula, Eq.II.54 for each combination of electric and magnetic fields and will not be given in this work.

IV.1.2 Crossing X2

IV.1.21 Crossing position

A list of measurements for crossing X2 is given in Table IV.3. As in Table IV.1 the first column identifies the experiment, the second gives the number of crossing signals used, the third gives the constant electric field strength, and the fourth gives the experimental results of the crossing position with their statistical errors. The last column gives the uncertainties in the electric field strength. The uncertainty in the determination of the crossing position is $\Delta B = \Delta B_1 + \Delta B_2 + \Delta B_3 = \pm 16$ G for all points (Sec.IV.2).

The results are displayed in Fig.IV.4. The theoretical values, the mean values of the two calculated HFS crossings, are indicated by the solid line which has the same shape

(1) The change of the amplitude caused by the formation of anticrossings was estimated to be negligible (Sec.II.3).

Exp	No of runs	E/kVm ⁻¹	B/G	ΔE/kVm ⁻¹
LC3	2	48.68	2357. <u>+</u> 20. est	1.23
LC3	1	60.88	2374.9 <u>+</u> 5.9	1.53
LC3	1	73.02	2405.5 <u>+</u> 9.1	1.84
LC3	2	97.40	2410.05 <u>+</u> 0.36	2.45
LC4	2	98.41	2422.6 <u>+</u> 4.1	0.86
LC3	2	121.95	2437.87 <u>+</u> 0.76	3.23
LC4	4	138.1	2450.3 <u>+</u> 1.6	1.4
LC3	1	183.0	2500.4 <u>+</u> 2.3	4.85
LC3	3	195.1	2502.3 <u>+</u> 3.2	5.17
LC3	1	292.7	2548.5 <u>+</u> 1.9	7.76
LC3	1	390.2	2570.2 <u>+</u> 2.4	10.3
LC3	1	487.8	2581.7 <u>+</u> 1.8	12.9

Table IV.3 List of measurements of crossing X2. The first two columns identify the experiment and state the number of level crossing signals used to determine the result for the crossing position. E is the constant electric field strength and B is the experimental result for the magnetic field strength at the crossing position with its rms error. ΔE is the experimental error in the determination of the electric field strength.

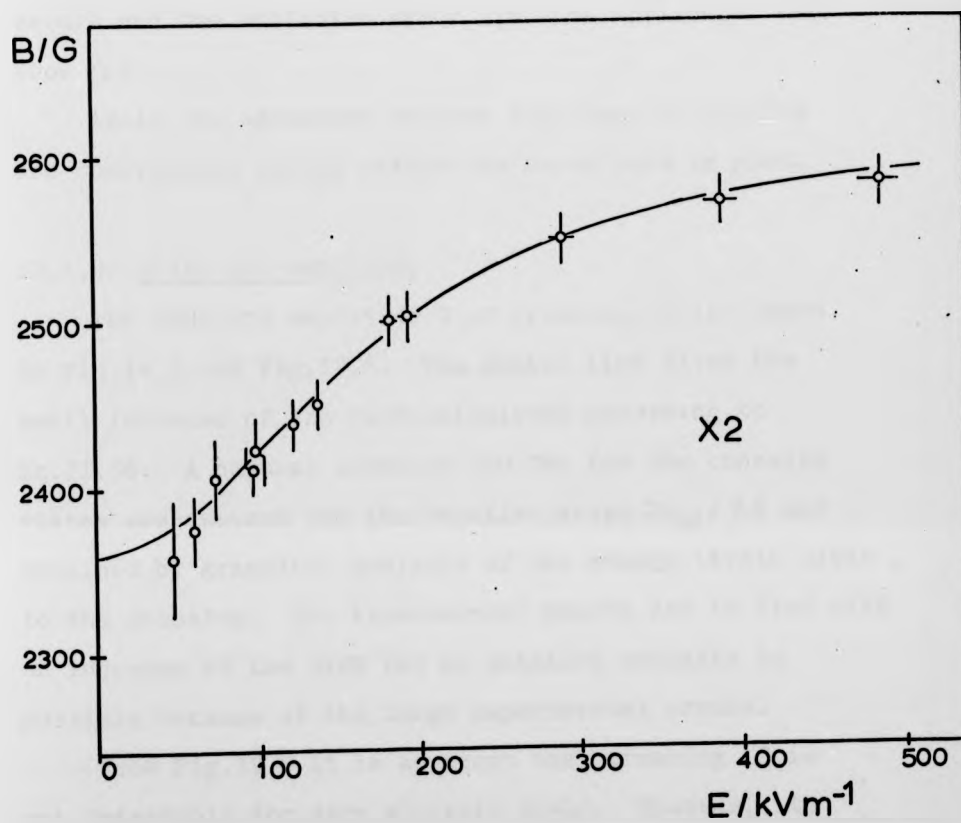


Fig. IV.4 Experimental results and theoretical values for crossing X2 showing the magnetic field strength B and the electric field strength E at the crossing. The solid line indicates the theory showing the mean value of the two observable HFS crossings. The open circles are the experimental results. The error bars include statistical and systematic errors as listed in Table IV.3.

as branch C in Fig.I.1. The circles are the experimental results. The vertical error bars show the statistical errors and the estimated error ΔB , the horizontal bars show ΔE .

Again the agreement between experimental results and theoretical values within the error bars is good.

IV.1.22 Width and amplitude

The FWHM and amplitude D of crossing X2 are shown in Fig.IV.5 and Fig.IV.6. The dashed line gives the small increase of the FWHM calculated according to Eq.II.56. A natural width of 100 MHz for the crossing states was assumed and the relative slope $\partial w_{bb} / \partial B$ was obtained by graphical analysis of the energy levels close to the crossing. The experimental points are in line with an increase of the FWHM but no detailed analysis is possible because of the large experimental errors.

From Fig.IV.6 it is apparent that crossing X2 is not detectable for zero electric field. However, its amplitude rises steeply with the electric field which produces the P admixture to the originally pure S states at the crossing.

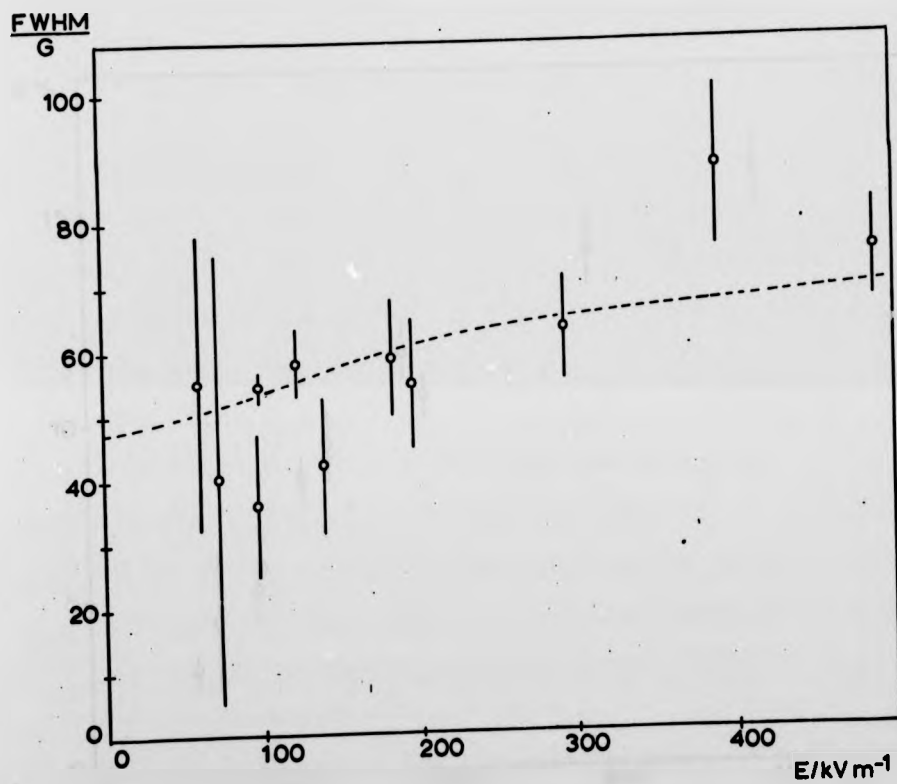


Fig.IV.5 FWHM of crossing X2 as a function of the electric field strength. The line indicates the FWHM calculated according to Eq.II.56 for a natural width of 100 MHz of the crossing states.

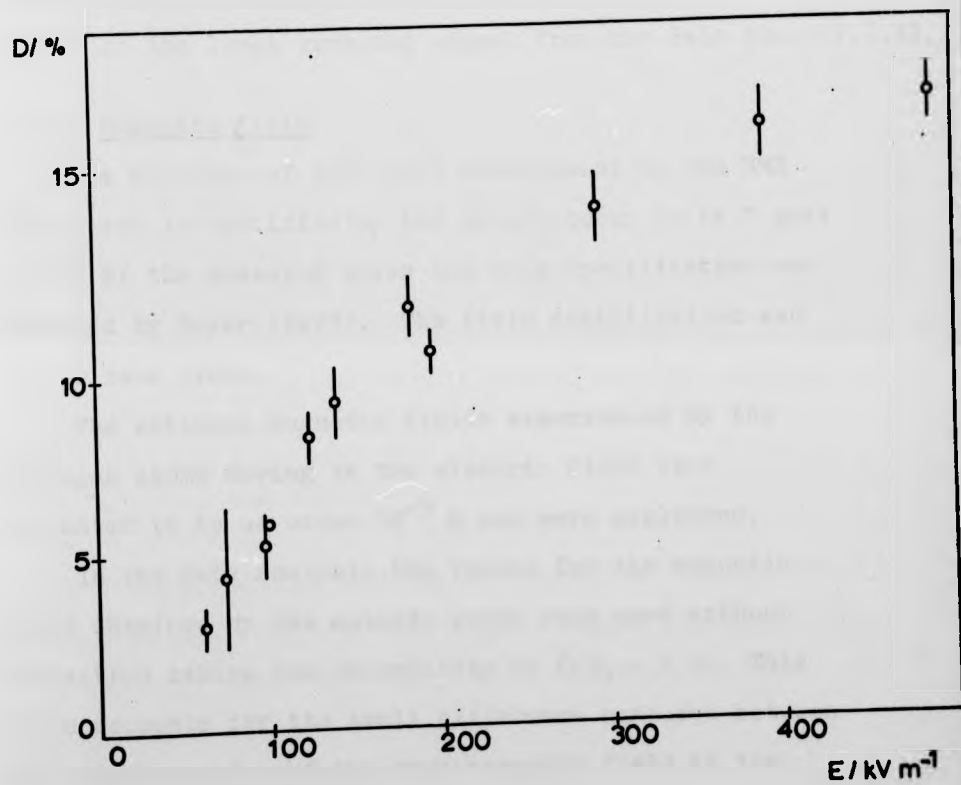


Fig.IV.6 Amplitude of crossing X2 as a function of the electric field strength.

IV.2 Error discussion

The measurement of the relation between the electric field E and the magnetic field B at the crossing has three sources of error. These are the measurement of the magnetic field strength (Sec.IV.2.1), the measurement of the electric field strength (Sec.IV.2.2), and the determination of the centre of the level crossing signal from the data (Sec.IV.2.3).

IV.2.1 Magnetic field

The accuracy of the field measurement by the NMR gaussmeter is specified by the manufacturer to be 1 part in 10^5 of the measured value and this specification was verified by Beyer (Be73). The field stabilisation was of the same order.

The motional magnetic fields experienced by the hydrogen atoms moving in the electric field were estimated to be of order 10^{-5} G and were neglected.

In the data analysis the values for the magnetic field obtained by the outside probe were used without correction taking the uncertainty as $\Delta B_1 = 1$ G. This value accounts for the small difference measured between the outside probe and the true magnetic field at the interaction volume (Sec.III.1.53), and for the inhomogeneity of the magnetic field across the interaction volume (Sec.III.1.52).

IV.2.2 Electric field

IV.2.21 Electric field parallel to the magnetic field

The electric field strength has been calculated from $E = U/d$, neglecting fringe field effects which should be smaller than 1 part in 10^4 . The voltage U was stabilised at $\Delta U/U = 5 \cdot 10^{-5}/\text{hr}$.

In different experiments different sets of condenser plates were used and the uncertainty of the electric field strength depends mainly on the error in the measurement of the respective condenser gap. The resulting uncertainty in the electric field strength including that of the applied voltage is listed in Table IV.4.

Experiment	Uncertainty
MR5	7.7%
LC1	2.2%
LC2,3	2.7%
LC4	1.0%

Table IV.4 Uncertainties in the electric field strength for different experiments calculated from the errors of the condenser gap and of the applied voltage.

For values of the applied voltage below 1100 V which had been measured with a DVM slightly smaller uncertainties apply (Sec. III.1.6). The corresponding values for the error in the electric field strength, ΔE are stated in Tables IV.1 and IV.3, column 5.

An error in the electric field strength being applied parallel to the magnetic field can also come from a misalignment of the two fields. A misalignment by an angle α splits the applied electric field E into one component parallel to the magnetic field, $E_z = E \cos \alpha$, and another component perpendicular to the magnetic field, $E_{al} = E \sin \alpha$.

It can be assumed that the visual alignment of the condenser plates relative to the pole faces was correct

within an angle $\alpha = 2^\circ$, so that $\cos 2^\circ = 0.9994$ and $\sin 2^\circ = 0.0349$. The difference between E and E_z of 6 parts in 10^4 is well within the other uncertainties and need not be taken into account. The component E_{al} together with the motional electric field can affect the level crossing position and this possible error is estimated in Sec.IV.2.22.

Another systematic error in the electric field strength can be introduced by deformations of the electric field caused by the close proximity of the aluminium walls of the vacuum tank. Since one of the condenser plates was held at high voltage while the other was on ground potential, this disturbance would cause an asymmetry which could be tested experimentally by reversing the voltage connections to the two condenser plates. This test was found to have no effect on the crossing position within the accuracy of experiments LC1 and LC2 but it has not been repeated to the accuracy of 1% which would be desirable for experiment LC4.

IV.2.22 Electric field perpendicular to the magnetic field

Electric field components in the x-y plane can be generated by misalignment between electric and magnetic fields, and by the motion of the hydrogen atoms in the magnetic field.

The component due to misalignment, E_{al} is a constant fraction of the applied electric field, $E = U/d$, for all runs of the same experiment. In the x-y plane it can point in any direction relative to the motional field, E_{mot} . The motional field of the order of 3 kV/m is at

right angles to the atomic beam direction and is proportional to the magnetic field strength. The spread of E_{mot} resulting from the distribution of velocities and the variation of E_{mot} over the crossing width are neglected.

The total electric field perpendicular to the magnetic field,

$$\vec{E}_{\perp} = \vec{E}_{\text{mot}} + \vec{E}_{\text{al}} ,$$

is assumed to point in the x-direction to obtain a real perturbation matrix.

Values of the applied electric field E close to those used in experiment LC4 and the corresponding theoretical magnetic field crossing positions B are listed in Table IV.5. Also listed are the magnitudes of $E_{\text{al}} = E \sin 2^{\circ}$, and $E_{\text{mot}} = \bar{v}_B B$ and their sum $E_{\text{max}} = E_{\text{al}} + E_{\text{mot}}$. E_{max} is the maximum size for the electric field perpendicular to the magnetic field obtained when \vec{E}_{mot} and \vec{E}_{al} point in the same direction.

The crossing position B' is then determined, for the electric field given by the vector $\vec{E} = (E_{\text{max}}, 0, E)$, by graphical analysis of the energy levels near the anti-crossing (Sec. II.2.3, Fig. II.8) and is listed in the next column of Table IV.5. The uncertainty of the graphical analysis was estimated to be ± 0.5 G.

The difference $\Delta B_2 = B - B'$ has been incorporated in the uncertainty ΔB quoted in Table IV.1 for LC4. To account for this possible error in the experiments MR5, LC1,2,3 as well, the maximum deviation of $\Delta B_2 = 5$ G has been used to obtain the values of ΔB stated in Table IV.1 and Table IV.3.

E	B	E_{al}	E_{mot}	E_{max}	B'	ΔB_2
0	3484.1	0	2.86	2.86	3484.3	-0.2
19.7	3491.3	.69	2.85	3.55	3491.5	-0.2
29.6	3500.3	1.03	2.87	3.80	3500.8	-0.5
49.3	3529.1	1.72	2.89	4.61	3529.2	-0.1
78.9	3598.7	2.75	2.95	5.70	3598.2	0.5
123.3	3759.6	4.30	3.08	7.40	3754.7	4.9
180.0	4051.5	6.28	3.32	9.60	4056.0	-4.5
220.0	4300.5	7.68	3.52	11.20	4304.3	-3.8
250.0	4504.9	8.73	3.69	12.40	4508.9	-4.0

Table IV.5 Effect of E_{\perp} on the position of crossing X1.

E is the electric field strength close to that applied in Exp. IC4.

B is the corresponding magnetic field at crossing X1.

E_{al} is the electric field component perpendicular to the magnetic field caused by possible misalignment of applied electric and magnetic fields.

E_{mot} is the motional electric field.

E_{max} is the maximum electric field strength perpendicular to the magnetic field when

\vec{E}_{al} and \vec{E}_{mot} are pointing in the same direction.

B' is the position of the anticrossing obtained by graphical analysis of the energy levels with an estimated uncertainty of ± 0.5 G.

$$\Delta B_2 = B - B'$$

The values of the electric fields are quoted in kV/m, the values of the magnetic fields in G.

In the case of perfect alignment only the motional electric field would remain. Its effect on the crossing position can be estimated to be smaller than 1 G assuming a quadratic dependence of the shift on E_{\perp} .

IV.2.3 Data analysis and signal distortions

The determination of the crossing position can be in error if the working line shape used in the least squares programme does not account properly for the distortions of the Lorentzian line profile in the experiment.

In the following section the influence of the experimental factors (Eq.III.26) on the measured crossing signal is investigated. It is shown that the variation of the experimental factors is so small or so slow that it can be approximated by a linear dependence on the variable field x which is already included in the working line shape. An exception is the nonlinear variation of the L_{yx} intensity and in Sec.IV.2.32 the effect of a nonlinear dependence on x is considered using computer simulations instead of experimental crossing signals as input data for the least squares fit. The error introduced by only partly accounting for linear variations when using the 5 parameter working line shape instead of the 6 parameter line shape, is estimated in the same way.

IV.2.31 Variation of experimental factors

In this section the variation of the experimental factors determining the fluorescence count rate as described in connection with Eq.III.26 is estimated.

IV.2.311 Detection efficiency

Changes in the detection efficiency η can be produced in three ways.

(a) Magnetic field defocussing effects in the multiplier can alter the PM sensitivity. The PM was screened by a soft iron cylinder to reduce the stray magnetic field to

4 G for $B_0 = 3500$ G in the centre of the magnet. Since magnetic fields as small as 4G hardly affect the PM output (Sec.III.1.7) variations of B_0 should result in only very small changes of the PM sensitivity.

(b) The phase between gating signals and beam chopping can change spontaneously with time or as a result of the magnetic field disturbing the synchronous motor. The phase monitor warned of any phase changes larger than $\pm 50 \mu s$. According to Eq.III.24 a phase change by $\Delta T = \pm 50 \mu s$ alters the experimental rate S' by $\pm 1\%$. Slow phase changes of this order can well be approximated by a linear dependence on x .

Quick changes of the order of 1% and the jitter (Sec.III.1.7) between gating and beam chopping introduce an error of the experimental rate S_i which is, however, distributed randomly. Such jitter only increased the scatter of the experimental count rates S_i and, therefore the statistical error of the crossing position.

(c) The $Ly\alpha$ absorption by the O_2 filter and the LiF windows can change with time. Since a steady flow of dried oxygen, controlled by a needle valve was maintained during the experiments, very small and slow changes are expected. Larger changes in the O_2 absorption would have shown up in the NO chamber current since the oxygen flow was common to the two filters in front of the PM and in front of the NO chamber.

IV.2.312 Hydrogen density

The parameters determining the density of the hydrogen beam were the temperature of the tungsten pipe and the total throughput of hydrogen (Sec.III.1.25).

Since the current of electrons bombarding the tungsten pipe was stabilised and because of the high thermal capacity of the hydrogen furnace, only slow drifts of the temperature were expected.

The variations of the hydrogen throughput were observed by measuring the pressure in the furnace pump tank. The pressure was found to vary by less than $1 \cdot 10^{-5}$ Torr/hr so that changes of the density during a run of about 20 min are of order 3%.

IV.2.313 Ly α emission

The lamp influenced the measurement through

- (a) the time dependence of the Ly α intensity,
- (b) the magnetic field dependence of the Ly α intensity, and
- (c) the non-uniform spectral distribution.

The time dependence may occur as short term instabilities or long term drifts.

The short term instabilities, where the Ly α intensity changes by a few per cent within less than a second, contribute to the scatter of the count rates S_1 . As no trend could be found in the occurrence of such jumps it was assumed that they follow a random distribution, so that they only increased the statistical error of the crossing position.

The long term intensity drifts, in most cases, took the form of slow decrease of intensity. By choosing equal steps between the values of the variable field x , the time dependence was transformed linearly into an x dependence. An attempt was made to obtain pairs of crossing signals, one with increasing field x and one with decreasing field, to eliminate the effect of such drifts on the crossing position. However, the $\text{Ly}\alpha$ intensity sometimes decreased more steeply at the beginning of a run than at the end, or could slowly rise to a maximum and then drop again. These variations were smaller than 10% of the total intensity over a run and the error introduced by such nonlinear variations is estimated in the next section.

(b) As may be seen from Fig.III.8, the dependence of the $\text{Ly}\alpha$ intensity on the magnetic field can be approximated by a straight line over the width of a crossing signal.

(c) Changes in the spectral distribution of the $\text{Ly}\alpha$ line without variation of the intensity integrated over all emission frequencies could not have been detected in the experiment. However, from the goodness of fit it can be concluded that they were small.

The centre frequency of the band absorbed by the atoms out of the $\text{Ly}\alpha$ line profile is changed when the external field shifts the energy levels of the atoms. Such changes are of order 10^9 Hz over the width of a crossing signal, and the $\text{Ly}\alpha$ profile of width of 10^{11} Hz (Fig.III.10) can well be approximated by a straight line for this small interval.

IV.2.32 Computer simulations

Sets of data (x_i, y_i) simulating the crossing signals were calculated and treated by the same fitting procedure as the experimental data (x_i, S_i) to estimate the errors introduced by the least squares programme and by not accounting fully for the distortions of the signal in the experiments when using the 5 parameter working line shape.

The data sets were calculated from,

$$\begin{aligned} \text{(a)} \quad y_i^{(a)} &= A / (1 + (\frac{x_i - Z}{b})^2) + e, \\ \text{(b)} \quad y_i^{(b)} &= y_i^{(a)} (1 - d(x_i - Z)), \\ \text{(c)} \quad y_i^{(c)} &= y_i^{(a)} (YMIN + YE (x_i - XMIN)^2) \end{aligned} \quad \text{(IV.1)}$$

The numerical values were chosen close to those encountered in the experimental data,

$Z=3480$, $b=30$, $A=6000$, $e=40000$, $x_i=3380, 3390 \dots 3580$, so that incidental errors in the computer programme due to a particular combination of numerical values would have been discovered.

Set (a) simulates the ideal situation where all experimental factors which determine the fluorescence count rate according to Eq.III.26 are constant. This is a test for the programme itself and a perfect fit was obtained. Formula (a) was also used to estimate the error made by approximating the two unresolved HFS crossing signals by only one Lorentzian line shape. Two crossing curves calculated from Eq.IV.1a for $Z_1=3480$ and $Z_2=3500$ were added. The least squares fit of the resulting data set produced exactly the expected crossing

position of 3490 and the deviations between calculated data and fitted curve were much smaller than usually obtained for the experimental signals (Fig.III.12). This is in agreement with the result of the χ^2 test (Sec.III.3.22).

Set (b) of Eq.IV.1 simulates a linear dependence of the experimental factors (Eq.III.26) on x which has been shown (Sec.IV.2.31) to describe the variation of most of the factors very well.

Set (c) simulates a parabolic dependence of the experimental factors on x and should be a good approximation for the nonlinear variation observed for the $Ly\alpha$ intensity (Sec.IV.2.313).

To judge the relative merits of the working line shapes using 5 and 6 parameters, both have been applied to fit the calculated data sets (b) and (c). The results for the "crossing position" Z are listed in Table IV.6.

Data set	d	XMIN	YE	Z 5 parameter	Z 6 parameter
b	$7 \cdot 10^{-4}$	-	-	3480	3480
b	$5 \cdot 10^{-3}$	-	-	3483	3480
c	-	3450	$1 \cdot 10^{-5}$	3472	3463
c	-	3420	$1 \cdot 10^{-5}$	3472	3463
c	-	3450	$-1 \cdot 10^{-5}$	3468	3496

Table IV.6 List of parameters used to calculate the simulation data sets and the results obtained for the "crossing position" Z, using the 5 parameter and the 6 parameter working line shapes. The theoretical value is $Z = 3480$.

The first three columns list the numerical values of the constants used to calculate the sets (x_i, y_i) from Eq.IV.1. The results for set (b) show that both working line shapes reproduce the value for Z when a variation of only 15% of the experimental factors over three FWHM is present ($d=7 \cdot 10^{-4}$). For a much stronger linear variation of 90% over three FWHM ($d=5 \cdot 10^{-3}$) the second row shows that, as to be expected, the 6 parameter fit is better.

The data sets (c) simulate a parabolic dependence of the experimental factors with the minimum at 3450, the minimum at 3420, and the maximum at 3450. In all cases the results from the 5 parameter working line shape are in better agreement with the theoretical value of $Z = 3480$.

To decide which working line shape was more suitable for the experimental level crossing signals both line shapes have been applied to the signals of crossing X1 for zero electric field. The theoretical value for the position of this crossing of 3484.1 G was approached closer by the results of the 5 parameter working line shape (3480.9 G for 7 runs) than by the result of the 6 parameter line shape (3489.5 G for the same 7 runs). Therefore, the 5 parameter working line shape as given in Eq.III.29 was used to fit all crossing signals.

The simulation runs listed in Table IV.6 (c) for the 5 parameter line shape show deviations of 8, 8, and 12 from the theoretical value. Considering that these simulations overestimated the parabolic dependence and produced more severe distortions of the original Lorentzian line profile

than encountered in the experimental crossing signals it was decided to allow an uncertainty $\Delta B_3 = \pm 10$ G in the experimental results. It was felt that ΔB_3 should be a conservative estimate of the error introduced by distortions of the experimental crossing signals, and no further error has been added for approximating the crossing signal as a function of the electric field by a Lorentzian profile.

Since some of the distortions can shift the result for the crossing position to higher or lower values, the uncertainty ΔB_3 will be more important in cases where only a single crossing signal is available but will partially cancel when averaging the results of several runs. An example of the cancellation is the excellent agreement between the experimental result of (3484.3 ± 1.3) G obtained from 13 runs for crossing X1 without electric field, with the theoretical value of 3484.1 G.

IV.3 Conclusion

IV.3.1 Comparison of experiment and theory

For comparison, the results of the most reliable experiment, LC4, for the crossing X1 are listed again in Table IV.7 together with theoretical values. The theoretical crossing positions were obtained by using different values for the Lamb shift S' or by changing all electric field matrix elements by applying different values for a_0 in the calculations.

As shown in Fig.IV.7 the calculated crossing positions are shifted to higher magnetic field values if the Lamb shift is smaller and they are shifted to lower magnetic fields if the Stark effect matrix elements are too small. The curves in Fig.IV.7 were calculated for,

- (1) $S' = S$ and $a'_0 = a_0$,
- (2) $S' = S$ and $a'_0 = 98\% a_0$,
- (3) $S' = 0$ and $a'_0 = a_0$.

As can be seen in the figure the experimental results for the higher field values lie between the curve calculated for the theoretical Stark effect matrix elements which are estimated to be correct to 1 part in 10^4 , and the curve obtained when underestimating the matrix elements by 2%.

Thus, good agreement between theory and experiment has been established within the accuracy of the experimental results of about 2%.

Taking the systematic errors ΔB and ΔE of Table IV.1 into account the difference between theory and experiment is approximately $(-1 \pm 2)\%$. Although ΔB and ΔE can be regarded as limits of the known systematic errors, the difference of 1% is not significant because for experiment LC4 further systematic errors of order 2% cannot be excluded (Sec.IV.2.21).

Exp IC4	E/kV m^{-1}	B/G	Calculated values									
			$S' = S$	S	S	S	S	S	S	S	S	S
			$a'_0 = a_0$	$99\%a_0$	$98\%a_0$	$95\%a_0$	$90\%a_0$	a_0	$90\%S$	a_0	0	
0.0	3483.9		3484.1	3484.1	3484.1	3484.1	3484.1	3484.1	3484.1	3484.1	3484.1	
19.68	3490.6		3491.3	3491.2	3491.0	3490.6	3489.9	3491.5	3493.2	3493.4		
29.52	3498.2		3500.3	3499.9	3499.6	3498.7	3497.2	3500.6	3504.2	3504.8		
49.20	3523.8		3529.1	3528.0	3527.1	3524.5	3520.4	3529.8	3539.4	3540.9		
78.73	3589.5		3598.7	3596.0	3593.8	3587.2	3576.7	3600.6	3622.9	3626.3		
123.3	3746.2		3759.6	3754.4	3749.1	3733.6	3708.7	3764.6	3809.1	3815.5		
180.0			4051.5	4041.0	4015.6	3999.9	3950.4	4059.	4127.7	4136.9		
182.6	4050.											
220.0			4300.5	4286.0	4271.7	4229.1	4159.7	4309.9	4390.2	4400.8		
222.69	4300.											
250.0			4504.9	4487.2	4469.9	4418.2	4333.6	4515.2	4602.1	4613.5		
252.0	4500.											

Table IV.7 Comparison of the results obtained in experiment IC4 and the theoretical values calculated for various values S' for the Lamb shift and for various values of the Stark effect matrix elements using a_0 as variable parameter.

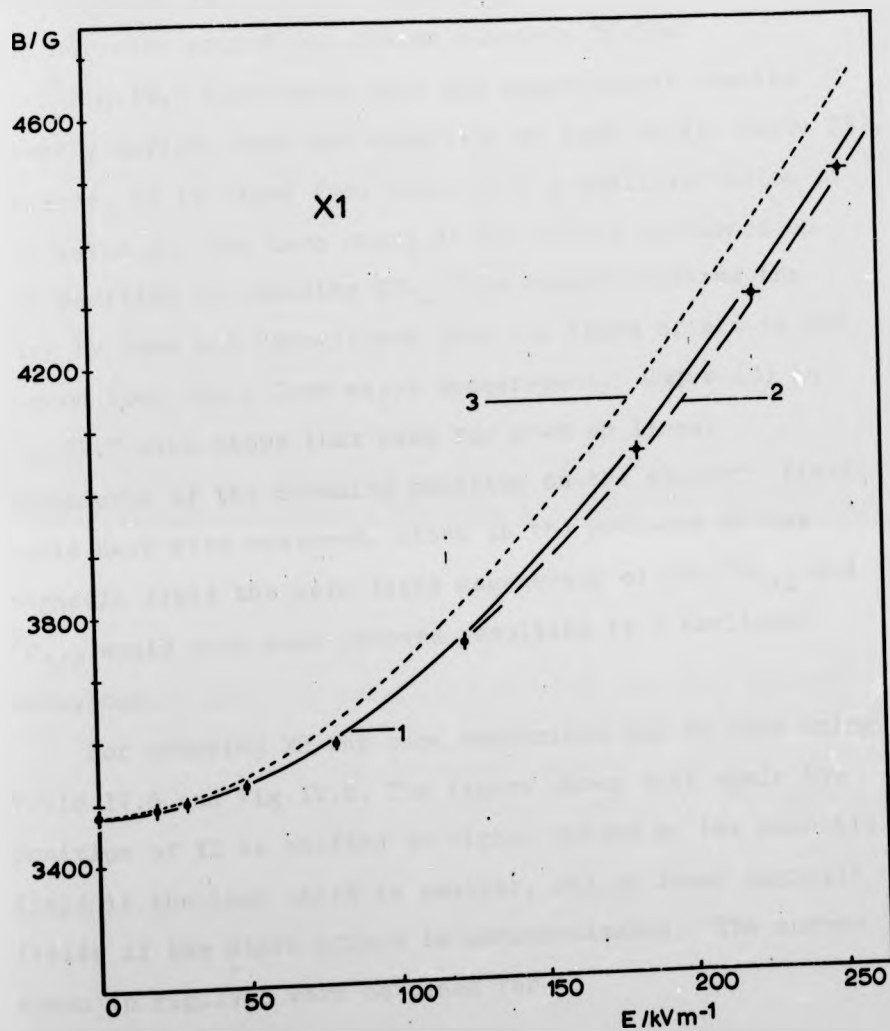


Fig.IV.7 Results of experiment LC4 for the position of crossing X1 in comparison with theoretical values obtained for different values S' for the Lamb shift and different values for the Stark effect matrix elements by using a_0 as variable parameter. The curves are calculated for

- (1) $S' = S$ and $a'_0 = a_0$,
- (2) $S' = S$ and $a'_0 = 98\% a_0$,
- (3) $S' = 0$ and $a'_0 = a_0$.

It should also be remembered that the comparison between theory and experiment in this way assumes equal amplitude of the two HFS crossings, an assumption which has not been proved for finite electric fields.

Fig.IV.7 also shows that the experimental results clearly deviate from the case with no Lamb shift, curve (3). However, as is clear from Table IV.7 a small variation of the value for the Lamb shift S' has little influence on the position of crossing X1. This result confirms the view by Rose and Carovillano that the Stark effect is not a good tool for a Lamb shift measurement. Curve (3) in Fig.IV.7 also shows that even for $S'=0$ no linear dependence of the crossing position on the electric field could have been measured, since in the presence of the magnetic field the zero field degeneracy of the $^2S_{1/2}$ and $^2P_{1/2}$ would have been removed resulting in a nonlinear behaviour.

For crossing X2 the same comparison can be made using Table IV.8 and Fig.IV.8. The figure shows that again the position of X2 is shifted to higher values of the magnetic field if the Lamb shift is smaller, and to lower magnetic fields if the Stark effect is underestimated. The curves shown in Fig.IV.8 were obtained for

- (1) $S' = S$ and $a'_0 = a_0$,
- (2) $S' = S$ and $a'_0 = 80\% a_0$,
- (3) $S' = 90\% S$ and $a'_0 = a_0$.

As may be seen from Table IV.8 the position of crossing X2 is less sensitive to small variations of the Stark effect matrix elements than crossing X1. On the other hand, crossing X2 is much more sensitive to a change of the Lamb shift, and the present data would allow a determination of the Lamb shift within about 10%.

Exp LC3 E/kVm ⁻¹	B/G	Calculated values				
		S'=S a ₀ '=a ₀	S 99%a ₀	S 98%a ₀	S 80%a ₀	90%S a ₀
0.0		2358.9	2358.9	2358.9	2358.9	2384.1
48.68	2357	2376.8	2376.4	2376.1	2370.6	2400.3
60.88	2374.9		2385.4	2384.9	2376.8	2408.6
73.02	2405.5		2395.5	2394.8	2383.9	2417.9
97.4	2410.05	2418.9	2417.9	2417.0	2400.5	2438.5
98.41	2422.6					
121.95	2437.87	2442.6	2441.4	2440.0	2419.0	2460.0
138.1	2450.3					
183.0	2500.4	2494.3	2493.0	2491.6	2465.0	2506.5
195.1	2502.3	2502.7	2501.4	2500.1	2473.3	2514.1
292.7	2548.5	2550.2	2549.2	2548.2		2556.6
390.2	2570.2	2574.2	2573.5	2572.8	2556.3	2578.2
487.8	2581.7	2587.1	2586.7	2586.4	2574.2	2589.8

Table IV.8 Comparison of experimental results and theoretical values obtained for various values S' of the Lamb shift and for various values of the Stark effect matrix elements using a₀ as variable parameter.

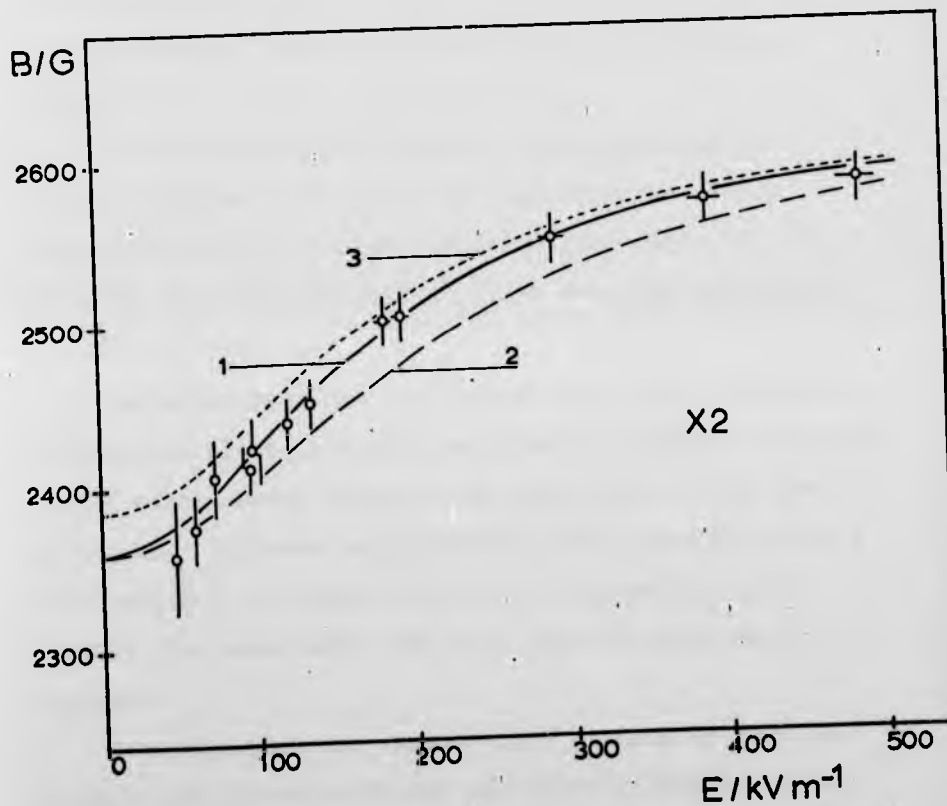


Fig.IV.8 Experimental results for the position of crossing X2 in comparison with theoretical values calculated for different values δ' of the Lamb shift and for different values of the Stark effect matrix elements using a'_0 as variable parameter. The curves are obtained for

- (1) $\delta' = \delta$ and $a'_0 = a_0$,
- (2) $\delta' = \delta$ and $a'_0 = 80\% a_0$,
- (3) $\delta' = 90\% \delta$ and $a'_0 = a_0$.

IV.3.2 Final remarks

The results of the atomic beam level crossing experiment of the nonlinear low-field Stark effect in the level $n=2$ of hydrogen agree within about 2% with the theoretical values based on numerical diagonalisation of the combined Zeeman and Stark effect perturbation matrices.

On the theoretical side the comparison between theory and experiment could be improved by a closer investigation of the level crossing line shape by applying the Breit formula Eq.II.54 for each combination of external fields.

The experiment can be improved by a more accurately constructed electric field condenser and better stability of the experimental factors, in particular of the $Ly\alpha$ intensity. Improved experimental level crossing signals would warrant the application of a more sophisticated working line shape and lead to a more accurate data analysis.

Concentrating the experimental efforts on just one value of the electric field, the Stark effect could be measured to better than 1%. The most suitable value is $E = 180$ kV/m for crossing X1.

Similarly a measurement of the Lamb shift could be carried out using $E = 120$ kV/m for crossing X2 to better than 5%. This estimate confirms that the Stark effect is not suitable for a precision measurement of the Lamb shift in hydrogen but the method may be of interest for other elements.

LIST OF REFERENCES

- A70 Andra H J, Phys Rev A 2, 2200 (1970)
- B33 Breit G, Revs Mod Phys 5, 91 (1933)
- B67 Bass A M , Appl Optics 5, 12 (1967)
- B70 Brodsky S J, Atomic Physics 2; Proc II Intern
Conf on Atomic Physics, Plenum Press, London
(1971)
- BBGM72 Baird J C, J. Brandenberger, K I Gondaira and
H Metcalf, Phys Rev A 5, 564 (1972)
- BD64 Bjorken J D and S D Drell, Relativistic Quantum
Mechanics, McGraw-Hill Inc. New York (1964)
- BE73 Beyer H J, PhD Thesis, University of Stirling (1973)
- BK67 Bonch-Bruevich AM and VA Khodovoi, Usp Fiz Nauk
93: 71 (1967) (Soviet Phys Usp 10, 637 (1968))
- BMN65 Budick B, S Marcus and R Novick, Phys Rev 140
A 1041 (1965)
- BMW67 Barth W, R S Martin and J H Wilkinson,
Numerische Mathematik 9, 386 (1967)
- BP67 Brodsky S J and R G Parsons, Phys Rev 163, 134
(1967)
- BPr68 Brodsky S J and J R Primack, Phys Rev 174, 2071
(1968)
- BPr69 Brodsky S J and J R Primack, Ann Physics 52, 315
(1969)
- BR70 Barnett C F and J A Ray, Rev Sci Instr 41, 1665
(1970)
- BS57 Bethe H A and E E Salpeter, Quantum Mechanics of
One- and Two-Electron Atoms, Springer Verlag,
Berlin (1957)
- BS73 Blackman J A and G W Series, J Phys B 6, 1090
(1973)
- C74 Cordle J E, J Phys B 7, 1284 (1974)
- E16 Epstein P S, Ann Physik 50, 489 (1916)
- E60 Edmonds A R, Angular Momentum in Quantum Mechanics
Princeton University Press (1960)
- E71 Erickson G W, Phys Rev Lett 27, 12, 780 (1971)
and Computer Programme, University of Surrey,
Guildford

LIST OF REFERENCES (cont.)

- E73 Eck T G, Phys Rev Lett 31, 5, 270 (1973)
- F34 Frerichs R, Ann Physik (5), 19, 1 (1934)
- F61 Franken P A, Phys Rev 121, 508 (1961)
- FB58 Fite W L and R T Brackmann, Phys Rev 112, 1141 (1958), *ibid.*p1151
- FEB65 Fehsenfeld F C, K M Evenson and H P Broida, Rev Sci Instr 36, 294 (1965)
- G63 Gebauer R, Physikertagung Hamburg 1963, Physik Verlag, Mosbach/Baden
- GAM74 Gaupp A, H J Andrä and J Macek, Phys Rev Lett 32, 6, 268 (1974)
- GJ67 Gebauer R and Jäger H, Acta Phys Austr 26, 123 (1967)
- GS70 Gebauer R and H Selhofer, Acta Phys Austr 31, 8, (1970)
- GS2 70 *ibid.* 31, 131 (1970)
- HIII Lamb W E, Phys Rev 85, 259 (1952)
- H62 Heddle D W O, J Quant Spectrosc Radiat Transfer 2, 349 (1962)
- H67 Hughes J W B, Proc Phys Soc 91, 810 (1967)
- H72 Heckmann P H, Z Physik 250, 42 (1972)
- HF67 Himmel L C and P R Fontana, Phys Rev 162, 23 (1967)
- HH73 Hashimoto M and T Hayashi, Rev Sci Instr 44, 1125, (1973)
- HHKN72 Hahn Y B, R E Hebner, D R Kastelein and K J Nygaard, Rev Sci Instr 43, 695 (1972)
- HRK56 Heberle J W, H A Reich and P Kusch, Phys Rev 101, 612 (1956); *ibid.* 104, 1585 (1956)
- IH28 Ishida Y and S Hiyama, Sci Pap Inst Phys Chem Research Tokyo, 9, 1 (1928)
- J41 Jeans J, The Mathematical Theory of Electricity and Magnetism, Cambridge, At the University Press 1941
- K33 Kassner L, Z Physik 81, 346 (1933), and Physik Zeitschrift 34, 289 (1933)

LIST OF REFERENCES (cont)

- K61 Kleinpoppen H, Z Physik 164, 174 (1961)
- K67 Krakowski R A, PhD Thesis, University of California, Berkeley
- K72 Knight P L, J Phys A 5, 417 (1972)
- KHL66 Khadjavi A, W Happer and A Lurio, Phys Rev Lett 17, 9, 463 (1966)
- KRSS73 Kibble B P, W R C Rowley, R E Shawyer and G W Series, J Phys B 6, 1079 (1973)
- KSC73 Kulkarni R G, N V V J Swamy and E Chaffin, Phys Rev A 7, 27 (1973)
- L Lamb, see H III
- L13 LoSurdo A, Rend Accad Lincei 22, 665 (1913)
- L30 Lanczos C, Z Physik 65, 431 (1930)
- L31 *ibid* 68, 204 (1931)
- L50 Lüders G, Zeits.Naturf. 5a, 608, (1950)
- L51 Lüders G, Ann Physik (6), 8, 301 (1951)
- L55 Lee P, J O S A 45, 703 (1955)
- LR47 Lamb W E and R C Retherford, Phys Rev 72, 241 (1947)
- M68 MPherson Technical Bulletin No 101 (1968)
- MBB68 Metcalf H, J R Brandenberger and J C Baird, Phys Rev Lett 21, 165 (1968)
- MZ34 Mitchell A C G and M W Zemansky, Resonance Radiation and Excited Atoms, Cambridge, At the University Press (1934)
- N67 Nahum J, Phys Rev 158, 814 (1967)
- R29 Rojanski V, Phys Rev 33, 1 (1929)
- R31 Rausch von Traubenberg H, Z Physik 71, 291 (1931)
- R56 Rother H, Ann Physik (6), 17, 185 (1956)
- R65 Robiscoe R T, Phys Rev 138, A22 (1965)
- R68 Robiscoe R T, Phys Rev 168, 4 (1968)
- R69 Roman P, Introduction to Quantum Field Theory J Wiley & Sons Inc. (1969)
- Ra56 Ramsey N F, Molecular Beams, Oxford, At the Clarendon Press (1956)
- RBMW59 Rotenberg M, R Bivens, N Metropolis and J K Wooten, The 3j symbols and 6j symbols, Technology Press Cambridge Massachusetts (1959)
- RC61 Rose M E and R L Carovillano, Phys Rev 122, 1185 (1961)

LIST OF REFERENCES (cont.)

- RMJ69 Raz B, J Magen and J Jortner, Vacuum 19, 571 (1969)
- RS70 Robiscoe R T, and T W Shyn, Phys Rev Lett 24,
559 (1970)
- S28 Schlapp R, Proc R.Soc (London) A 119, 313 (1928)
- S67 Samson J A R, Techniques of Vacuum Ultraviolet
Spectroscopy, J Wiley & Sons Inc (1967)
- Sch26 Schrödinger E, Ann Physik 80, 437 (1926); *ibid.*457
(1926)
- Schw16 Schwarzschild K, Sitzb Berl Akad p.548
- Se57 Series G W, Spectrum of Atomic Hydrogen, Oxford
University Press (1957)
- Se64 Series G W, Phys Rev 136, A684 (1964)
- Sj32 Sjögren K; Z Physik 77, 290 (1932)
- SJ49 Steubing W and W Junge, Ann Physik (6) 5, 108,(1949)
- SKS39 Steubing W, A Keil and F Stolpe, Z Physik 112,
560 (1939)
- St13 Stark J, Abh Berl Akad, 47, 932 (1913)
- St14 Stark J, Ann Physik 43, 965 (1914); *ibid.*p983 (1914)
- T58 Tittel K, Dipl.arbeit, Phys.Inst.Universität
Tübingen (1958)
- T74 Wu-yang Tsai, Phys Rev A, 9, 1081 (1974)
- TPL69 Taylor B N, W H Parker and D N Langenberg,
Rev Mod Phys 41, 375 (1969)
- V99 Voigt W, Ann Physik 69, 297 (1899); *ibid* 4, 197(1901)
- V67 Vanier J, Appl Optics 6, 167 (1967)
- W62 Wilkinson J H Num Math 4, 354 (1962)
- W2 62 *ibid* 4, 368 (1962)
- Wa62 Warneck P, Appl Optics 1, 721 (1962)
- Wa65 Warneck P, J O S A 55, 921 (1965)
- WB65 Wilkinson P G and E T Bryan, Appl Optics 4,581(1965)
- WE67 Wieder H and T G Eck, Phys Rev 153, 103 (1967)
- WF67 Wing W H and P R Fontana, Bull Am Phys Soc 12, 1, 95
(1967) FG14
- Z66 Zugenmaier P, Zeits Angew Phys 20, 184 (1966)

Attention is drawn to the fact that the copyright of this thesis rests with its author.

This copy of the thesis has been supplied on condition that anyone who consults it is understood to recognise that its copyright rests with its author and that no quotation from the thesis and no information derived from it may be published without the author's prior written consent.